Ministry of Education
FEDERAL UNIVERSITY OF ITAJUBÁ
Created by Law nº 10435, from 24th April 2002

POSTGRADUATE PROGRAM IN
MATERIALS FOR ENGINEERING

FERNANDO SILVA PENA

Photoconductivity and electrical transport properties in PbTe single quantum well samples

Itajubá, July 2019

Ministry of Education
FEDERAL UNIVERSITY OF ITAJUBÁ
Created by Law nº 10435, from 24th April 2002

POSTGRADUATE PROGRAM IN
MATERIALS FOR ENGINEERING

FERNANDO SILVA PENA

Photoconductivity and electrical transport properties in PbTe single quantum well samples

Thesis submitted to the Graduate Program in Materials for Engineering as part of the requisites for obtaining qualification of PhD in Materials for Engineering.

Concentration Área: Non-metals
Researche Line: Semiconductors

Supervisor: Dr Marcelos Lima Peres
Co-supervisors: Dr. Paulo Henrique de O. Rappl and Dr. Demetrio Arthur Werner Soares.

Itajubá, July 2019

I dedicate this thesis to my father that even in his last breaths encourage me to continue this path.

Lots of proud my father, and gratitude!

Acknowledgment

First thanks to my wife, for all the support and patience in these troubled years. If it had not been for her, I would not have followed this path.

To my lab colleagues, in special to Marília for all the theoretical and personal discussion and the learning.

To Dr. Soares and Dr. Rappl for the co-orientation and for the lab and time disposition.

To Dr. Abramof and Dr. Rappl for the samples growing, the lab disposition and the support.

Also, I would like to thanks to Dr. Peres for the orientation, the patience, willingness, support and for all beers that avoided me from going crazy.

Abstract

We investigated the photoconductivity effect in 10 and 14 nm well thickness *n*-type $PbTe/Pb_{1-x}Eu_xTe$ quantum wells, with *x* values of 0.12 and 0.1, for a temperature range of 300–10K using infrared light. Also, magnetotransport properties measurements are performed in 8, 10, 15, 20 and 30 nm well width *p*-type $PbTe/Pb_{0.9}Eu_{0.1}Te$ quantum wells, at magnetic fields up to 33 T and temperature varying from 0.35 to 300 K, under dark and illuminated condition. For the *n*-type PbTe quantum wells, the measurements revealed that at high temperatures, the photoresponse has small amplitude. As temperature decreases to T~75 K, the photoconductivity amplitude increases reaching a maximum value 10 times higher than the original value before illumination. From Hall measurements performed under dark and light conditions, we show that this effect is a result of carrier concentration increase under illumination. Unexpectedly, for further reduction of temperature, the amplitude starts to decrease again. The electrical resistance profiles indicate that the transport occurs through barriers and the well that behave as two parallel channels. For temperatures below 75K, transport is more effective in the quantum well, where the signal reduction can be associated with the electron-electron scattering due to the increase in the carrier concentration that occurs under illumination. We also used the random potential model to explain the origin of the persistent effect observed in the photoconductivity curves. We compare magnetotransport measurements in *p*-type $PbTe/Pb_{0.9}Eu_{0.1}Te$ quantum wells with different widths: 10, 15 and 20 nm, revealing clearly QHE and SdH oscillations, which evidences the two-dimension electron gas formation and the high quality of the samples. The 10 nm well width presented odd non-integer filling factors sequence (2.3; 3.4; 5.6; 6.9 and 8.8). The non-integer values may be associated to edge states, since that parallel conduction in the interface, between the barrier and well, was not enhanced or destroyed by illumination, although the carrier concentration was enhanced. Further investigations are necessary to clarify this effect and we consider the approximated integers 2; 4; 6; 7 and 9 calculated from experimental *B* values. For the 15 and 20 nm QW thickness, the SdHO and QHE also appear, however, it reveals an even integer filling factors sequence. The 10 nm QW thickness odd sequence originated from the first sub-band Landau level spin splitting; according to the Fermi level compared to the longitudinal and transversal resistance together with the first longitudinal sub-band spin splitting simulation. This assumption

agrees with the FFT analysis that reveals the main frequency peak and two other ones, which may be the second harmonic spin splitting, up and down. The same FFT profile appears for the other two samples. Nevertheless, the 8 and 30 nm well width sample presented an insulator profile behavior and neither SdHO nor QHE were present. It is probably because the indium contacts do not diffuse through the PbTe layer well.

List of Abbreviations

2D - Two-dimensional

B - Magnetic field

BEP - Equivalent beam pressure

Bi - Bismuth

CB - Conduction band

CHE - Classic Hall effect

CMR - Classic magnetoresistance

DOS - Density of states

E_g - Energy gap

ff - Filling factors

FQHE - Fractional quantum Hall effect

GMP - Galvanomagnetic phenomena

HFML - High Magnetic Field Laboratory

HLN - Hikami, Larkin, and Nagaoka

INPE - National Institute of Spatial Researcher

IQHE - Integer quantum Hall effect

IR - Infrared

LABAS - Sensor and Material Associated Laboratory

LL - Landau Levels

LMR - Linear magnetoresistance

MBE - Molecular beam epitaxy

MIT - Metal-to-insulator transition

MQWs - Multiple quantum wells

MR - Magnetoresistance

PC - Photoconductivity

PPC - Persistent photoconductivity

PPMS - Physical Properties Measurements System

QHE - Quantum Hall effect

QLMR - Quantum linear magnetoresistance

QWs - Quantum wells

RHEED - Reflection high-energy electron diffraction

RM - Resistive magnet

SdH - Shubnikov-de Haas

SdHO - Shubnikov-de Hass oscillations

SO - Spin-orbit

UHV - Ultra-high vacuum

VB - Valence band

ZT - Figure of merit

LR - Longitudinal resistance

Summary

Acknowledgment IV
Abstract V
List of Abbreviations VII
Summary IX
1. Introduction 8
2. Literature review 11
2.1. PbTe based structures 11
2.1.1. PbTe films 11
2.1.2. PbEuTe alloys 15
2.1.3. PbTe QWs 18
2.2. Photoconductivity effect 21
2.2.1. Persistent photoconductivity effect (PPC) 24
2.3. Hall effect 27
2.3.1. Classic Hall effect 28
2.3.2. Quantum Hall effect 32
2.4. Magnetoresistance 38
2.4.1. Classic Magnetoresistance 39
2.4.2. Shubnikov-de Haas Oscillations 41
2.4.3. Linear Magnetoresistance 45
3. Experimental setup 47
3.1. Molecular beam epitaxy (MBE) 47
3.1.1. Crystallization processes 54
3.1.2. Sample growth data 56
3.2. Photoconductivity setup 59
3.3. Magnetoresistance experimental setup 60
3.4. Setup for Hall characterization 62
3.5. Experiments performed at High Fields Magnetic Laboratory (HFML) 63
4. Results and analysis 66
4.1. Photoconductivity results 66
4.2. Magnetotransport 75

5. Conclusions 106
6. Bibliography 109

1. Introduction

PbTe based quantum wells (QWs) have been widely used to fabricate infrared (IR) lasers, IR detectors, and thermo generators during the last decades [1-4]. Also, due to the large spin-orbit (SO) coupling interaction effect, PbTe based structures have emerged as potential candidates for spintronic based devices development [5-9]. In fact, Peres *et al.* (2014) [10] reported a large Rashba spin-orbit coupling effect in *n*-type PbTe quantum wells and Chitta *et al.* (2005) [11] showed a complex transport mechanism due to the multivalley band structure that leads to an unusual quantum Hall effect. Optical and electrical transport properties have been investigated in details over the years for PbTe compounds in order to fully describe the physical properties of this compound for potential applications. However, a topic that lacks investigation is the disorder effect on the physical properties PbTe based structure. This is important from the theoretical as well as from the practical point of view. For example, to develop high-performance sensors, it is mandatory to reduce the noise intensity and increase the electrical response. One way to reduce noise is increasing carrier concentration; this can be done by deviation from stoichiometry or doping. However, there is a limit since both processes generate disorder in the crystal lattice.

Since there is a lack of information about *p*-type PbTe/PbEuTe QW electrical transport properties in the literature (until this investigation begin), the main goal of this work is to present a detailed description of magnetotransport and photoconductivity effect on PbTe QWs, investigating the Shubnikov-de Haas and Quantum Hall Effect at high magnetic fields and low temperatures, for a sample series with different PbTe layer thickness. The Shubnikov-de Haas effect can provide carrier concentration, Landé *g* factor, effective cyclotron masses, mobility gap, and Landau broadening. The Quantum Hall Effect provided the filling factor sequence, presenting the occupation of the subbands as a function of the applied magnetic field. In addition, we performed photoconductivity measurements in two *n*-type PbTe/PbEuTe:Bi QWs. The *n*-type QWs were well studied in the past few decades; however, some gaps concerning the doping effect on electrical transport needs to be filled. Photoconductivity measurements enabled the investigation of the effect of trap states on transport properties as a function of temperatures and to address the position of the trap level within the band structures.

This work is divided into five chapters. In Chapter 2 there is a literature review related to structures based on PbTe, PbEuTe alloys, and PbTe QW. Also, some important effects used to analyze the experimental data presented in Chapter 4 are discussed.

In Chapter 3, the experimental setup used to obtain the data is presented along with the molecular beam epitaxy (MBE) technique, which was used to grow the samples. In this chapter, we discuss the MBE equipment and the growing procedure. Also, the setup used for the Hall, photoconductivity, magnetoresistance, and high magnetic fields measurements are explained.

In chapter 4, the results for *n* and *p*-type QWs are presented. For *n-type* QW, an insulator character was observed at room temperature for *R(T)* curves, presenting small response under infrared (IR) light. A metallic behavior is observed for lower temperatures, showing a high photoresponse when the sample is irradiated. Also, the persistent photoconductivity (PPC) (discussed in section 2.2) was observed, which indicates that the disorder plays an important role in this kind of sample. Furthermore, a fast photoresponse was observed, which is a crucial characteristic for IR sensor devices application. We compare the results of 10 nm and 14 nm QW thickness, obtaining the same behavior which ensures the reproducibility of this work. These results are minutely discussed in section 4.1.

In section 4.2 we discuss the results for *p*-type PbTe/$Pb_{0.9}Eu_{0.1}Te$ samples. The QW thickness influence on the transport properties was first investigated in a series of QWs with a thickness of 10 nm, 20 nm and 30 nm. The 10 nm QW thickness sample presents a metallic behavior for all temperature range (300 K - 1.9 K). The Shubnikov-de Hass oscillations (SdHO), as well as the Quantum Hall effect (QHE), manifest at temperatures lower than 50 K and for magnetic fields (B) values starting from 4 T. However, the 20 nm and 30 nm QW thickness present metallic and insulator behavior at different temperatures range, showing the barrier contribution for electrical transport. Also, for magnetic fields (B) up to 9 T, neither SdHO nor QHE are observed for these samples. Unlike the previous samples, the one with a thickness of 10 nm presents oscillations and QHE for $B > 7$ T.

In Chapter 5, the results are summarized. For *n*-type samples, we verified that the contribution from each channel depends on the temperature region. Also, we have showed that the decrease in photoconductivity amplitude for temperatures below 75 K is due to the electron-electron scattering

enhanced by conduction via multiple valleys, which leads to a reduction of carrier mobility. For *p*-type samples, the 10 nm thickness one presents the best results, showing metallic behavior for all temperature range, presenting clearly QHE and SdH oscillations starting at $B = 4$ T. We associated the odd filling factor (ff) sequence to the Landau level spin splitting that appears as two close frequencies which is in good agreement with the high g factor value obtained from the main oscillatory component of the magnetoresistance (MR).

2. Literature review

In this chapter, the fundamental theory of electrical transport and photoconductivity properties based on PbTe compounds are presented. In addition, the recent results presented in the literature about these structures are discussed. The information provided in this chapter supports the analysis presented in the "Results and discussion" chapter.

2.1. PbTe based structures

Lead salt compounds present peculiar physical properties and have been investigated for at least 50 years. The electrical, optical, thermal and mechanical properties were well established by many investigators [1, 12-19]. The advent of molecular beam epitaxy (MBE), since 1968, among other growth techniques, has allowed the growth of epitaxial films with high crystalline quality, thus, has enabled a better understanding of condensed matter physics. For the investigation of nanostructures, the sample quality is of great concern.

In this work, we investigated, doped and undoped, PbTe quantum wells (QWs) structures, confined between insulating $Pb_{1-x}Eu_xTe$ barriers. The properties description of each material forming the single quantum well structure is given next. This description helps to analyze the data presented in Chapter 4.

2.1.1. PbTe films

Even though there is vast information on several PbTe properties in literature, in this section, only the relevant properties for our analysis are discussed.

PbTe belongs to the IV-VI group elements and is a direct-gap multivalley semiconductor with a Fermi surface consisting of four equivalent ellipsoids of revolution, around the axes <111>. There is one ellipsoid in the [111] direction and three others making an angle of 70.53° with this axis in the directions: $[\bar{1}11]$, $[11\bar{1}]$ and $[1\bar{1}1]$, Figure 2.1(c), with energy minima at the Brillouin zone L point ($L_6^- - L_6^+$), Figure 2.1(a). The energy gap value is ~300 meV at room temperature and its crystalline structure is fcc type (NaCl type crystalline structure), Figure 2.1(b).

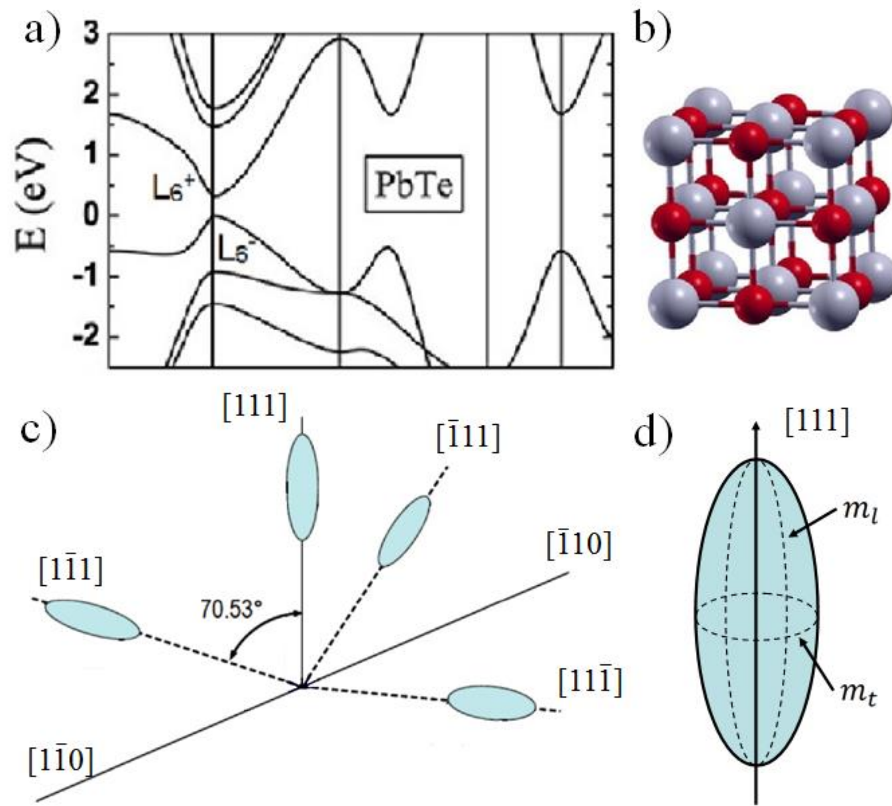

Figure 2.1 (a) Band structure of PbTe. (b) Schematic illustration of the NaCl unit cell (rock-salt type, face-centered cubic structure, fcc) used to represent PbTe, where the big spheres represent the Pb and the small ones represent the Te. (c) Illustration of the revolution ellipsoids for PbTe, oriented in the directions $[111]$, $[\bar{1}11]$, $[1\bar{1}1]$ and $[11\bar{1}]$ for the valence band in the first Brillouin zone. (d) Schematic representation of the constant energy ellipsoid (Fermi surface) in the [111] direction and the respective indication of the effective masses: longitudinal (m_l) and transversal (m_t).

This unusual Fermi surface also leads to a high mass anisotropy, which is the relation between the longitudinal and transversal mass (m_l/m_t), shown in Figure 2.1(d). The value found in the literature is ~10 for PbTe [20], a high value when compared, for example, with GaAs, which has anisotropy of ~5 [21].

Another important characteristic of PbTe is its large dielectric constant that reaches $\epsilon \sim 380$ at room temperature and ~1400 at 4.2 K [19]. This huge value arises from the lattice contributions and leads to an effective screening against impurity scattering. This allows high carrier mobility values [22] that can reach up to 2×10^6 cm^2/Vs [23].

As pointed out earlier in the introduction, the spin-orbit interaction is very strong in these materials. Due to strong Fermi surface anisotropy, longitudinal and transversal effective *g*-factor components appear and their values are found to be around $g_{\parallel}^{*} \sim 55$ and $g_{\perp}^{*} \sim 25$ [24] , respectively. The effective *g*-factor is defined in terms of the energy that spin contributes to the total electronic energy under a magnetic field:

$$E_n = (n-1)\hbar\omega_c \pm \frac{1}{2} g \mu_B B \tag{2.1}$$

This high *g*-factor value causes the twofold Kramers degeneracy of energy bands, splitting each level by two, as represented in Figure 2.2 [25].

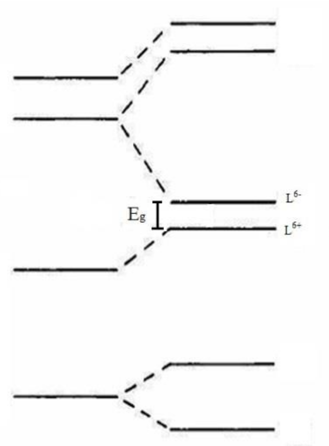

Figure 2.2 Degeneracy of energy bands, showing the spin splitting due to high *g* factor.

This quadruplet degeneracy can be broken by strain or two-dimensional confinement. This complex energetic structure induces non-trivial electrical transport. It was verified in *n*-type PbTe quantum well (QW) structure that the multiple valleys and a high electronic density allow the observation of an anomalous sequence of filling factors in the Integer Quantum Hall effect [11].

For *p*-type QWs, there are no results in the literature so far concerning the investigation of the integer quantum Hall effect.

For the majority of papers presented in the literature, structures based on PbTe are grown on BaF_2 substrates. However, due to the strain arising from the lattice mismatch between the substrate and the film, the valley along the longitudinal axis oriented in the [111] direction is shifted down, suffering an energy reduction of about 5 meV, in relation to the other three oblique valleys [26]. As a consequence, for an *n*-type PbTe film, the three oblique valleys may undergo depopulation with electrons migrating to the longitudinal valley. In the case of *p*-type PbTe film, the opposite occurs, the holes migrate from the longitudinal valley to the obliques. However, for high carrier concentrations or high temperatures, all valleys will be occupied, *i.e.,* when the Fermi level is higher than 5 meV.

PbX (X = Te, Se, S) also have some advantages compared to other semiconductors. The *n*-type charge carriers can be controlled by doping with bismuth (Bi) and also by means of intentional deviations in the stoichiometry since metal and chalcogens vacancies and interstices act as donor and acceptor centers, respectively (Chapter 3). For *p*-type carriers, doping with thallium (Tl), BaF_2 or intrinsic doping, due to stoichiometry deviation, increases the *p*-type carrier density [27]. Therefore, as mentioned, the doping addition or stoichiometry deviation leads to disorder in the crystal lattice that gives rise to defect states in PbTe. Such disorder may lead to effects that alter the electrical properties and play an important role in the photoconductivity and magnetoresistance measurements, for example, persistent photoconductivity [28] and linear magnetoresistance [29], as discussed in Sections: 2.2 and 2.4, respectively.

Theoretical studies predict that IV-VI compounds, such as PbTe, may exhibit the Spin Hall effect (discussed in Section 2.3) also due to spin-orbit coupling [30] [31] opening possibilities for future applications on spintronic-based devices [32] [33] [34]. It should be emphasized that epitaxial growth techniques are indispensable in the sample preparation for such measurements, since the low defect density, unique in these growth techniques, avoids undesired suppression of such effects.

2.1.2. PbEuTe alloys

The introduction of Eu^{2+} atoms to form $Pb_{1-x}Eu_xTe$ alloy drastically changes the optical and electrical properties of this compound. One direct consequence is the increase of the energy gap allowing large energy tunability with a variation of Eu concentration. This allows these alloys to be applied for the development of light sensors that operate from infrared (IR) to visible region in the light spectra. Another drastic consequence of the introduction of Eu atoms in PbTe is the metal-to-insulator transition (MIT) observed when Eu concentration varies between x=0.0 and x=1.0. The Eu atoms create disorder in the net decreasing the carrier mobility [35]. The transition that occurs due to disorder in the net is an Anderson type transition [36] and, for *p*-type films, this transition occurs around x=0.06 [35-37] and for *n*-type films it is around x=0.10 [26] as present in Figure 2.3. If the disorder is high enough, the carriers are no longer described by the free electron wave function and the carriers become localized leading to the metal-to-insulator transition. From the temperature dependence of the resistivity profile presented in Figure 2.3, it is possible to obtain the Eu concentration for which this transition occurs.

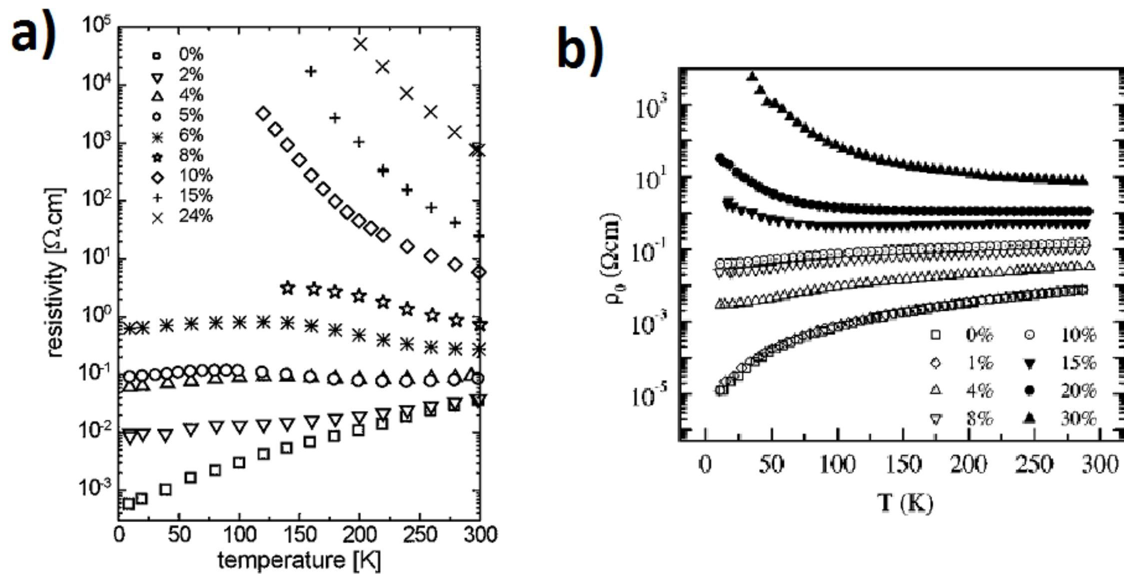

Figure 2.3 Temperature dependence of the resistivity for $Pb_{1-x}Eu_xTe$ epitaxial layer, (a) for a *p*-type film showing the MIT at x~0.05 and (b) for an *n*-type film with MIT at x~0.1. Source: [26] [37].

In Figure 2.3(a), for the p-type sample (x=0), the curve presents a metallic profile and the resistance drops as the temperature decreases. For x close to 0.06 curves start to change to an insulator behavior and the resistance increases as temperature decreases. The same changes occur in Figure 2.3(b). For the PbTe sample, the metallic behavior is present and for x values close to 0.1 curves start to behave like an insulator.

A system can present metallic or insulator behavior according to the values of the product of the Fermi wave vector k_F and the electron mean free path l. According to the Boltzmann's classical theory of conduction if $k_F l \gg 1$ the system is metallic and if $k_F l \ll 1$ the system should present an insulator behavior. If $k_F l \sim 1$ the system is a transition region [35] where both phases can coexist. The k_F can be derived from the equation:

$$k_F = \left(\frac{3\pi^2 p}{N}\right)^{\frac{1}{3}} \tag{2.2}$$

N is the number of valleys and p is the carrier concentration. l can be derived from the expression:

$$l = \frac{\hbar k_F \mu}{e} \tag{2.3}$$

The carrier concentration (p) and electron mobility (μ) can be obtained from Hall measurements that will be described in details later in the section. Figure 2.4 presents the $k_F l$ product as a function of Eu concentration for p-type $Pb_{1-x}Eu_xTe$ samples, according to [38]. It is possible to see that for $k_F l \gg 1$ Eu content is $x < 0.05$ and for $k_F l \ll 1$ Eu content is $x > 0.05$, which is in accordance to Figure 2.3(a).

In the region of weak disorder, $k_F l > 1$ but not $k_F l \gg 1$, the phenomenon of weak localization can occur, *i.e.*, the disorder gives rise to the quantum interference between the partial carrier wave functions leading to a partial MIT. Weak localization manifests at low temperatures as an increase of the electrical resistance. In case of an application of a magnetic field, negative magnetoresistance takes place which indicates a delocalization of carriers when the magnetic field is applied. For the study presented in this work, this effect is important since it helps to probe the existence of spin-orbit coupling effects. In the case of strong spin orbit-coupling, the weak localization is suppressed and the electrical resistance suffers a drop at some point at low temperatures, differently from the

asymptotic expected behavior. If a magnetic field is applied, a positive non-parabolic behavior is observed at low fields. Figure 2.5(a) presents the resistance of the *p*-type $Pb_{1-x}Eu_xTe$ epitaxial films for *x* varying from 0 up to 0.05, as a function of the temperature [35]. According to this figure, the system behaves like a metal for *x* values up to 0.04, i.e., the resistance decreases as the temperature is lowered. Figure 2.5(b) shows the magnetoresistance in the region of low magnetic fields. It is clear the presence of spin-orbit coupling effect for the sample with *x*=1%, 3% and 5%. Thus, the disorder can be useful to probe the existence of spin orbit (SO) effects.

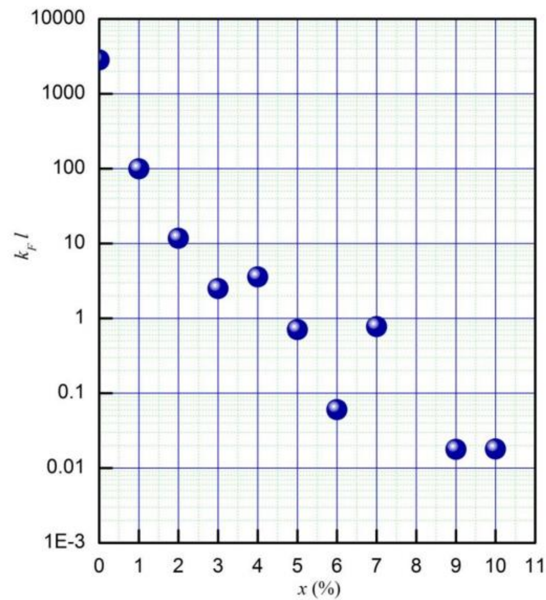

Figure 2.4 Present the $k_F l$ relation in the function of Eu concentration for p-type $Pb_{1-x}Eu_xTe$ samples. Source: [38]

Based on the MIT presented in this section, the $Pb_{1-x}Eu_xTe$ barriers are grown with x ~0.1 in order to guarantee that the electrical transport will occur mainly through the QWs. In the next section the main features of PbTe QWs are presented.

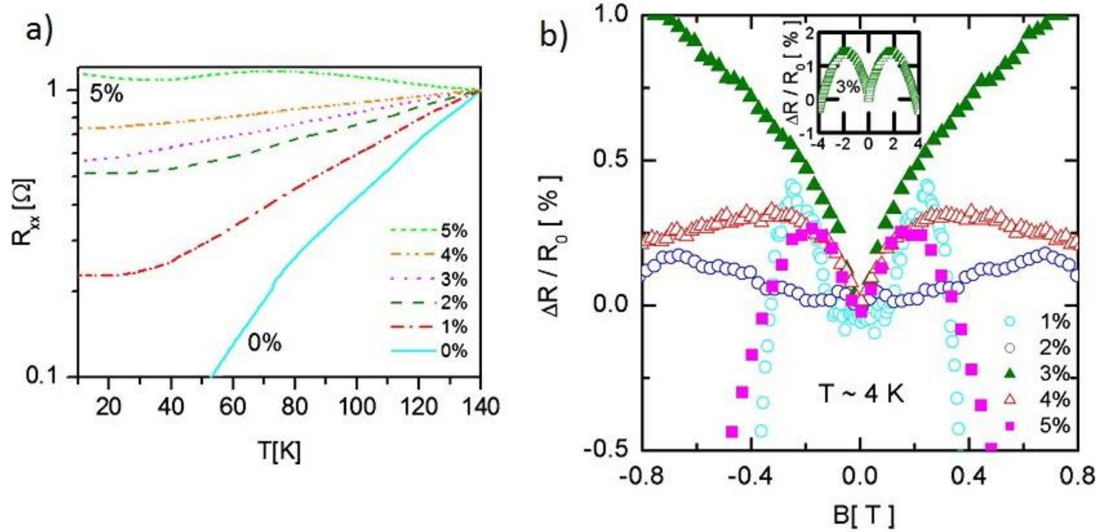

Figure 2.5 (a) Resistance in the function of temperature for $Pb_{1-x}Eu_xTe$ films with Eu concentration varying from x=0 until x~0.05, presenting an exponential behavior for certainly x>0 values indicating the antilocalization effect. (b) Magnetoresistance measurements for x~0.01 until x=0.05 showing the positive magnetoresistance, the signature of the antilocalization effect, especially pronounced for x~0.03 film and the negative magnetoresistance, indicating the weak localization effect. Source: [35].

2.1.3. PbTe QWs

The investigation on the transport properties of PbTe QWs has been carried out over the last decades. During this time, very interesting features were provided for the basic physics point of view as well as for potential applications. Laser diode devices are one of the first applications for PbTe QWs once this material has a small band gap in the midinfrared spectral range with a wavelength around 2.5 μm – 6 μm [39-41]. Ishida *et al* (1986) [39] studied PbTe/EuTe multiple quantum wells (MQWs) grown using the hot wall technique. They analyzed their structural properties by x-ray diffraction and measured the optical and magnetoresistance properties. An MQW laser was prepared to obtain a pulsed laser of 4.4 μm. The quality was not good due to the fluctuations of EuTe compositions and other imperfections resulting from the low-quality sample growth using hot wall technique. Partin *et al*. [41, 42] have grown a single PbTe QW diode laser using MBE technique and found that the signal tuned from 6.45μm at T~13K to 4.41 μm at T~174 K and to 4.01 μm at T~241 K in the pulsed regime. Also, preliminary experiments showed that for a higher energy barrier, it was possible to achieve a temperature of operation of 260 K. This

demonstrates that the operating temperature depends on the height of the energy barriers. More recent works involving PbTe compounds are found in the literature involving laser diode devices with better quality samples and higher temperature of operation [2, 43].

PbTe QWs are also suitable for thermoelectric devices being among the best bulk thermoelectric materials in the temperature range of 500 K to 700 K [44, 45]. The MBE technique allows the manufacture of high-quality QWs samples with a lower thickness (down to 2 nm). Harman *et al.* [45] were the first ones to investigate the thermoelectric properties of PbTe/$Pb_{1-x}Eu_xTe$ MQWs growth over a BaF_2 substrate using the MBE technique. They found an enhancement in the figure of merit (ZT) from 0.45 (for bulk PbTe) to 1.2 in the best QW. The figure of merit is a well-defined metric to evaluate thermoelectric materials given by $ZT = S^2\sigma T/\kappa$ [46], where S is the seed back coefficient or thermoelectric sensitivity. It is a measure of the magnitude of an induced thermoelectric voltage in response to a temperature difference across the material. σ is the electric conductivity, κ is the thermal conductivity and T is the temperature. The enhancement is attributed to the large density of states per unit volume that occurs for small PbTe layer thickness. The investigative works about thermoelectric power devices applications for these materials remain active nowadays [47, 48].

Despite the device development interest, basic physics research also has a large potential in PbTe QWs. Integer quantum Hall effect (IQHE) and Shubnikov the Haas oscillations (SdHO) can be investigated, with great interest, once PbTe presents a non-conventional Fermi surface and large g factor. Springholz *et al.* (1993) [23] investigated the electronic properties of PbTe/$Pb_{1-x}Eu_xTe$ MQWs, regarding the Eu concentration in the structures. The results showed a decrease in the mobility of the $Pb_{1-x}Eu_xTe$ barriers with the increase of Eu content, indicating two-dimensional (2D) confinement of the carriers in the PbTe layer. This agrees with the discussion presented in the last section. For Eu concentration larger than x~0.047 the parallel conduction in the $Pb_{1-x}Eu_xTe$ is minimized, making possible to observe the IQHE and the SdHO (see Figure 2.6(a)). On the other hand, the non-zero minimum the SdH oscillations mean that remaining parallel conduction in the $Pb_{1-x}Eu_xTe$ layer still exists. This effect will be also present in some of the results presented in Chapter 4.

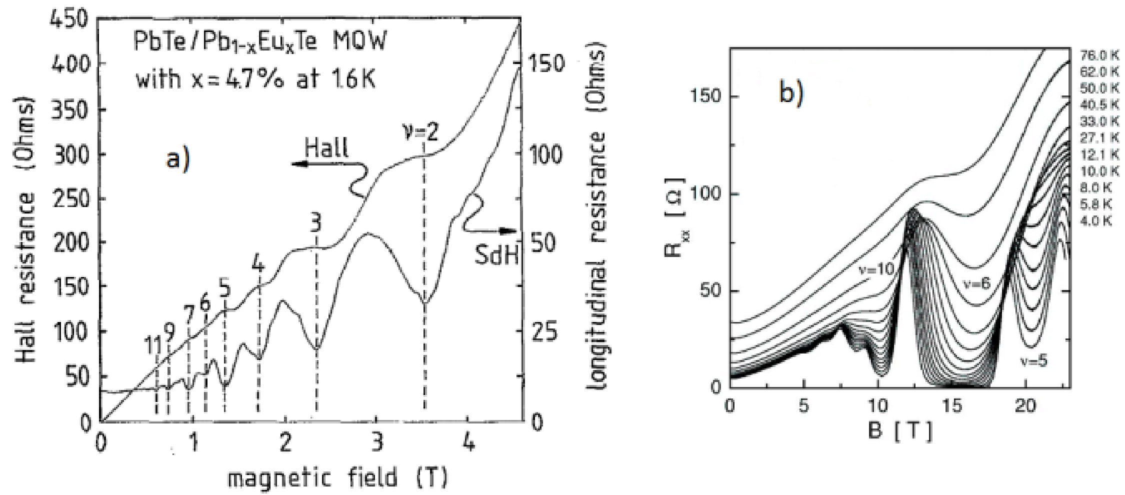

Figure 2.6 (a) Hall resistance (left scale) and longitudinal resistance (right scale) at 1.6K for PbTe/$Pb_{1-x}Eu_xTe$ MQW sample with x=0.047 as a function of the magnetic field applying a constant current of 100μA [23]. (b) Magnetic field dependence of the longitudinal resistance R_{xx} for increasing temperatures from 4 to 76K. Source: modified from [11].

One expects that if the Eu concentration in the barrier is increased, the parallel conduction should be reduced or suppressed. Chitta *et al.* (2005) [11] successfully investigated the IQHE in *n*-type PbTe/$Pb_{1-x}Eu_xTe$ QWs, with Eu concentration around x=0.1 in the barriers. Figure 2.6(b) shows the zero plateau for longitudinal resistance at B~15 T, indicating that the carriers conduction is fully occurring in the PbTe layer. They also explained the unusual filling factor sequence obtained taking into account the electron transference between the longitudinal and oblique valleys.

The large SO interaction mentioned before in PbTe is Rashba type, *i.e.*, caused by the asymmetry of the QW or heterojunction. Peres *et al*. (2014) [10] presented an experimental investigation of the SO coupling effect in *n*-type PbTe/$Pb_{1-x}Eu_xTe$ QWs by means of weak antilocalization effect. Using the model developed by Hikami, Larkin, and Nagaoka (HLN) [49] the zero filed spin-splitting was derived. Also, it was verified that the electron-electron interaction is one of the main scattering mechanisms in *n*-type PbTe quantum wells [10]. In another experiment, using a high asymmetric PbTe QW, Jin *et al*. (2009) [50] also observed large Rashba spin-splitting. In that case, the QW was intentionally grown with asymmetric barriers in CdTe/PbTe/PbSrTe structure.

The $PbTe/Pb_{1-x}Eu_xTe$ QWs investigated in this work, present a rich system to investigate all the effects cited above. Besides, our samples are *p*-type, and we expect to observe new features in the experimental data. We also guarantee that barriers are insulating enough to ensure hole confinement in the QWs. The parameters to be determined after the detailed investigation of these nanostructures must provide additional information for the questions that are still open regarding the Anderson localization and the Integer Quantum Hall effect. One powerful tool used to investigate samples in this work is the photoconductivity effect, presented in the next section.

2.2. Photoconductivity effect

Photoconductivity (PC) is the effect in which the conductivity of a solid is modified under illumination. Full understanding of this effect is crucial for fabrication and improvement of light-sensitive devices [51-53]. Moreover, photoconductivity measurements can provide important information about electrical properties as lifetime, mobility, charge carriers and impurity centers energy [54].

To understand the conductivity effect, it is necessary to know how electrons behave in semiconductor materials. In a solid, electrons can occupy many levels, frequently grouped as energy bands, but in a pure semiconductor crystal, the near Fermi level bands are called valence band (VB) and conduction band (CB), separated by a forbidden band, named energy gap (E_g) as shown in Figure 2.7. For an intrinsic semiconductor material, at T=0 K, the VB is fully occupied and CB is fully depleted. However, for a finite temperature, a considerable electron number (e^-) can “jump” from VB to CB, leaving empty states at the VB. These states behave like quasiparticles and are designated as holes (h^+). Therefore, the conduction can occur in VB by holes and in CB by electrons and the total electrical conductivity is the composition of both contributions (see Equation (2.4)).

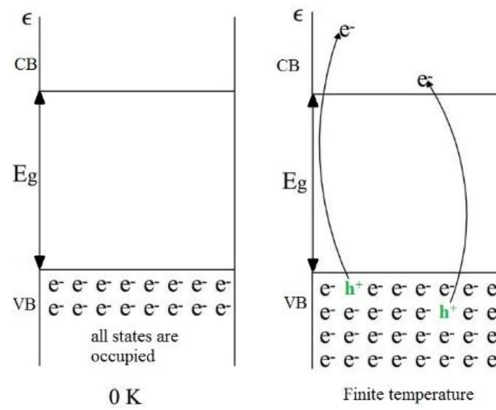

Figure 2.7. Schematic illustration of allowed bands in a pure semiconductor crystal, valence band (VB), conduction band (CB), and the forbidden energy gap (E_g) band show including carrier behavior for T=0 K and finite values.

The transition between the valence and conduction bands can be direct or indirect. The direct transition occurs when the top of the conduction band (E_c) and the bottom of the valence band (E_v) have the smallest gap in the same position of reciprocal lattice, as represented in Figure 2.8(a). The indirect transitions occur only assisted by phonons $(\hbar\omega_q)$ that transfer momentum to the electron while maintaining the conservation of the total momentum, as represented in Figure 2.8(b). Indirect transition is less likely than direct because it depends on the probability of an electron colliding with a compatible phonon. Some examples of indirect band gap semiconductors are Si, Ge and AlSb.

Quantitatively, electrical conductivity can be determined by:

$$\sigma_0 = e\left(n_0\mu_{n_0} + p_0\mu_{p_0}\right) \tag{2.4}$$

where n_0 and p_0 are the electron and hole concentration, respectively, μ_{n_0} and μ_{p_0} are the electron and hole mobility and e is the electron charge.

Another way to promote an electron to the CB is by applying light. If the incident photon energy is equal to or greater than the E_g, the electrons in the VB can absorb a photon $(\hbar\omega)$ and be promoted to the CB. When this occurs, the conductivity varies according to:

$$\Delta\sigma = \sigma_L - \sigma_0 \tag{2.5}$$

where σ_L is the conductivity when the material is under illumination.

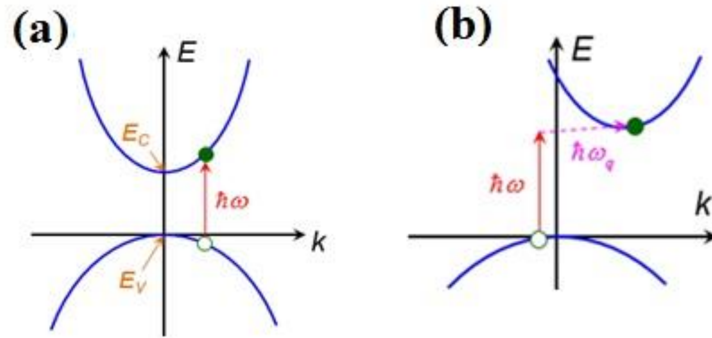

Figure 2.8. Schematic illustration of photoconduction effect by (a) direct and (b) indirect transition (with the help of the network phonon).

Assuming only one carrier type participating in the process, Equation 2.4 is reduced to $\sigma_0 = en_0\mu_0$. Therefore, Equation 2.5 can be rewritten and expanded as:

$$\sigma_L = \sigma_0 + \Delta\sigma = e(n_0 + \Delta n)(\mu_0 + \Delta\mu)$$

$$\Delta\sigma = e(n_0 + \Delta n)(\mu_0 + \Delta\mu) - en_0\mu_0$$

$$\Delta\sigma = e(n_0\Delta\mu + \mu_0\Delta n + \Delta n\Delta\mu)$$

$$\Delta\sigma = e\mu_0\Delta n + e\Delta\mu(n_0 + \Delta n) \tag{2.6}$$

Equation (2.6) shows that the conductivity variation under illumination may exhibit negative values, since it depends on the variation in the concentration and carrier mobility. For example, Tavares *et al.* (2017) [55] performed photoconductivity measurements using infrared LED on $Pb_{0.66}Sn_{0.44}Te$ films in the 85 K to 300 K temperature range and observed negative photoconductivity (see Figure 2.9). The observed negative effect was attributed to the carriers that are trapped in the defect levels created by the disorder. In this case, the trapping mechanism plays an important role in the generation and recombination rates that are temperature sensitive.

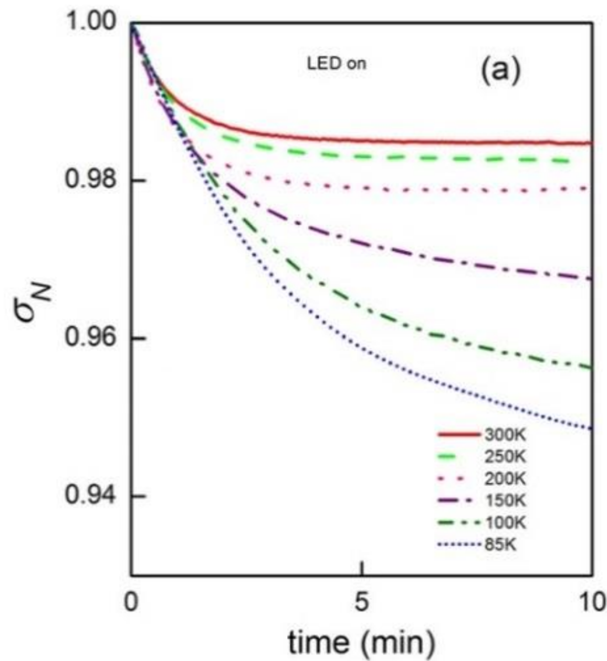

Figure 2.9 Normalized time-dependent photoconductivity for $Pb_{0.66}Sn_{0.44}Te$ film in the temperature range of 85–300 K under illumination. Source: modified from [55]

Another observable effect that can be caused by defects is the persistent photoconductivity (PPC) discussed in the next section.

2.2.1. Persistent photoconductivity effect (PPC)

The electron generation from the valence band (VB) to the conduction band (CB) is always followed by electron recombination from the CB to the VB. During the recombination process, however, carriers can be trapped by some potential barrier inside the band gap, caused by vacancies, interstices or impurities. When the carriers are trapped, the recombination time is longer when compared to a crystalline intrinsic sample, impurity free, and the recombination process can take long time periods to reach the ground state. This effect is known as persistent photoconductivity (PPC) and is an useful tool for investigating defect states in semiconductors. The persistence effect is well reported in the literature for different semiconductor materials as

materials based on PbTe [35, 36] and GaAs [56, 57]. Castro *et al.* [58] observed PPC, as shown in Figure 2.10, in *p*-type intrinsic PbTe and BaF_2-doped PbTe at T~300 K. At t=0, the LED is turned on, increasing the carrier density participating in conduction. When the light is turned off (see arrows), a long tail appears on the resistance as a time function, indicating the PPC effect presence.

Some mechanisms are proposed to explain the persistent effect. The most accepted are based on the existence of potential energy barriers that arise due to the surfaces, interfaces and impurities effects. These microscopic defects generate carrier trapping points, also called traps, slowing down the recombination process [59].

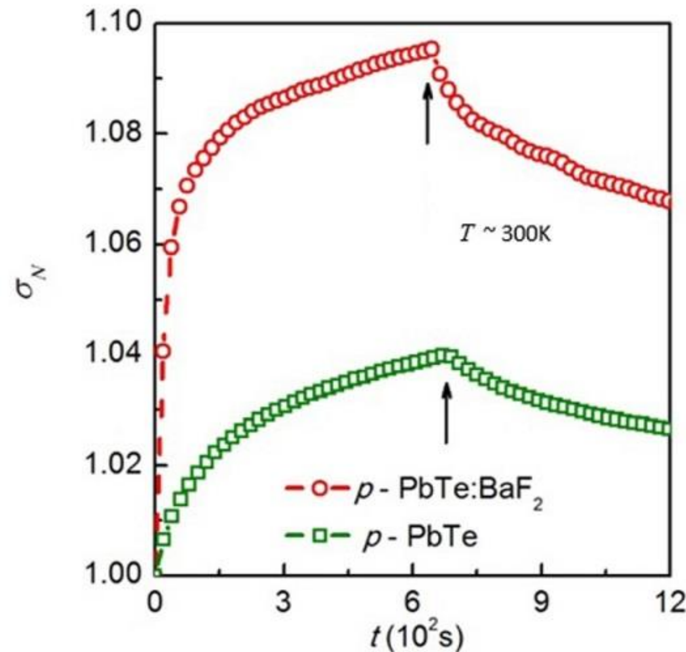

Figure 2.10 Photoconductivity normalized (σ_N) at t=0 under illumination by the blue LED for the undoped p-PbTe sample (open square) and *p*-PbTe:BaF_2 (open circles) at T=300 K. The arrows indicate the lighting shutdown. Both samples exhibit PPC effect after switching off the light. Source: [58]

The conductivity during the recombination process, when PPC is present in the system, exhibits an exponential decay profile, as in Figure 2.10, and can be described as [34]:

$$\sigma = \sigma_0 exp\left(\frac{-t}{\tau}\right) \tag{2.7}$$

where τ is the recombination time and can be expressed as [60]:

$$\tau = \tau_0 exp\left(\frac{\Delta\varepsilon}{k_B T}\right) \quad (2.8)$$

where $\Delta\varepsilon$ is the activation energy, which is the energy difference between the recombination center and the band edge.

One can also study the PPC effect on semiconductors if a random potential modulates the energy bands, as represented in Figure 2.11 by the green line. Considering a semiconductor with random potential relief $U(r)$ [61], this random potential is characterized by percolation levels (E_p) [62]. It is not easy to calculate the precise value of these percolation level. Fortunately for a 2D structure, it corresponds to the average value of the energy bands, in other words $E_p^e \equiv E_C$ and $E_p^h \equiv E_V$, for *p* and *n*-type semiconductors respectively. For a 3D structures, the potential relief value is reduced [63].

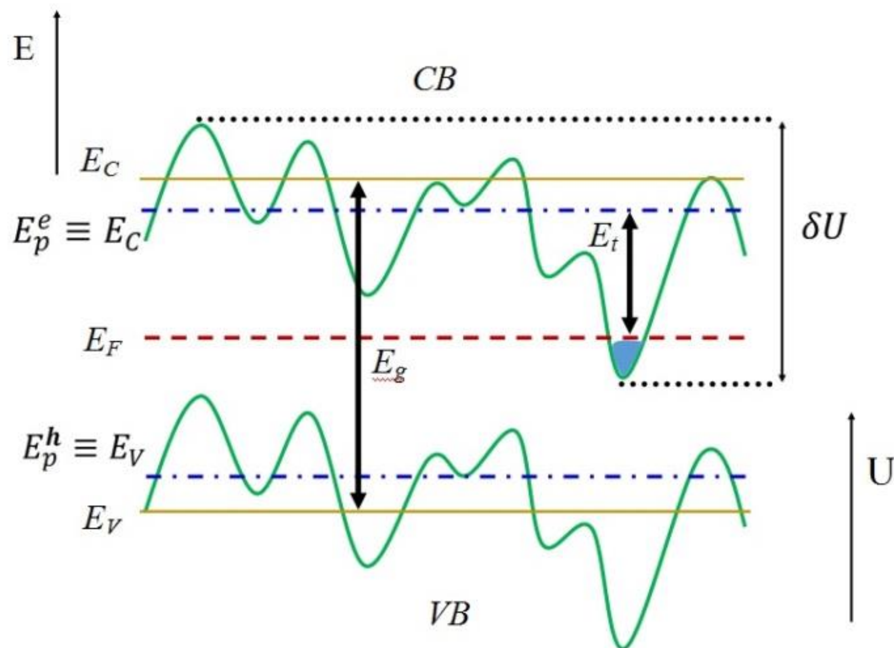

Figure 2.11 Figure 2.12 Schematic representation of the random potential in band energy. EC and EV are the conduction and valence band energy respectively; E_p^e and E_p^h are the percolation energy for electron and hole respectively; E_F is the Fermi energy; E_g is the energy gap; $E_t = E_p^e - E_F$ is the potential barrier energy high due to trap level for *n*-type material; δU is the random potential amplitude and the cross-hatched area between Fermi level and the random potential are localized states.

Mathematically, Shik *et al.* [61] showed that the random potential leads to a trap with an energy barrier height E_t given by:

$$E_t = \frac{e^2 {N_t}^{2/3}}{\epsilon n_0^{1/3}} \tag{2.9}$$

where ϵ is the dielectric constant, n_0 is the free carrier density and N_t is the defect center density. N_t that can be extracted from linear magnetoresistance (LMR), which will be discussed in section 2.4.

Therefore, the PC effect can be used to obtain the energy depth of the impurity levels within the band gap and the recombination times as well.

2.3. Hall effect

Hall effect is an important tool to characterize materials, providing necessary information about electrical transport parameters, such as carrier concentration, carrier mobility, transport dimensionality, and spin effects. The Hall effect is separated into two different types: the classic Hall effect (CHE) and quantum Hall effect (QHE). In this section, we focus on the classical Hall Effect.

The CHE is a phenomenon that occurs due to the carrier accumulation on the sample borders caused by the charge scattering induced by an applied magnetic field *B*. The distance between the two magnetic poles, called magnetic length (l_B), in this case, corresponds to circular orbit performed by the carrier, which depends on the *B* intensity. As *B* increases, l_B decreases to the point where the particle no longer collides with the material border. Instead, it will perform a circular movement in a *x-y* plane with angular frequency ω_c, that causes a change in the curve profile from which is the signature of the quantum Hall effect (QHE). In this section, we will briefly describe the Hall effect, first the CHE and then the QHE.

2.3.1. Classic Hall effect

The classical Hall effect can be derived from the Drude model. This model treats the solid as a fixed array of atoms in a free electron gas. In addition, the electrons do not interact with each other and are randomly scattered by the fixed atoms. In this model, the electron moves in a metallic material in the direction of an applied electric field (E). Figure 2.13 shows a representation of a metallic material under a magnetic field applied in the z-direction and an electric field applied in the x-direction. The sample dimensions are d, w, and l, and an electron current (I) is flowing in the x-direction. In this situation, the electron suffers the influence of the electric (F_E) and magnetic (F_B) forces. Initially, the electrical force is in the same direction as E, but due to the charge accumulation in the borders, the total electric field must be composed of two components such as $\vec{E} = \vec{E}_x\hat{\imath} + \vec{E}_y\hat{\jmath}$.

From Newton´s second law:

$$\overrightarrow{F_B} + \overrightarrow{F_E} + \frac{m\vec{v}}{\tau} = m\frac{d\vec{v}}{dt} \tag{2.10}$$

where $\vec{v}$ is the average velocity vector, m is the carrier mass, t is time and τ is the average time between collision. In the equilibrium, $\frac{d\vec{v}}{dt} = 0$ and since B is applied in the z direction and the electron is moving in the plane x-y, this equation can be written as:

$$E_x\hat{\imath} + E_y\hat{\jmath} = \left(-\frac{m}{e\tau}v_x - v_yB\right)\hat{\imath} + \left(v_xB - \frac{m}{e\tau}v_y\right)\hat{\jmath} \tag{2.11}$$

In matrix form it can be expressed as:

$$\begin{pmatrix} E_x \\ E_y \end{pmatrix} = \begin{pmatrix} -\frac{m}{e\tau} & -B \\ B & -\frac{m}{e\tau} \end{pmatrix} \begin{pmatrix} v_x \\ v_y \end{pmatrix} \tag{2.12}$$

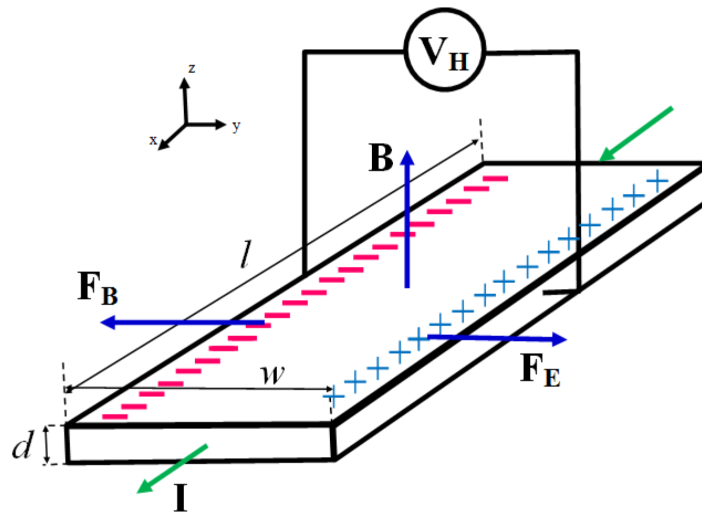

Figure 2.13 Schematic illustration of a semiconductor or metallic material with dimensions *d, w* and *l*. An electric field applied in the *x*-direction, generating an electron current I in the *x*-direction. A magnetic field *B* is applied in the *z*-direction, generating a magnetic force (F_B) in the *y*-direction, causing the carriers accumulated in the side of the material and appearing a Hall voltage (V_H).

From the relation $\vec{J} = ne\bar{v}$, where $\vec{J}$ is the current density vector and n is the electron concentration:

$$\begin{pmatrix} J_x \\ J_y \end{pmatrix} = -ne \begin{pmatrix} v_x \\ v_y \end{pmatrix} \quad or \quad \begin{pmatrix} v_x \\ v_y \end{pmatrix} = -\frac{1}{ne} \begin{pmatrix} J_x \\ J_y \end{pmatrix} \tag{2.13}$$

using Equation 2.13 in 2.12:

$$\begin{pmatrix} E_x \\ E_y \end{pmatrix} = \begin{pmatrix} \frac{m}{ne^2\tau} & \frac{B}{ne} \\ -\frac{B}{ne} & \frac{m}{ne^2\tau} \end{pmatrix} \begin{pmatrix} J_x \\ J_y \end{pmatrix} \tag{2.14}$$

The current density is $\vec{J} = \sigma\vec{E}$, σ is the electrical conductivity and $\rho = 1/\sigma$ is the electrical resistivity. To find the conductivity matrix, we use the matrix rule $\sigma \times \sigma^{-1} = I_0$, where I_0 is the identity matrix in the form

$$\begin{pmatrix} a & b \\ c & d \end{pmatrix} \begin{pmatrix} \frac{m}{ne^2\tau} & \frac{B}{ne} \\ -\frac{B}{ne} & \frac{m}{ne^2\tau} \end{pmatrix} = \begin{pmatrix} 1 & 0 \\ 0 & 1 \end{pmatrix}$$

$$\begin{vmatrix} \left(a\frac{m}{ne^2\tau}-\frac{bB}{ne}\right) & \left(\frac{bB}{ne}+b\frac{m}{ne^2\tau}\right) \\ \left(c\frac{m}{ne^2\tau}-\frac{dB}{ne}\right) & \left(\frac{cB}{ne}+d\frac{m}{ne^2\tau}\right) \end{vmatrix} = \begin{vmatrix} 1 & 0 \\ 0 & 1 \end{vmatrix} \tag{2.15}$$

Solving Equation 2.15 we find the conductivity matrix:

$$\begin{vmatrix} \sigma_{xx} & \sigma_{xy} \\ \sigma_{yx} & \sigma_{yy} \end{vmatrix} = \frac{ne^2}{m} \begin{vmatrix} \left(\frac{\tau}{1+\omega_c^2\tau^2}\right) & \left(-\frac{\omega_c\tau^2}{1+\omega_c^2\tau^2}\right) \\ \left(\frac{\omega_c\tau^2}{1+\omega_c^2\tau^2}\right) & \left(\frac{\tau}{1+\omega_c^2\tau^2}\right) \end{vmatrix} \tag{2.16}$$

where ω_c is the cyclotron frequency. A classic electron under a magnetic field in the *z* direction and moving in the *x*-*y* plane will perform a circular trajectory with angular velocity:

$$\omega_c = \frac{eB}{m} \tag{2.17}$$

$\vec{J} = \vec{\sigma}\vec{E}$ in the matrix form:

$$\begin{vmatrix} J_x \\ J_y \end{vmatrix} = \begin{vmatrix} \sigma_{xx} & \sigma_{xy} \\ \sigma_{yx} & \sigma_{yy} \end{vmatrix} \begin{vmatrix} E_x \\ E_y \end{vmatrix} \tag{2.18}$$

From equation 2.16 we assume that $\sigma_{xx} = \sigma_{yy}$ and $\sigma_{xy} = -\sigma_{yx}$. Besides, at equilibrium $J_y = 0$ and $J_x = I_x/A$, where A is the cross-sectional area of the surface where the current is flowing. From these considerations and solving the matrix in Equation 2.18 we obtain:

$$\sigma_{xx}E_x + \sigma_{xy}E_y = J_x$$
$$-\sigma_{xy}E_x + \sigma_{yy}E_y = 0$$

Solving these systems for J_x:

$$J_x = E_y\left(\frac{{\sigma_{xx}}^2+{\sigma_{xy}}^2}{\sigma_{xy}}\right) \tag{2.19}$$

From 2.16 and 2.18 we have that $\sigma_{xy} = \sigma_{xx}\omega_c\tau$, then:

$$J_x = E_y\frac{ne^2}{m\omega_c} \tag{2.20}$$

replacing ω_c:

$$\frac{E_y}{J_x} = \frac{B}{ne} \tag{2.21}$$

Using Van der Pauw geometry it is possible to consider the cross-sectional area as a square, according to Figure 2.13, $A=wd$ and replacing $J_x = I_x/w.d$ and $E_y = V_y/w$ we have:

$$\frac{V_y}{I_x} = \frac{B}{dne} \tag{2.22}$$

That can be written as:

$$R_{xy} = R_H \frac{B}{d} \tag{2.23}$$

where R_{xy} is the Hall resistance and R_H is the Hall factor. For a 2D structure, where the thickness is negligibly, it is given by:

$$R_H = \frac{1}{ne} \tag{2.24}$$

According to Figure 2.14, where R_{xy} is plotted as a function of *B*, it is possible to obtain the carriers concentration from the slope, using the Equation 2.24.

The electronic mobility (μ) of the carriers can also be extracted. From Equation 2.16 we have:

$$\sigma_{xx} = \frac{ne^2}{m}\left(\frac{\tau}{1+\omega_c^2\tau^2}\right) \tag{2.25}$$

When $B=0$, the cyclotron frequency is $\omega_c = 0$. $\mu = e\tau/m$, and $\rho = 1/\sigma$, for a 2D material we have $R_{xy} = \rho_{xy}$. Therefore for $B=0$:

$$R_0 = \frac{1}{n.e.\mu} \tag{2.26}$$

$$\mu = \frac{1}{neR_0} = \frac{R_H}{R_0} \tag{2.27}$$

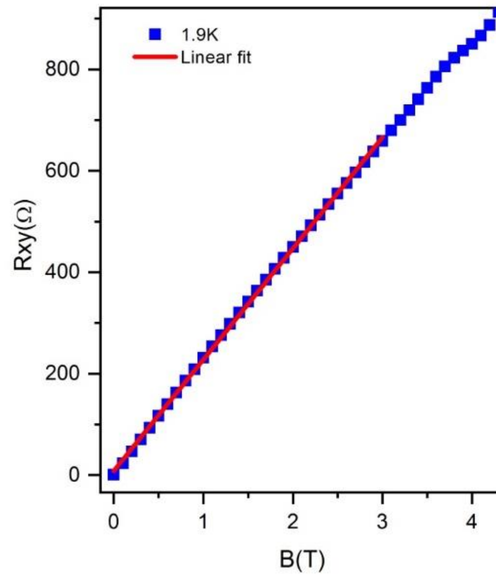

Figure 2.14 Hall resistance (R_{xy}) as a function of B for a 10 nm thick PbTe/$Pb_{0.9}Eu_{0.1}Te$ QW. The red line is a linear fit to obtain the Hall factor in accordance with Equation 2.49.

The classic analysis is valid for low values of B when the curve profile is linear. If B is increased and reach the limit $\tau_i\omega_c > 1$, the classic prediction fails. The curve profile can change, presenting some plateaus and entering in the quantum domain, where-interesting effects happen. The QHE is treated in detail in the next section.

2.3.2. Quantum Hall effect

At low temperatures and high magnetic fields, the classic Hall effect, as mentioned, no longer describes the phenomenon observed. As B increases, the magnetic length (l_B), given by Equation 2.28, decreases until the particle makes a circular motion in the x-y plane. This causes a linear profile change in plotting the R_{xy} curve for the appearance of some plateaus, which characterizes the quantum Hall effect (QHE) domain.

$$l_B = \sqrt{\frac{\hbar}{eB}} \tag{2.28}$$

This effect was first observed by Von Klitzing in 1980 [64] and exhibit the profile shown in Figure 2.15, where R_{xy} and R_{xx} were measured for a $GaAs/Al_xGa_{1-x}As$ heterostructure. Both resistances presented interesting behavior. Resistance plateau appears for one interval B and then jump to another plateau. In addition, the resistivity in these plateaus is quantized. The effect on R_{xx} resistance is discussed in Section 2.4.

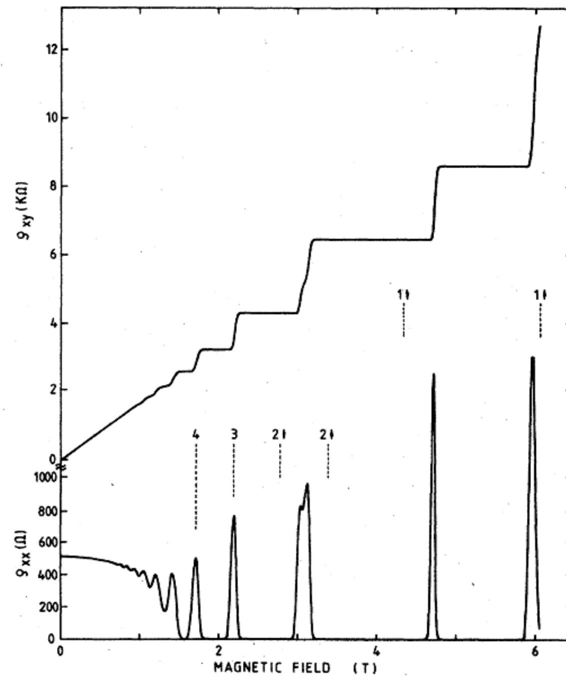

Figure 2.15 Experimental curves for Hall resistance ($R_{xy} = \rho_{xy}$) and resistivity $\rho_{xx} \sim R_{xx}$ of a heterostructure as a function of the magnetic field at a fixed carrier density corresponding to a gate voltage $V_g = 0\ V$. The temperature is around 8mK. Source: [64].

To understand the QHE, first we solve the Schrödinger equation using the Landau-Gauge method. For a planar sample under an orthogonal and uniform magnetic field the Hamiltonian is:

$$H = \frac{(\vec{p} - q\vec{A})^2}{2m} \tag{2.29}$$

where q is the charge and $\vec{A}$ is the magnetic potential vector:

$$\vec{B} = \vec{\nabla} \times \vec{A} \tag{2.30}$$

From Equation 2.29 we obtain the Schrodinger equation:

$$\frac{(\vec{p}-q\vec{A})^2}{2m}\psi = E\psi \tag{2.31}$$

$$\frac{1}{2m}\left(-i\hbar\vec{\nabla} - q\vec{A}\right)^2\psi = \psi \tag{2.32}$$

Considering a uniform magnetic field in $\hat{z}$ direction and choosing the potential vector as $\vec{A} = (0, Bx, 0)$ we can rewrite Equation 2.32 as:

$$\left[-\frac{\hbar^2}{2m}\frac{d^2}{dx^2} + \frac{1}{2}m\omega_c^2\left(x + \frac{\hbar k}{eB}\right)^2\right]u(x) = \varepsilon u(x) \tag{2.33}$$

Equation 2.33 is the Schrödinger equation for the harmonic oscillator with a radius described by Equation 2.28. k is wavelength and $u(x)$ is the random potential. The wave functions and their solutions for the electron movement in the *x-y* plane, when *B* is applied, are described by Equations 2.34 and 2.35 respectively:

$$\phi_{nk}(x,y) \propto H_{n-1}\left(\frac{x-x_k}{l_B}\right) exp\left[-\frac{(x-x_k)^2}{2{l_B}^2}\right] exp(iky) \tag{2.34}$$

$$\varepsilon_{nk} = \left(n + \frac{1}{2}\right)\hbar\omega_c \;\; (independent\ of\ k) \tag{2.35}$$

where n = 1, 2, 3, … are integers and H_n are the Hermit polynomials. The solutions of Equation 2.35 show that energy depends on n instead of k, so the states with the same n, but different k are degenerated as shown in Figure 2.16.

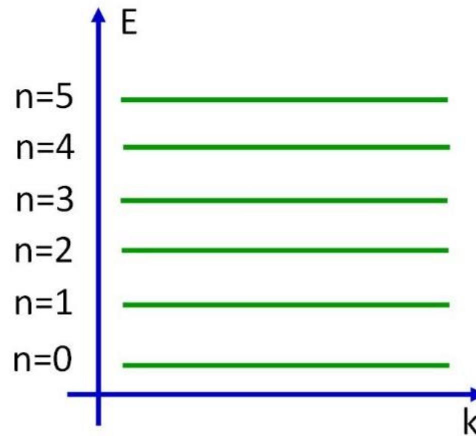

Figure 2.16 Energy levels degeneracy. Modified from [65].

For high magnetic fields, the 2D density of the states collapses giving rise to the delta functions δ, called Landau Levels (LL) shown in Figure 2.17(a) with energies values given by Equation 2.35.

The number of states allowed in each LL per unit area considering the spin degeneration and the cyclotron energy ($\hbar\omega_c$) must be exactly the same number of states given by the classic 2D band model:

$$N_B = \frac{2eB}{h} = \frac{2m\omega_c}{2\pi\hbar} = \frac{m}{\pi\hbar}\hbar\omega_c \tag{2.36}$$

Equation 2.36 represents an ideal system, however, in real materials the disorder effect is always present, causing the electron scattering in a finite average time interval (τ_i). This time interval is called quantum lifetime and differs from a transport lifetime (τ). In addition, the disorder effect causes a broadening (Γ) of the LL delta functions. This enlargement is show in Figure 2.17(b) and is written as:

$$\Gamma = \frac{\hbar}{\tau_i} \tag{2.37}$$

If the limit $\hbar\omega_c > \Gamma$ is reached, the separation between LL increases promoting a greater enlargement of the delta functions and significant changes in the state density as shown in Figure 2.17(c). This limit can be written as $\tau_i\omega_c > 1$ and is the limiting factor between classic (low fields) and quantum (high fields) Hall effect domain.

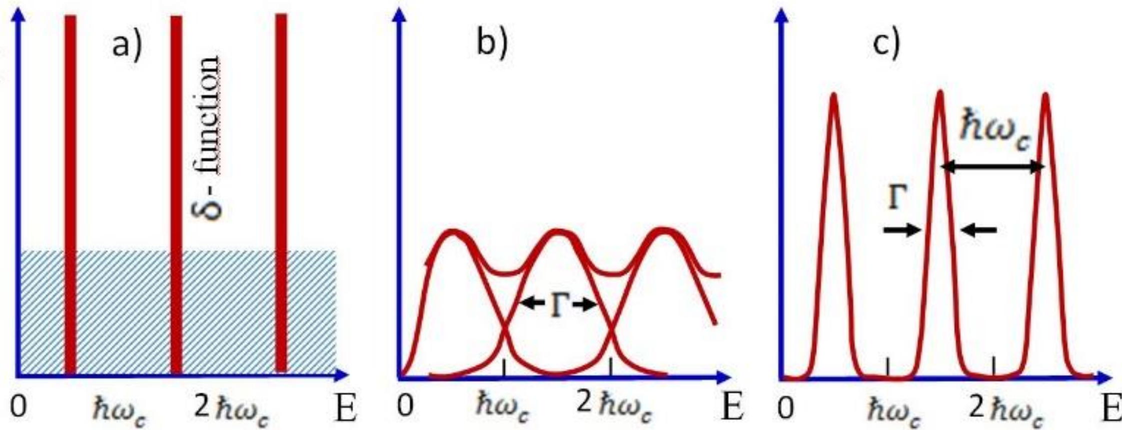

Figure 2.17 Density of states neglecting the spin effect. States that were continuous, concentrated in the Landau levels. (a) the ideal system, with the δ-functions. (b) A more realistic system when the Landau levels are broadening (Γ) due to the disorder present in the material. (c) By raising B, the levels become more distinct if $\hbar\omega_c > \Gamma$, ou $\tau_i\omega_c > 1$. Modified from: [66].

When the magnetic field increases beyond $\tau_i\omega_c > 1$, the separation $\hbar\omega_c$ and the number of states supported by each LL increase. To keep constant the state density, the number of occupied LL (filling factors - v) must change as a function of B , as shown in Figure 2.17 according to:

$$v = \frac{n_{2D}}{N_B} = \frac{hn_{2D}}{eB} = 2\pi l_B^2 n_{2D} \tag{2.38}$$

n_{2D} is the carrier density in two dimensions. If v is an integer, it is called the integer quantum Hall effect (IQHE). If v is not an integer, it is called the fractional quantum Hall effect (FQHE).

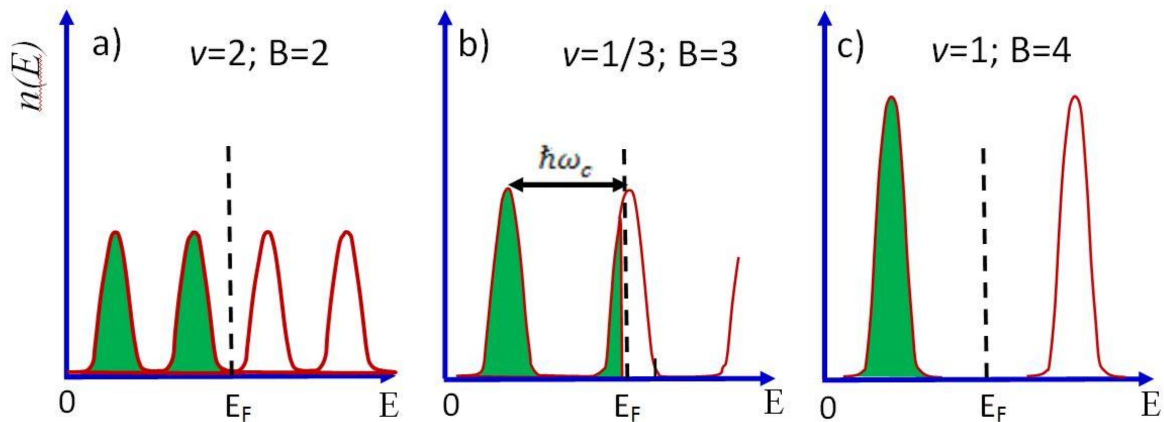

Figure 2.18 Illustrative representation of Landau level occupation, neglecting the spin effect. Showing how the Fermi level changes to accommodate the electrons while maintaining the constant state density. *a) B=2 e* $v = 2$. *b) B=3* $v = \frac{1}{3}$. *c) B=4* $v = 1$. Source: modified from [66].

To observe the LL with good resolution, a high-quality sample is required and $k_B T \ll \hbar\omega_c$, i.e., low temperatures and high magnetic fields are required. When these criteria are satisfied, LL separation causes the transversal resistance (R_{xy}) quantization according to Equation 2.39, and R_{xy} shows plateaus, as shown in Figure 2.18 [64-66].

$$R_{xy} = \frac{h}{e^2}\frac{1}{v} \tag{2.39}$$

h/e^2 is the resistivity quantum also named as Von Klitzing constant, after Klaus von Klitzing, Nobel Prize winner for the IQHE discovery [64]. The magnetic field corresponding to the center of the plateaus can be calculated, according to Equation 2.23 and 2.24, $\left(R_{xy} = B/ne\right)$ and Equation 2.39 we have:

$$B = \frac{nh}{ev} \tag{2.36}$$

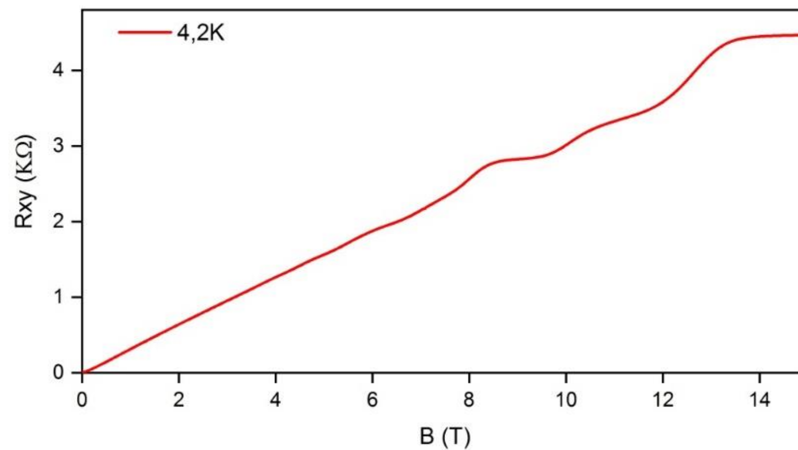

Figure 2.19 Experimental curves of R_{xy} (full line) as a function of B for a n-type PbTe/$Pb_{0,9}Eu_{0,1}Te$ QW at T~4.2 K.

Magnetic field also affects the longitudinal resistance, R_{xx}, as show next in a classical and quantum limits.

2.4. Magnetoresistance

Magnetoresistance (MR) occurs in metals and semiconductor materials and is the change in electrical resistance under an applied magnetic field. For nonmagnetic materials, in low fields, the effect is small, but can become very large for high fields and low temperatures. In addition, MR can change the profile depending on the angle between B and the sample surface.

The first theoretical treatment for this effect was by R. Gans in 1906 [67]. Since then much effort has been made to elucidate the different experimental MR results that appear. In this section, we will discuss the classic magnetoresistance (CMR), linear magnetoresistance (LMR) and the Shubnikov-de Haas (SdH) oscillations.

2.4.1. Classic Magnetoresistance

The classic magnetoresistance presents a quadratic profile at low B and saturating at a constant value for higher fields. We can derive a mathematical relation applying the same initial Hall effect arguments from section 2.3, using Equation 2.19 and remembering that $J = \sigma E$, we have:

$$\sigma_{xy} = \frac{{\sigma_{xx}}^2 + {\sigma_{xy}}^2}{\sigma_{xy}} \tag{2.41}$$

$$\sigma_{xx} = \frac{{\sigma_{xx}}^2 + {\sigma_{xy}}^2}{\sigma_{xx}} \tag{2.42}$$

Consequently, as $\rho = \sigma^{-1}$ we have:

$$\rho_{xy} = \frac{\sigma_{xy}}{{\sigma_{xx}}^2 + {\sigma_{xy}}^2} \tag{2.43}$$

$$\rho_{xx} = \frac{\sigma_{xx}}{{\sigma_{xx}}^2 + {\sigma_{xy}}^2} \tag{2.44}$$

For low *B* the resistivity variation $(\Delta\rho)$ is low, so that $\rho \rightarrow \rho_0$, where ρ_0 is the resistivity at *B*=0. With this assumption and using the magnetoresistance definition, we have:

$$\frac{\Delta\sigma}{\sigma_0} = \frac{\sigma_{xx} - \sigma_0}{\sigma_0} = \frac{\frac{1}{\rho_{xx}} - \frac{1}{\rho_0}}{\frac{1}{\rho_0}} = \frac{\rho_0 - \rho_{xx}}{\rho_{xx}} \tag{2.45}$$

Since $\rho \rightarrow \rho_0$:

$$\frac{\Delta\sigma}{\sigma_0} = \frac{\rho_0 - \rho_{xx}}{\rho_{xx}} = \frac{\rho_0 - \rho_{xx}}{\rho_0} = -\frac{\Delta\rho}{\rho_0} \tag{2.46}$$

Using Equation 2.44 in 2.46 and $\omega_c = eB/m$, we have:

$$-\frac{\Delta\rho}{\rho_0} = \frac{\frac{ne^2}{m}\left(\frac{\tau}{1+\omega_c^2\tau^2}\right) - \frac{ne^2}{m}}{\frac{ne^2}{m}}$$

$$-\frac{\Delta\rho}{\rho_0} = \left(\frac{1}{1+\frac{e^2B^2}{m^2}\tau^2}\right) - 1 \tag{2.47}$$

A Equation 2.47 simulation is shown in Figure 2.19. The insert shows the exponential profile at low *B*. When *B* is raised, the profile changes and begins to saturate to high *B*.

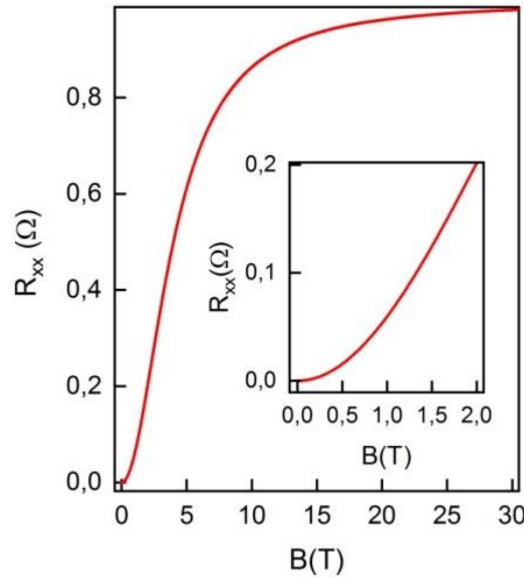

Figure 2.19 R_{xx} simulation curve as a *B* function according to Equation 2.47, the inset shows the exponential profile at low *B*.

If we assume low values of *B*, the term $\omega_c^2\tau^2$ is very small and (2.47) can be expanded in the first order in Taylor series. Equation 2.47 can be rewritten as:

$$-\frac{\Delta\rho}{\rho_0} = \left(1 - \frac{e^2\tau^2}{m^2}B^2\right) - 1$$

$$\frac{\Delta\rho}{\rho_0} = \frac{e^2\tau^2}{m^2}B^2 \tag{2.48}$$

The electron mobility is $= e\tau/m$, so the above relation becomes:

$$\frac{\Delta\rho}{\rho_0} = \mu^2B^2 \tag{2.49}$$

This means that for low magnetic field values, the curve presents a parabolic profile.

2.4.2. Shubnikov-de Haas Oscillations

Figure 2.20(a) shows R_{xx} for a SnTe/BaF_2 sample. The oscillation pattern that appears in R_{xx}, for B > 7.5 T, can be understood when we consider the Landau broadening of Equation 2.37 to calculate the state density (DOS). For a 2D semiconductor, it becomes [11]: [Figure 2.21(a) shows Rxx for a SnTe/BaF2 sample. The oscillation pattern that appears in Rxx, for B > 7.5 T, can be understood when we consider the Landau broadening of Equation 2.37 to calculate the state density (DOS). For a 2D semiconductor, it becomes

$$DOS(\varepsilon) = \frac{eB}{h}\frac{1}{\Gamma\sqrt{2\pi}} exp\left[\frac{-(\varepsilon-\varepsilon_n)^2}{2\Gamma^2}\right] \tag{2.50}$$

where ε_n is given by Equation 2.35. The Fermi energy, obtained from the DOS oscillation is show in Figure 2.20(b), where the LL energies for different quantum numbers, including spin-splitting, are simulated together with the Fermi energy represented by the blue line.

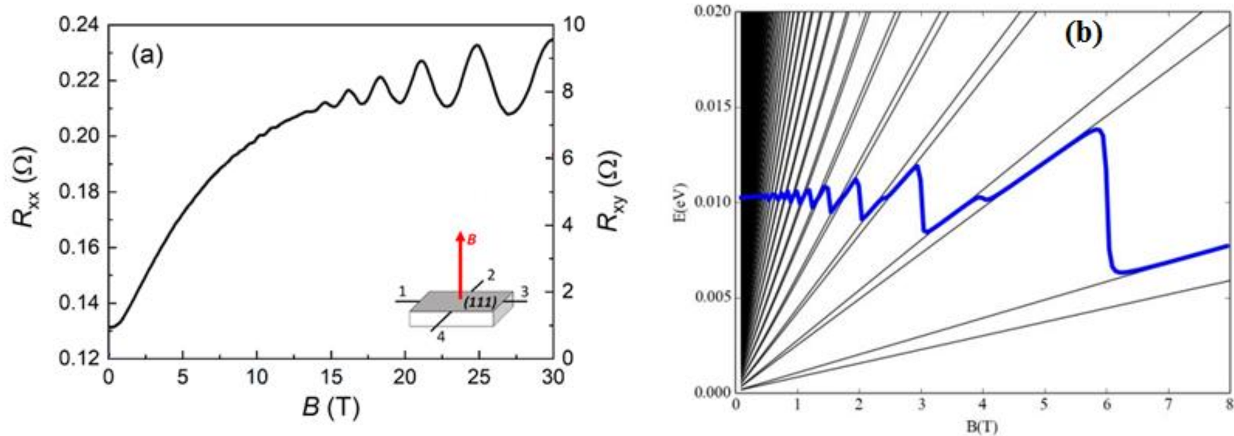

Figure 2.20 (a) Longitudinal resistance R_{xx} measured at 4.2 K as a function of a perpendicular magnetic field B in the SnTe/BaF_2 sample. For B< 7.5 T, the classic MR profile is present and for B>7.5 T Shubnikov-de Hass oscillations appear. Source: Modified from [68]. (b) Landau Level energy simulation of the 2D different quantum numbers, including spin splitting with increasing magnetic field. The big blue line is the Fermi energy, which represents the oscillations seen in measurements due to the change in the DOS. Source: Modified from Inge

Therefore, from Equation 2.50 the oscillation of the DOS is justified. The oscillations reverberate and can be seen on the R_{xx} curve if the LL splitting is greater than the Landau

broadening. This condition is generally satisfied at low temperatures if $k_BT \ll \hbar\omega_c$ and high magnetic fields if $\tau_i\omega_c > 1$. Lifshitz and Kosevich [69] describe this behavior mathematically as:

$$\rho_{xx} \propto R_T R_D R_S \sin\left(\frac{2\pi F}{B} + \phi\right) \tag{2.51}$$

The Equation 2.51 first term, R_T, is the temperature dependent part, also called the damping term, given by:

$$R_T = A_0 \frac{\alpha m^* \frac{T}{B}}{\sinh\left(\alpha m^* \frac{T}{B}\right)} \tag{2.52}$$

with $\alpha = 2\pi^2 k_B/\hbar e$, where A_0 is an adjustment constant that depends on the material; m^* is the effective mass and k_B the Boltzmann constant. The second, R_D, is the Dingle term, related to the finite quantum lifetime of the electrons and can be expressed as:

$$R_D = exp\left(\frac{\pi^2 k_B m^*}{\tau_i e B}\right) \tag{2.53}$$

where R_S is the term related to spin:

$$R_S = \cos\left(\frac{\pi g m^*}{2m_0}\right) \tag{2.54}$$

where g is the Landé factor and m_0 is the rest mass.

These four Equations (2.51; 2.52; 2.53 and 2.54) allow us obtain the fundamental frequencies of the oscillations, effective mass, quantum lifetime, Landau broadening (using Equation 2.37), g factor and the carrier concentration that can be obtained, since:

$$2\pi(\nu + \gamma) = \pi k_F^2 \frac{\hbar}{eB} \tag{2.55}$$

For two-dimensional electron gas:

$$n = n_{2D} = \frac{k_F^2}{4\pi} \tag{2.56}$$

where k_F is the Fermi wave vector and γ is a phase shift that must be zero for normal fermions [70-73].

In addition, it is possible to obtain information about the Fermi surface of the material. Since frequency depends only on the *B* perpendicular component and it is related to the extreme cross-section (A) of the Fermi surface by Onsager relation [74] expressed in Equation 2.57,

$$F = \frac{\hbar A}{2\pi e} \tag{2.57}$$

According to this relation, if the angle between the sample and applied *B* changes, the frequencies must change to anisotropic Fermi surfaces and remains constant for isotropic surfaces. In addition, a fundamental oscillation frequency can be obtained by replacing Equation 2.57 in 2.55, since $A = \pi {k_F}^2$ and considering normal fermions:

$$\nu = \frac{F}{B} + \gamma \tag{2.58}$$

That is, if the filling factors are plotted as a function of 1/*B*, the frequency can be obtained directly from the slope of the curve.

Moreover, from the SdH oscillations, it is possible to obtain the *g* factor value, provided that the Zeeman effect is sufficiently strong so that the separation can be observed in the R_{xx} oscillations. Taking the total electronic energy, considering the Landau level and the spin splitting:

$$\varepsilon_{n\pm} = \left(n + \frac{1}{2}\right)\hbar\omega_c \pm \frac{1}{2} g \mu_B B \tag{2.59}$$

where $\mu_B = e\hbar/2m_o$ is the Bohr magneton. The SdH oscillation peaks must match with the Fermi energy (ε_F), crossing with solutions of Equation 2.59. For values of *n* and *1/B*, when this happens, we have:

$$\frac{1}{B_{n+}} = \frac{1}{\varepsilon_F}\left[\left(n + \frac{1}{2}\right)\frac{\hbar e}{m^{cyc}} + \frac{1}{2} g \frac{e\hbar}{2m_o}\right] \tag{2.60}$$

$$\frac{1}{B_{n-}} = \frac{1}{\varepsilon_F}\left[\left(n + \frac{1}{2}\right)\frac{\hbar e}{m^{cyc}} - \frac{1}{2} g \frac{e\hbar}{2m_o}\right] \tag{2.61}$$

$$\frac{1}{B_{(n+1)+}} = \frac{1}{\varepsilon_F}\left\{\left[(n-1) + \frac{1}{2}\right]\frac{\hbar e}{m^{cyc}} + \frac{1}{2} g \frac{e\hbar}{2m_o}\right\} \tag{2.62}$$

From Equations 2.60, 2.61 and 2.62 we have:

$$\frac{1}{B_{n+}} - \frac{1}{B_{n-}} = \frac{1}{\varepsilon_F} g \frac{e\hbar}{2m_o} \tag{2.63}$$

$$\frac{1}{B_{n+}} - \frac{1}{B_{(n+1)+}} = \frac{1}{\varepsilon_F} \frac{\hbar e}{m^{cyc}} \tag{2.64}$$

Then, we obtain:

$$\frac{\left(\frac{1}{B}\right)_{n+} \left(\frac{1}{B}\right)_{n-}}{\left(\frac{1}{B}\right)_{n+} \left(\frac{1}{B}\right)_{(n+1)+}} = \frac{m^{cyc} g}{2m} \tag{2.65}$$

For sufficiently high magnetic fields, the Landau level spin splitting can be attributed directly, since the R_{xx} peaks begin to separate in two different peaks. The correct association of these peaks, with the spin up and down levels, is required. Figure 2.21 shows the association made by Burke *at al.* [75] for a *p*-type PbTe film.

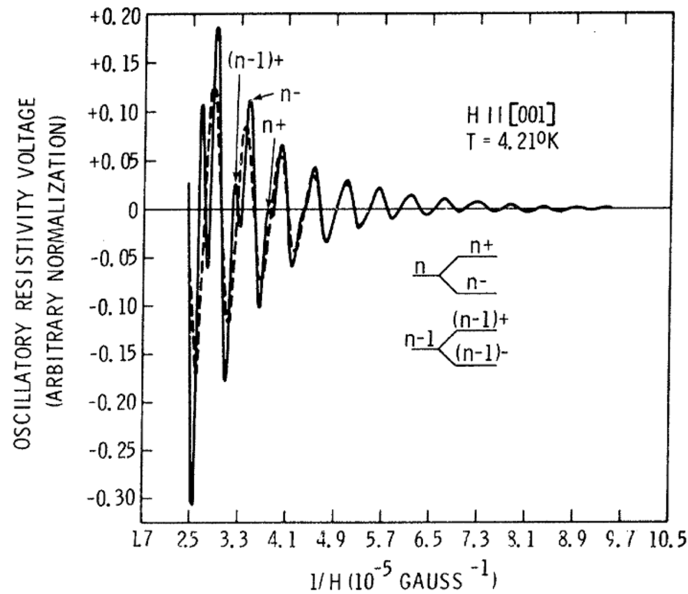

Figure 2. 21 Normalized oscillatory components of the resistivity versus *1/H* (*H* is the magnetic field). The doubling of the peaks is due to the Landau level spin splitting. Source: modified from [75]

The effects described in this chapter will support the analysis of experimental data presented in Chapter 4.

2.4.3. Linear Magnetoresistance

Another interesting and unusual MR is the appearance of a linear profile, rather than the classic behavior discussed in Section 2.4.1. This linear magnetoresistance (LMR) has attracted the scientific community attention due to the potential application in magnetosensor devices, that can be used in the development of recording heads, magnetic storage devices, magnetic position, speed sensors and magnetic levitating train [76] [77]. The LMR behavior was first reported by Kaptiza in 1928 [78], where he describes a device to create a pulsed magnetic field up to 32 T (huge advance for that period). The measurements were performed in a polycrystalline Bi sample which, to his surprise, presented a linear behavior for the whole B range. It was only in 1959 that Lifshitz and Perschanskii [79] developed a theory after publishing a series of articles on galvanomagnetic phenomena (GMP) in a strong magnetic field. They showed that in cases where the metal samples have open Fermi surfaces, the polycrystalline material would present LMR in magnetic field [79]. This LMR classic theory is called LP (Lifshitz and Perschanskii) theory. However, the Bi sample measured by Kaptiza does not have an open Fermi surface, so the LP theory is not applied, and the mystery remains.

Later, in 1969, Abrikosov [80] constructed a mathematical theory on GMP in metals, using Landau's quantization of the electron motion in a magnetic field (discussed in Section 2.3). In the Abrikosov's theory, he considers the extreme case, where all the electrons are only at the lowest Landau level, if the resistance varies linearly with the magnetic field. His theory has two conditions:

$$n \ll \left(\frac{eB}{\hbar}\right)^{3/2} \ and,\ T \ll \frac{e\hbar B}{m^{cyc}} \tag{2.66}$$

where m^{cyc} is the cyclotron effective mass. The first condition in Equation 2.66 requires the lowest Landau level to participate in the conduction mechanism and the second requires the temperature to be less than the band splitting. Both conditions are satisfied in the Kaptiza experiment. This is called Abrikosov quantum linear magnetoresistance (QLMR) theory, and states that the magnetic field and resistivity temperature dependence are given by:

$$\frac{\rho(B,T)-\rho(0,T)}{\rho(0,T)} = \frac{N_t B}{\pi n^2 e \rho(0,T)} \tag{2.67}$$

where $\rho(B,T)$ is the resistivity as a function of the temperature and the magnetic field, $\rho(0,T)$ is the resistivity value at B=0, N_t is the impurity density (defect center density) and n is the carrier density.

However, the samples investigated in this work are monocrystals, so these theories discussed above are not applicable. Nevertheless, in 1997, R. Xu *et al.* [81] published the LMR discovery in slightly non-stoichiometric silver chalcogenides sample, for B up to 5.5 T and for temperatures ranging from 4.5 to 300 K. Recent work shows that the linear profile persists for B up to 55 T [82]. At lower temperature, these materials are intrinsic semiconductors with a narrow direct gap. There is no way to explain this behavior in a homogenous material. Abrikosov [83] proposes two mechanisms to explain this discovery. First, real samples contain inhomogeneity, which can lead to small regions with high and small carrier concentration. In the lower concentration regions, the extreme quantum conditions for QLMR theory occur. Second, the disorder present in the sample causes the bands to overlap, transforming the narrow gap semiconductor into a gapless semiconductor with quasi-linear band structure [84]. Although there is no direct observation of this gapless state, it has been mathematically proven [80] and the QLMR theory has been applied successfully in recent works [29] [36] [85].

The effect discussed in this section can be used to experimentally obtain the impurity density according to Equation 2.66 and with this value it is possible to calculate the energy depth of the impurity levels within the band gap, according to Equation 2.9 from the PC effect.

3. Experimental setup

In this chapter, we describe the experimental set up used to perform the growth and measurements of samples investigated in this study. We present the MBE growth technique, which assures the high crystalline quality of samples. Also, the photoconductivity and magnetoresistance configurations are described in details.

3.1. Molecular beam epitaxy (MBE)

In this study, the samples were grown by Molecular Beam Epitaxy (MBE) which is a monocrystalline thin film deposition technique. This technique presents a very good cost/benefit relation, providing good crystalline quality samples and has high reproducibility. Furthermore, this technique ensures accurate atomic scale control of the deposition layers width and doping concentration [86].

The growing process in the MBE technique starts with the heating of solids sources, releasing a particle beam that reaches a hot substrate surface. Briefly, the growth process by the MBE technique consists of the vaporization, in general, of solid charge sources, by means of resistive heating. A molecular beam resulting from this action emanates from the sources directly to the heated surface of a substrate. This process occurs in an ultrahigh vacuum (UHV) chamber which ensures that the mean free paths of the vaporized species are much larger than the distances between sources and substrate. Furthermore, the epitaxial process occurs outside the thermodynamic equilibrium, since both the substrate and the source's temperature are different. In this way, it is possible to compensate for the differences between the sticking coefficient of the chemical compounds and the vapor pressure values of the deposited materials. In addition, it allows precise control of the thickness, composition and doping level of the epitaxial layers [87].

The samples investigated in this study were epitaxially grown in an MBE system, Riber 32P, located in the Sensor and Material Associated Laboratory (LABAS) of the National Institute for

Space Research (INPE). This equipment is exclusively dedicated to IV-VI and V-VI compounds [87].

Before starting the epitaxial layer growth, the substrate is chosen to meet the best possible adjustment of its parameters, that is, the lattice constant and coefficient of thermal expansion, with those of the layer. For example, for structures based on IV-VI compounds, barium fluoride, BaF_2, single-orientation volumetric crystal (111), is the best substrate choice. Therefore, in this work, synthetic monocrystals, produced by Korth Kristalle GmbH [88, 89], oriented and cut into regular prism shape and, as mentioned, with a cross-section in the plane (111) and a 15x15mm area, were used as a substrate. In the beginning, during the preparation process, thin BaF_2 slices, with a thickness of less than 1mm, are separated from the crystalline bar by cleavage. These freshly cleaved slices are, then, chosen by visual inspection, taking into account the better surface morphological appearance, i.e., wherever possible, with a reduced surface defect density, for example, low-angle tilt boundaries and restricted density of cleavage steps. Thereafter, these slices are attached, by the superficial tension of gallium-indium, Ga-In, liquid solution in a molybdenum holder and this assembly is then taken to the system loading chamber, Figure 3.1, label 1, where a schematic illustration is shown, from the top view, of MBE system, Riber 32P. As shown, this MBE system is composed of three chambers: in addition to the mentioned loading chamber, there is also a preparation chamber, Figure 3.1, label 2, and a main chamber or growth chamber, Figure 3.1, label 3, where the epitaxial process actually occurs. The preparation chamber is intended for substrate degassing and/or annealing process up to 700° C, under UHV condition created by ionic pumping. This chamber is isolated from the other chambers by manually operated UHV gate valves; the transfer of the sample holder between the chambers is done by magnetically coupled slide rods, Figure 3.1, labels, 1a and 2a. After the degassing, the substrate is taken into the growth chamber, Figure 3.1, label 3. In this location, the sample holder is coupled to a mechanical manipulator, Figure 3.2, which allows adjusting the angle between the molecular beam and the sample plane as well as rotating it around its axis. In addition, the substrate remains surrounded by a cryogenic panel built with a double hollow wall, which during growth is kept filled with liquid nitrogen to act as a cryogenic trap for the residual vapors. A second liquid nitrogen circuit involves the sources, shown in Figure 3.2, providing thermal insulation between them. Along with the cryogenic action, the UHV condition in this chamber is also aided by the simultaneous operation of two different types of pumping systems, ion vacuum pump and titanium (Ti) sublimation pump.

In the growth chamber, before the film deposition process, the substrate surface receives a thermal cleaning treatment at 300° C, for 10 minutes, and then the deposition procedure begins. [90].

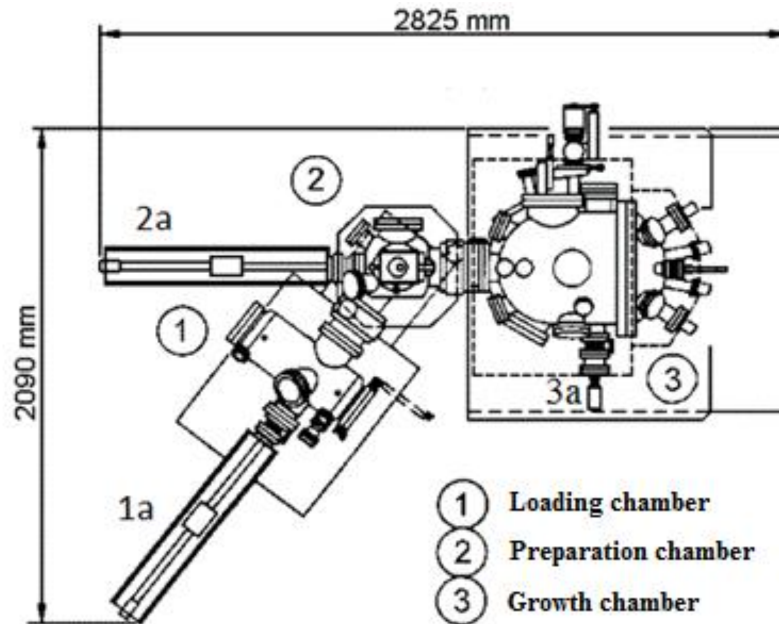

Figure 3.1 Top view schematic illustration of MBE, Riber 32P system, where the label (1) refers to the loading chamber, (2) to the preparation chamber and (3) to the growth chamber. Transfer of the sample holder between the chambers is carried out manually by means of magnetically coupled slide rods, labeled by (1a) and (2a); while (3a) shows the location of the RHEED electron gun. Source: modified from [91].

The Riber 32P MBE growth chamber has eight independent sources, each equipped with a mechanical shutter which interrupts the molecular beam, at up to 0.2 s intervals, accessed manually or remotely. In addition, there is also a central shutter that simultaneously blocks the gaseous flow from all sources. Substrate and source temperatures are set by computerized PID controllers and can be stabilized around the reference value with variations of ± 0.1° C [88]. In the manipulator, as mentioned, the sample holder can be rotated at angular velocities from 8 rpm, ensuring greater homogeneity and uniformity of the film. Vaporized flux calibration from the sources is performed through a nude Bayard-Alpert type hot cathode ionization vacuum gauge [92] which can be moved to the position previously occupied by the sample holder, Figure 3.2. This operation is simple, by construction; the manipulator allows to expose to the molecular beam or to protect from it, alternatively, either the substrate or the meter. Strictly speaking, these measurements refer to the

pressure variation in the meter, when it is exposed or not to the molecular beam. This property is due to the direct relationship between the two quantities: flux rate (number of molecules impinging on unit area per unit time) and pressure. For this reason, this measurement is sometimes called beam equivalent pressure (BEP).

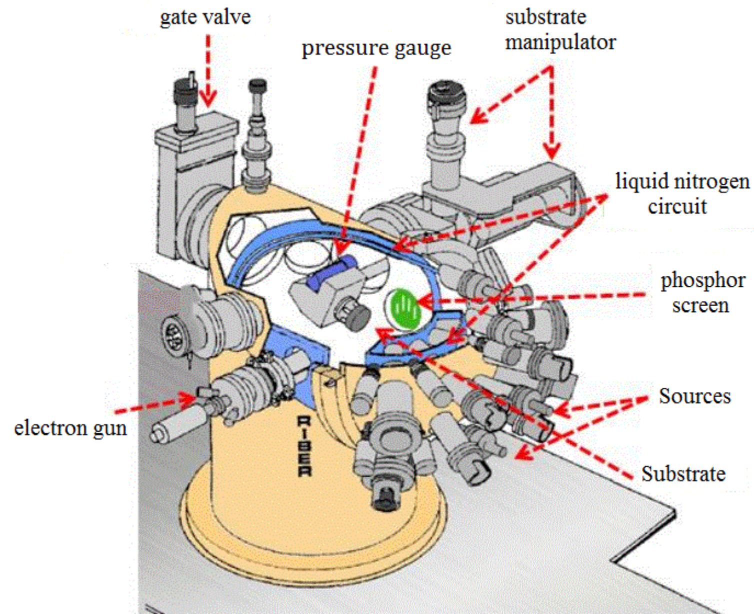

Figure 3.2 Schematic illustration of the MBE, Riber 32P, growing chamber, highlighting the sources, RHEED surface analysis technique (RHEED electron gun and fluorescent, phosphor coated, screen), cryogenic chambers and other parts, indicated by the red arrows. Source: modified from [87].

Due to the compatibility of the surface analysis technique by reflection high-energy electron diffraction (RHEED) with MBE, it has become useful to monitor *in situ* and real-time, thin film growth processes, as shown in Figure 3.2. In the RHEED technique brief description: an incident electron beam, generated by a hot filament cathode, referred to as an electron gun, is accelerated and collimated towards the sample surface through a system mounted by grids and multiple magnetic lenses. The energy of the electron beam typically ranges from 10 to 50 KeV, depending on the electron gun characteristics. At the sample surface, the beam is directed at small angles, below 5 °, so that its penetration occurs only in the outermost atomic layers, close to the surface, where it undergoes scattering. The diffracted beam, which emerges from the sample, is then reflected in the above-mentioned fluorescent screen, forming diffraction patterns. Due to the surface two-dimensionality, the reciprocal lattice degenerates into a column lattice, that is, the

points of the reciprocal lattice are transformed into a column lattice, parallel to each other in the normal direction of the surface which diffracts the beam, and the diffracted point patterns, reflected in the fluorescent screen, can be understood as the intersection of these columns with the surface of the Ewald sphere, determined by the wave vector of the incident electrons [93, 94]. By way of illustration, Figure 3.3 shows typical RHEED diffraction patterns related to the equivalent direction's family <110> based on the variation of the azimuth angle relative to the electron beam direction, along with the different steps of the epitaxial deposition process of compounds IV-VI on BaF_2 substrate. In particular, the images report some sequential steps of a 8 nm thick, *p*-PbTe single quantum well preparation, sandwiched between two $Pb_{0.9}Eu_{0.1}Te$ thick layers, with 2 μm, in this case, accommodated as barriers. However, the layer directly deposited on BaF_2 is also intended to serve as a buffer layer to reduce the difference between the PbTe and BaF_2 lattice parameters, $\Delta a = 4.1$ %, aware of the known similarity of the thermal expansion coefficient of the mentioned compounds. In the structural stacking order, Figure 3.3 (a) shows a typical diffraction pattern of a flat monocrystalline surface, whose crystalline quality is confirmed by the presence of Kikuchi lines, visualized in the image as tenuous diagonal lines. They originate from Bragg electron reflections, scattered inelastically, by the diffuse thermal effect of the incident beam on the crystalline planes, for example, due to the all atoms thermal vibration [95, 96]. Also, along the Kikuchi lines, two distinct points are observed: the one with the highest luminous intensity refers to the incident electron beam specular reflection diffraction, and the other, located higher up in the figure, refers to the diffraction by transmission, also referred to as a direct beam. Finally, the zero order Laue Zone [97], where the diffraction points are shown elongated, in the form of vertical, parallel stripes, with intensity and discontinuous thicknesses. The presence of these stripes, rather than well-defined diffraction points with intense brightness, typical in the pattern diffracted by flat monocrystalline surfaces with a high degree of perfection. When an electron beam with low dispersion in energy focuses on them, is based on the fact that the pristine surface of the BaF_2 slice, although flat, exhibit undesirable cleavage step sequences along the disruption plane, originating in the cleavage process, whose plane family <111> is linked to the octahedral shape. The image, shown in Figure 3.3 (b), records an immediate instant after the beginning of the $Pb_{0.9}Eu_{0,1}Te$ compound deposition, which occurs in a pseudomorphic growth regime, that is, the epitaxial layer is laterally tensioned by compressive force, seeking to align with the BaF_2 lattice, whose lattice parameter is smaller than that of the compound $Pb_{0.9}Eu_{0.1}Te$. In this case, the $Pb_{0.9}Eu_{0.1}Te$ lattice

parameter is larger than BaF_2 and, so, the distance between the stripes is closer. Because of that, in the reciprocal space the diffraction point spacing is inversely proportional to the distance in real space and, therefore, the diffraction pattern in Figure 3.3 (b), has a higher stripe density compared to the previous one. It is worth noting that the growth mode, at the beginning of $Pb_{0.9}Eu_{0.1}Te$ deposition on BaF_2 can be adjusted by varying the ratio Eu to Te_2 at the beam flow, according to the source temperatures. That is, at an early stage, growth can occur in islands, as discussed in the next section, and, therefore, a typical diffraction pattern, by transmission across the $Pb_{0.9}Eu_{0.1}Te$ islands, is displayed on the RHEED screen. However, as the deposition proceeds, with a few tens of nanometers, the islands coalesce, and the last dot pattern is gradually replaced by a typical flat surface pattern with some roughness, for example, as shown in Figure 3.3 (c). Otherwise, the layer-by-layer growth mode can be established from the beginning, as shown in Figure 3.3 (b). At the end of this step, the main shutter closes, blocking the vapor flow on the sample surface. As expected, after 3 h; 26 min of growth, with the deposition rate of 1.62 Å/s, we have an epitaxial film, with a thickness of 2 µm, relaxed of the strain induced at the $Pb_{0.9}Eu_{0,1}Te$/ BaF_2 interface, due to the elastic potential energy stored during the $Pb_{0.9}$ $Eu_{0,1}$ Te film thickening. This assertion is confirmed by the presence of finer and well-defined stripes, exhibited in the diffraction pattern in Figure 3.3 (c). However, this image quality degrades in the next step, Figure 3.3 (d), i.e. at the time of the main shutter reopening, for the *p*-PbTe quantum well deposition. In this case, in particular, the deposition occurred in the time of 1 min and 1 s which, with the growth rate of 0.131 nm / s, corresponds to the tensioned epitaxial film stacking, with 8 nm thickness. Therefore, by comparison with the previous diffraction pattern, the stripe thickening becomes evident. In addition to the degradation in the stripe definition, also the distance between them is a little bit bigger than in Figure 3.3 (c), although it is almost imperceptible because of the similarity between the heterojunction lattice parameters, as was intentionally thought. For the same reason, the beginning of the $Pb_{0.9}Eu_{0,1}Te$ barrier deposition on the, previously deposited, PbTe epitaxial film presents a diffraction pattern with stripes more intense and better defined, Fig. 3.3 (e), in relation to Figure 3.3 (b), when deposition occurred on BaF_2. As expected, the film surface epitaxial quality improves gradually with the barrier thickening, which, similar to the $Pb_{0.9}Eu_{0.1}Te$ intermediate layer, or buffer layer, after 3 h and 26 min, reached 2 µm and, thus, the sample structure growth was concluded. Finally, undoubtedly, the diffraction pattern, shown in Figure 3.3 (f), among those shown in the same figure, reports the best image quality due to the high epitaxial organization.

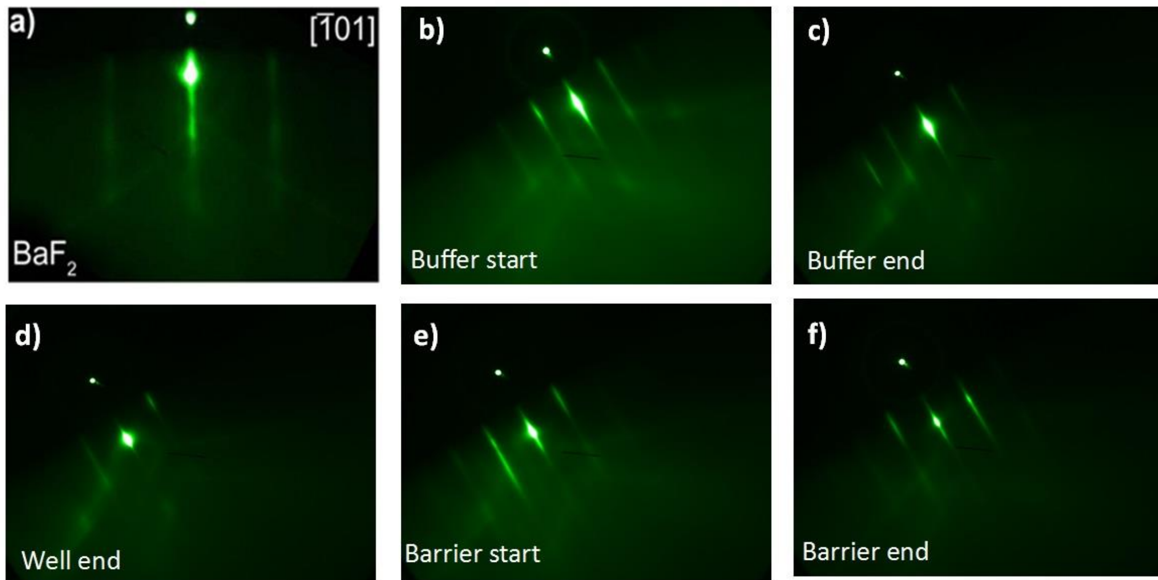

Figure 3.3. RHEED patterns related to the stacking sequence of a *p*-PbTe single quantum well structure grown between $Pb_{0.9}Eu_{0.1}Te$ layers, ID-(17041): (a) BaF_2 pristine surface, applied as a substrate, from reference [98] (b) $Pb_{0.9}Eu_{0.1}Te$ buffer layer at the growth beginning; (c) $Pb_{0.9}Eu_{0.1}Te$ buffer layer at the growth end; (d) *p*-PbTe single quantum well layer growth; (e) $Pb_{0.9}Eu_{0.1}Te$ barrier layer at the growth beginning; f) $Pb_{0.9}Eu_{0.1}Te$ barrier layer at the growth end.

In short, as mentioned, the epitaxial growth process by MBE occurs through the interaction of a gaseous phase in direct contact with the organized surface of a heated monocrystal, and then referred to as the substrate. This interaction involves physical-chemical mechanisms that may result in the adherence of the vaporized material molecules in different initial modes of deposition, as discussed in the next section.

3.1.1. Crystallization processes

During the epitaxial deposition, there are physical and chemical processes that can change significantly the properties of the grown film. Some of these mechanisms are shown in Figure 3.4 [86, 99]:

- Atom or molecule adsorption on the substrate surface;
- Atom or molecule thermal desorption that does not adhere to the film;
- Migration or dissociation of the adsorbed molecules;
- Atom incorporation into the crystalline lattice or to the growing film.

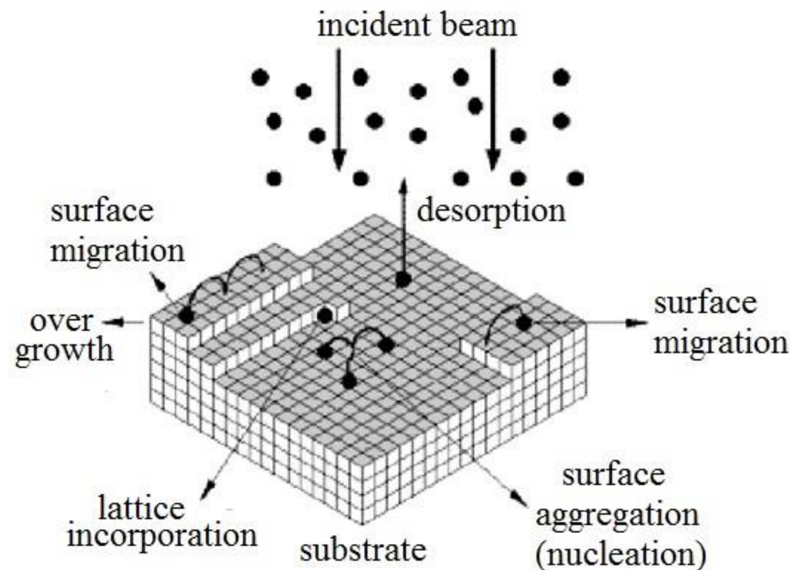

Figure 3.4. Schematic Illustration of some surface process that can occur during the epitaxial deposition. Source: modified from [99].

At the initial stage, vapor phase epitaxial deposition can present at least three distinct modes depend mainly on the lattice parameter difference of the materials involved and their surface free-energy [86, 100]. These deposition modes, in essence, are shown in Figure 3.5 and are distinguished, according to the epitaxial film surface morphological aspect, as two-dimensional

growth mode, case (a); three-dimensional, case (b); or an intermediate condition of these two modes, case (c):

I. Frank-van der Merwe mode, Figure 3.5(a), grows one layer after another, also known as a layer-by-layer mode; in this mode, the molecules integrated to the surface are more strongly bonded to the substrate than to each other. Therefore, the first molecules incorporated into the crystal lattice form a complete monolayer on the surface. This newly formed monolayer is, in turn, covered by another monolayer, and so on;

II. Volmer-Weber growth mode, Figure 3.5(b), small three-dimensional clusters, which become islands of aggregates, form on the substrate surface, or sample. These islands grow independent of each other until they coalesce and form a single layer with monolayer dozens. This occurs when the binding force between the molecules is stronger than between the vaporized material and the substrate The island volumetric aspect, whose height greatly exceeds the thickness of a monolayer, gives rise to the denomination of the mode of "island growth", or three-dimensional;

III. Stranski-Krastanov mode Figure 3.5(c), consists of the epitaxial film initially deposited in layer-by-layer mode and then in island mode. That is, this deposition mode stands out because it does not favor subsequent layer growth in the Frank-van der Merwe mode after elastic potential energy relaxation accommodated in the first stressed monolayers. In other words, even if the previously deposited layer is flat, the surface gradually becomes rough and deposition in island mode is established as the thickness increases. As mentioned, the spontaneous shift from the Frank-van der Merwe mode to Volmer-Weber mode is because of the high deformation degree existing between the epitaxial film and the substrate, caused by the difference between its lattice parameters.

It may be noticed that if the epitaxial growth occurs by any of the latter two modes, the surface will be rough with lower crystalline quality relative to the Frank-van der Merwe mode. However, it should be borne in mind that all growth modes are essential, each dedicated to the sample-specific preparation.

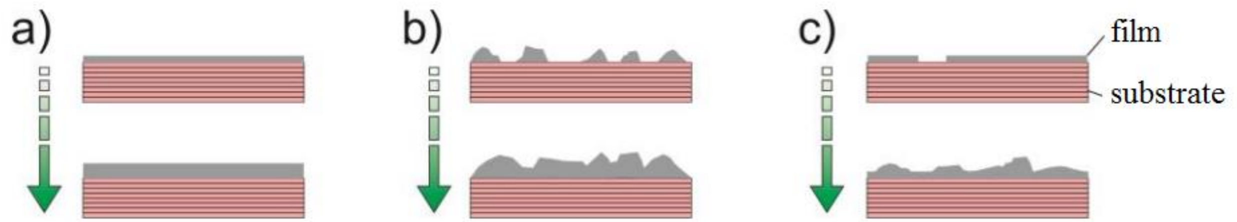

Figure 3.5. Different growth modes of epitaxial layers: (a) Frank-van der Merwe ;(b) Volmer-Weber growth and (c) Stranski-Krastanov. Source: modified from [87].

3.1.2. Sample growth data

As alluded to earlier, the sample epitaxial films were grown in MBE system, Riber 32P, on freshly cleaved BaF_2 (111) substrates, whose temperature was set at 240º C and no annealing periods were used. Initially, two n-PbTe/n-$Pb_{1-x}Eu_xTe$:Bi (0.06 – 0.08%) QWs, with PbTe well width ranging from 10 to 14 nm, were grown between symmetric doped $Pb_{1-x}Eu_xTe$:Bi layers, 30 nm thick, on $Pb_{1-x}Eu_xTe$ buffer layer, 2,4 and 2,7 µm thick, respectively, according to the schematic representation shown in Figure 3.6 (a). The PbTe/$Pb_{1-x}Eu_xTe$ system is particularly suited for the quantum well manufacture consisting of a narrow gap well combinations and wide gap barrier, since the $Pb_{1-x}Eu_xTe$ energy gap increases steeply with Eu content (x), which, in this case, ranges from 12 % to 10% for the 10 nm and 14 nm thick QW, respectively. Buffer and barriers were grown from the simultaneous sublimation of PbTe and Eu source, apart from Te offer and, consequently, x corresponds to the nominal film concentration, which, as mentioned (Section 3.1), is obtained by the material source beam equivalent pressure (BEP), $x = \frac{\mathrm{BEP(Eu)}}{\mathrm{BEP(Eu)+BEP(PbTe)}}$. Just to keep in mind, the BEP measurements were taken on a hot-cathode Bayard-Alpert nude gauge and the ion gauge is placed in the substrate position, just before starting the film deposition, returning to its place of origin after reading. $Pb_{0.9}Eu_{0.1}Te$ buffer, 2 µm thick, was deposited having the same x content and thickness as the barrier in the QW structure.

With respect to the PbTe electrical properties, they are usually dominated by nonstoichiometry, and the lattice defects, which can be used in a manner similar to the impurity addition. That is, Pb vacancy acts as acceptor (two holes) and Te vacancy behaves as a donor (two electrons), while the

Pb interstitial contributes one hole and the Te interstitial bears from neutral to weakly *n*-type. Therefore, doping can also be achieved by stoichiometry control, i.e. providing excess Pb or Te during growth, so it is impossible to produce undoped intrinsic PbTe. For this reason, *n*-PbTe layers are grown from nonstoichiometry PbTe charge, for example, in this case, rich in Pb to ensure the *n*-type character of the quantum well. Another QW series was prepared, but with *p*-PbTe well, that is *p*-PbTe/$Pb_{1-x}Eu_xTe$, where the $Pb_{1-x}Eu_xTe$ buffer layer and the barrier layer $Pb_{1-x}Eu_xTe$ were deposited with the same Eu content, $x = 10$ %, and thickness of 2 μm.

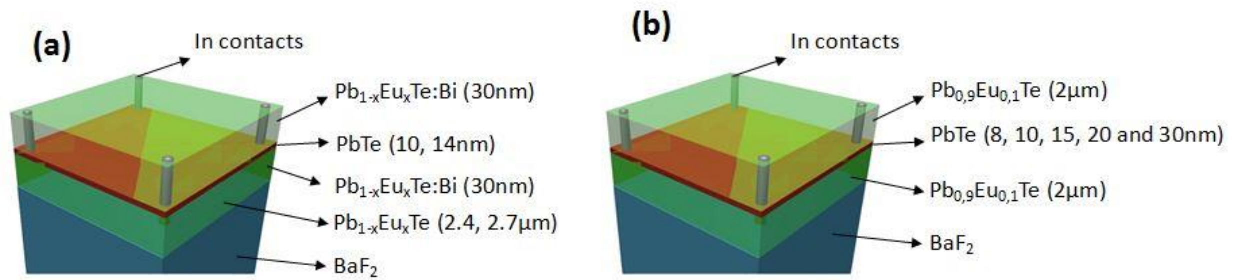

Figure 3.6 Schematic illustration of quantum well series structures: (a) *n*-PbTe/*n*-$Pb_{1-x}Eu_xTe$:Bi, with 10 and 14 nm well width, sandwiched between 30 nm barriers, seated on, 2.4-2.7 μm thick, buffer layer; (b) PbTe/$Pb_{0,9}Eu_{0,1}Te$, with 8, 10, 15, 20 and 30 nm well width, sandwiched between, 2 μm thick, $Pb_{0.9}Eu_{0.1}Te$, buffer and barrier, layers. The diffusion profile of the fused indium (In) contacts is also shown in the illustration

According to previous information, the PbTe source is filled with nonstoichiometric charge, but intentionally metal-rich, so that an additional flux of tellurium (Te_2) has always been simultaneously sublimated to obtain, in all QW structure layers, *p*-type intrinsic films. In each sample, the undoped *p*-PbTe QW layer thickness is not the same, but: 8, 10, 15, 20 and 30 nm, as schematically shown in Figure 3.6 (b). It should be said that the drastic deterioration effect on the $Pb_{1-x}Eu_xTe$ electronic transport properties with increasing Eu-content is used to minimize parallel conduction in the $Pb_{1-x}Eu_xTe$ layers: buffer and barrier.

The growth characteristics of *p*-type samples described above are present in Table 3.1 and Table 3.2. The table presents the beam equivalent pressure (BEP), the growth time of the barriers and the well and the estimated layer thickness.

Table 3.1 Some information on the *p*-PbTe/$Pb_{0.9}Eu_{0.1}Te$ QW epitaxial growth well width of 8, 10, 15, 20 and 30nm related to the beam equivalent pressure (BEP) measurements at the growth end, each layer growing time and the respective layer thickness

	p-PbTe/$Pb_{0.9}Eu_{0.1}Te$ QW structures							
Layer	Sample ID	well width (nm)	BEP (Torr), measurement after growing				Time (h:min:s)	estimated layer thickness
			PbTe	Te1	Te2	Eu		
Barrier "Buffer"	17041	8	$9.3x10^{-7}$	$7.7x10^{-8}$	$8.0x10^{-8}$	$1.2x10^{-7}$	03:26:00	2µm
	16022	10	$9.6x10^{-7}$	$6.7x10^{-8}$	$7.3x10^{-8}$	$1.2x10^{-7}$	03:26:00	
	17042	15	$9.3x10^{-7}$	$7.4x10^{-8}$	$7.8x10^{-8}$	$1.2x10^{-7}$	03:26:00	
	16024	20	$9.5x10^{-7}$	$6.2x10^{-8}$	$8.4x10^{-8}$	$1.1x10^{-7}$	03:26:00	
	16025	30	$9.5x10^{-7}$	$6.5x10^{-8}$	$8.6x10^{-8}$	$1.2x10^{-7}$	03:26:00	
Well	17041	8	$9.4x10^{-7}$	$3.0x10^{-8}$	$8.4x10^{-8}$	----------	00:01:01	8nm
	16022	10	$9.3x10^{-7}$	$5.0x10^{-8}$	$6.0x10^{-8}$	----------	00:01:18	10nm
	17042	15	$9.4x10^{-7}$	$3.1x10^{-8}$	$8.1x10^{-8}$	----------	00:01:54	15nm
	16024	20	$9.4x10^{-7}$	$4.4x10^{-8}$	$6.3x10^{-8}$	----------	00:02:35	20nm
	16025	30	$9.3x10^{-7}$	$5.1x10^{-8}$	$6.1x10^{-8}$	----------	00:03:53	30nm
Barrier "Cap"	17041	8	$9.2x10^{-7}$	$7.5x10^{-8}$	$7.8x10^{-8}$	$1.2x10^{-7}$	03:26:00	2µm
	16022	10	$9.7x10^{-7}$	$6.6x10^{-8}$	$7.4x10^{-8}$	$1.0x10^{-7}$	03:26:00	
	17042	15	$9.3x10^{-7}$	$7.4x10^{-8}$	$7.8x10^{-8}$	$1.1x10^{-7}$	03:26:00	
	16024	20	$9.7x10^{-7}$	$6.0x10^{-8}$	$8.5x10^{-8}$	$1.0x10^{-7}$	03:26:00	
	16025	30	$9.4x10^{-7}$	$6.2x10^{-8}$	$8.6x10^{-8}$	$1.1x10^{-7}$	03:26:00	

From the data presented in Table 3.1, we notice that the BEP values are quite constant which allows excellent control in the single quantum well structure manufacturing and, consequently, the epitaxial structure reproducibility in terms of layer thickness, Eu concentration in the $Pb_{1-x}Eu_xTe$ alloys and surface morphologies. Undoubtedly, they are indispensable prerequisites, but not sufficient, for this scientific research activity success.

3.2. Photoconductivity setup

Photoconductivity (PC) measurements were performed on 10 nm and 14 nm thick PbTe/$Pb_{1-x}Eu_xTe$:Bi QWs. To make the electrical contacts, small indium pellets are placed on the sample surface in the Van der Pauw geometry together with Au wires. This is set on a hot plate heated up to T=180 ºC. In this way, the indium diffuses through the heterostructure and crosses the layers (barriers and well), see Figure 3.5 [9]. Then, golden contacts connect the indium to the sample port. For the illumination of the sample, an infrared light emitting diode (LED) with a peak wavelength of 940 nm and ~12 mW/m^2 was used.

The PC measurements were performed in the "Laboratório de Caracterização Eletro-óptica de Materiais" at "Universidade Federal de Itajubá", under the supervision of Dr. D. A. W. Soares and at Sensor and Material Associated Laboratory (LABAS) at INPE. The system at "Universidade Federal de Itajubá" consists of a measuring source unit Keithley 237 as a current source. This equipment operates as a current source or voltage meter. The characteristic scales are ± 1.0000 nA with steps of 100 fA until 100.00 mA, supporting 10 μA. As voltage meter of $\pm 1.1000\ V$ with a resolution of 10 μV until $110.0\ V$ and 10 mV.

The measurements were made using 4 contact points and the LED were positioned right over the sample, to illuminate the surface homogeneously, Figure 3.7(a) shows an illustration of this setup. Then DC current from Keithley 237 is applied in two contacts while the tension is measured in the other two using a Keithley 2001, gathering an apparent electrical resistance value. The specifications of Keithley 2001 are: multimeter of 7 $^1/_2$ digits, 200 mV band, resolution of 10 μV until $200\ V$ and resolution of 10 mV.

The energy gap value $E_g(x,T)$ at T=77 K, is ~190 meV and ~727 meV for the well and the barrier, respectively, according to the expression $E_g(x,T) = 189.7 + 0.48[T^2/T + 29](1 - 7.56x) + 4480x$, where x is the Eu content in the alloy and T is the temperature [101]. The simplified illustration of the energy band diagram of this quantum well is shown in Figure 3.7(b), assuming 55:45 conduction to valence band offset [8], resulting in a potential barrier with height energy of 295 meV for the conduction band (ΔE_c) and 242 meV for the valence band (ΔE_v).

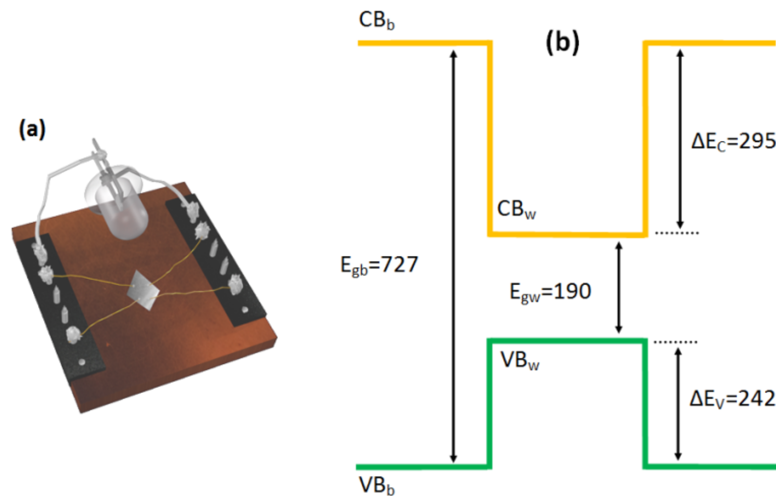

Figure 3.7 (a) Illustration of the sample port, with the indium and golden sample contacts, and the LED used for PC experiments. (b) A simplified illustration of the energy band diagram of these 10 nm and 14 nm $PbTe/Pb_{1-x}Eu_xTe$:Bi QWs assuming 55:45 conduction to valence band offset.

3.3. Magnetoresistance experimental setup

Preliminary magnetoresistance measurements on $PbTe/Pb_{0.9}Eu_{0.1}Te$ were performed at Physical Properties Measurements System (PPMS) from Quantum Design. This equipment permits magnetotransport measurements in a closed Helium circuit with an internal recovery system that allow almost total Helium recovery. The temperature can reach from 1.9 K until 400 K and a magnetic field up to 10 T. PPMS system is shown in Figure 3.8 where (a) is the enclosure superconductor magnetic, (b) and (c) are the human interface and the controller system. This automated closed system permits accurate measurements once it is equipped with a closed dedicated lock-in, lowering the noise signal and the human error. Also, it permits an excellent temperature and magnetic field control. However, it minimizes the students learning since the interaction with the assembly and operation of the equipment is minimal, once that it is an automated closed system.

Figure 3.8 PPMS equipment, (a) enclosed superconductor magnetic and the sample chamber, (b) and (c) Human interface and controller system.

Sample preparation in PPMS is similar to PC set, without the LED. Indium pallets were diffused in the sample in Van der Paul geometry and golden wires connect the sample to the sample port. Figure 3.9 shows the mounted samples at the sample port (a) with two available channels that permit measurement of the bottle at the same time. The set is in the user bridge (b) that allows testing the samples contact before inserted in the PPMS system.

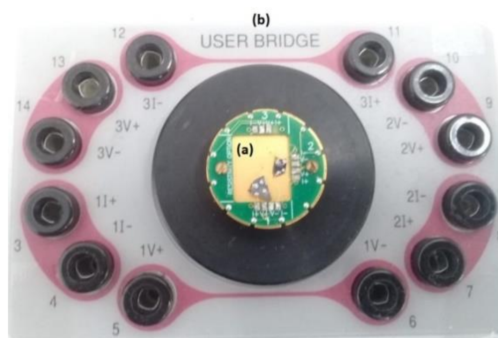

Figure 3. 9 (a) Sample port with two available channels with samples mounted and (b) the user bridge that allows the contact tests before inserting the set inside the PPMS system.

Low temperatures are crucial to decreasing thermal and phonon interferences permitting the observation of QHE and SdHO when the magnetic field is perpendicularly applied to the sample. The measurements performed using PPMS system, provided enough results to justify the internship at HFML – in the Netherlands, with lower temperatures and higher *B*, in order to better understand these effects.

3.4. Setup for Hall characterization

For the samples used to perform PC measurements (PbTe/$Pb_{1-x}Eu_x$Te:Bi QW), Hall characterization was performed at LABAS-INPE using a Keithley 80A system, assembled together with a Walker Scientific HV4 magnet up to 0.72 T. To make the electrical contacts, the same procedure from PC setup was followed. The contacts are made as illustrated in Figure 3.10. The Hall configuration requires transversal contacts, unlike Figure 3.7 that shows the configuration used for PC measurements. The Hall measurement system from INPE performs 8 measurements changing the configuration of the contacts at each round. For example, first, it applies current (*I*) in (1) and (3) and measures voltage (*V*) in (2) and (4), we can call it $I_{1,3}V_{2,4}$, than at $I_{2,4}V_{3,1}$ configuration until all possibilities are done. After that, the system takes the average over all values obtained at each configuration, leading to a more prudent value minimizing the problems generated by contacts geometry and edge effects.

Also, preliminary Hall characterization (discussed in section 4.2) was performed for PbTe/$Pb_{0.9}Eu_{0.1}$Te QW using PPMS device (presented in section 3.3) following the same configuration shown in Figure 3.10. Instead of average overall values obtained at each configuration, in PPMS was just took one measure of longitudinal resistance (R_{xy}) in the function of *B*, at fixed configuration. The carriers and mobility can be calculated in accord with Equations 2.44 and 2.47.

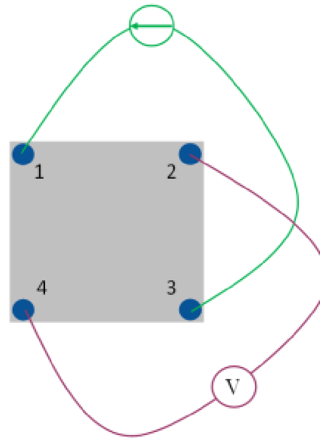

Figure 3.10 Schematic illustration of Hall configuration showing the transversal contacts. The current (*I*) is applying at contacts 1 and 3 while voltage (*V*) is measuring in 2 and 4.

However, at HFML, the laboratory structure is completely different from those discussed above. All equipment is mounted by the user according to the necessity. This setup is discussed in the next section.

3.5. Experiments performed at High Fields Magnetic Laboratory (HFML)

In order to investigate the electronic transport in PbTe/$Pb_{0.9}Eu_{0.1}Te$ QWs, magnetoresistance and Hall measurements were performed at HFML using a superconductor reaching magnetic field up to 15 T and a resistive magnetic with *B* up to 33 T. The resistive magnet (RM) illustrated in Figure 3.11(a), consist of a bitter coil composed by several single cooper plates discs stacked upon each other with insulator layers between them, as shown in Figure 3.11(b). Figure 3.11(c) shows the current applied in the copper plates that generate a magnetic field, also heating the plates which require a cool down with the water-based system. The cool water enters through the coil holes and hot water leaves the system. The probe with the sample is aligned in the center of the magnet, where *B* is maximum and equivalent in all directions, the data is captured by the mounted

equipment. The Bitter magnet used is located at cell 5 in HFML facility and the coils are powered by 17 MW power supply and a maximum current of I~36.7 KA.

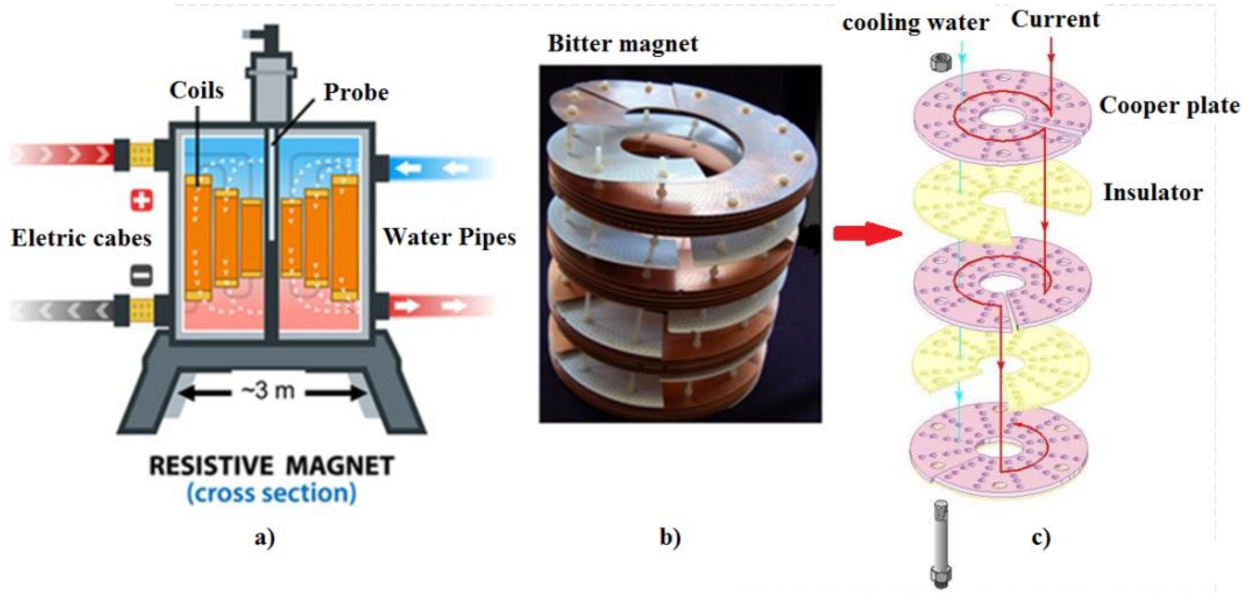

Figure 3.11 (a) schematic illustration of resistive magnet with the electric cable, water pipes, the probe and the coils. (b) Outer bitter coil, consisting of several singles plates discs stacked upon each other with isolation layer between them and (c) show the current flow through the coils (red line) heating the system that is cool down by demineralized water running through the holes (blue line). Source: modified from [102] and [103].

A He^3 cryostat was used to reach temperatures until 4.2 K and a He^4 close system to decrease temperature down to 0.35 K. To make the electrical contacts, small indium pellets are placed on the sample surface in the Van der Pauw geometry. This is set on an Annealing Oven AO 500 from MBE Components GmbH, heated up to 200 ^{o}C, at a closed chamber with argon gas evacuated until 10-40 mbarr pressure. In this way, the indium diffuses through the heterostructure and crosses the layers (barriers and well) [9]. After this process, Au wires with silver ink support are soldered over the diffused Indium pallets and then connected to the sample port.

Figure 3.12 (b), (c), (d) and (e) show the back and front side of the sample holder, the tip of the stick and schematic illustration, respectively. The sample holder accommodates until 4 samples at the same time, 3 in the front side (c) and 1 in the back side (b) and is coupled in the extremity of the stick, making possible to reach the center of the magnet. The stick (Figure 3.12(d) and (e)) is

equipped with a manual rotator allowing the user to change the angle between the sample and the *B* direction.

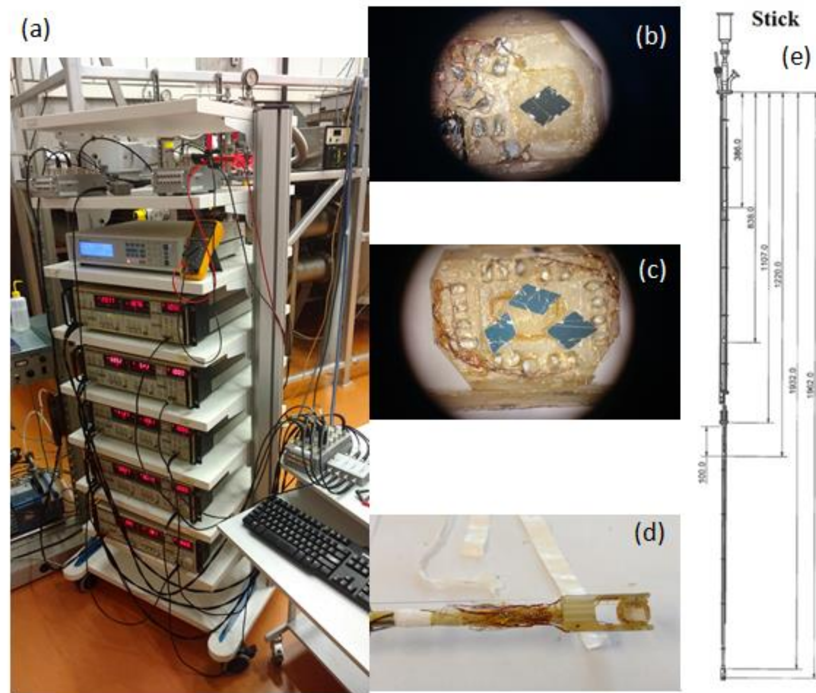

Figure 3.12 Pictures and illustration at HFML of (a) mounted current sources and temperature controller setup, (b) and (c) are the front and back side of the sample holder with samples, showing the available connections (d) the sticker point where the sample holder is attached allowing to reach the center of *B* in the bitter magnet and the rotator wire, (e) the entire sticker diagram.

In HFML all equipment is mounted by the user in accord with the necessity. Figure 3.12(a) shows the set mounted without the source for LED. We use one current source for each sample, a total of four, one more for the Hall probe and another for the LED. Also, a lakeshore temperature controller was used to stabilize the temperatures higher than 4.2 K. All equipment is connected to the sticker using co-axial cables by a connection box. The measurements performed using the superconductor magnet, follow the same procedures with *B* up to 15 T.

With all these arrangements above, it was possible to obtain crucial data in order to better understand the transport properties of the measured samples as presented and analyzed in the next chapter.

4. Results and analysis

In this chapter, the results of photoconductivity and magnetotransport measurements performed on PbTe QWs are presented. For the analysis, the theoretical models described in chapter 2 were used.

4.1. Photoconductivity results

In this section, we present photoconductivity measurements performed in a 10 nm and 14 nm PbTe/$Pb_{0.88}Eu_{0.12}$Te:Bi quantum well for temperatures from 300 K to 10 K using infrared light. The following results presented in this section were published in the Applied Physics Letter [104].

Figure 4.1(a) presents the normalized photoconductivity (σ/σ_0, where σ_0 is the electrical conductivity under dark conditions) measured for the 10nm PbTe/$Pb_{0,88}Eu_{0,12}$Te QW at temperatures ranging from 10 K up to 300 K using infrared illumination. An infrared light emitting diode with a peak wavelength of 940 nm and 12 mW/m^2 was used for the photoconductivity experiments. The illumination is switched on at t = 0 and off at t = 100 s. According to this figure, at high temperatures, the photoconductivity presents small amplitude ($< 1\%$) but, as temperature reduces, a huge increase of photoresponse is observed. At T=75 K, the maximum amplitude reaches a value 10 times higher than the original value before illumination. On the other hand, according to this figure, further decreasing the temperature leads to a photoconductivity amplitude reduction. The inset in Figure 4.1(a) details the photoconductivity amplitude temperature dependence (σ_M/σ_0), where σ_M is the maximum photoconductivity value. This behavior is unexpected since for most experiments in narrow gap semiconductors the photoconductivity amplitude increases as the temperatures decreases [11] [38] [58] [104]. This effect can be related to the QW structure, which may allow transport via a combination of two channels, in this case, the barrier and the well itself. As mentioned (Section 3.1.2), this is an unexpected scenario, because the $Pb_{(1-x)}Eu_{(x)}$Te electronic transport properties deteriorate with increasing Eu-content, x, minimizing the parallel

conduction in the buffer and barrier layers. However, the measurement results show that the bismuth addition alters the $Pb_{0.88}Eu_{0.12}Te$ barrier electrical insulator property. Therefore, the QW resistivity depends on the temperature region, as explained below.

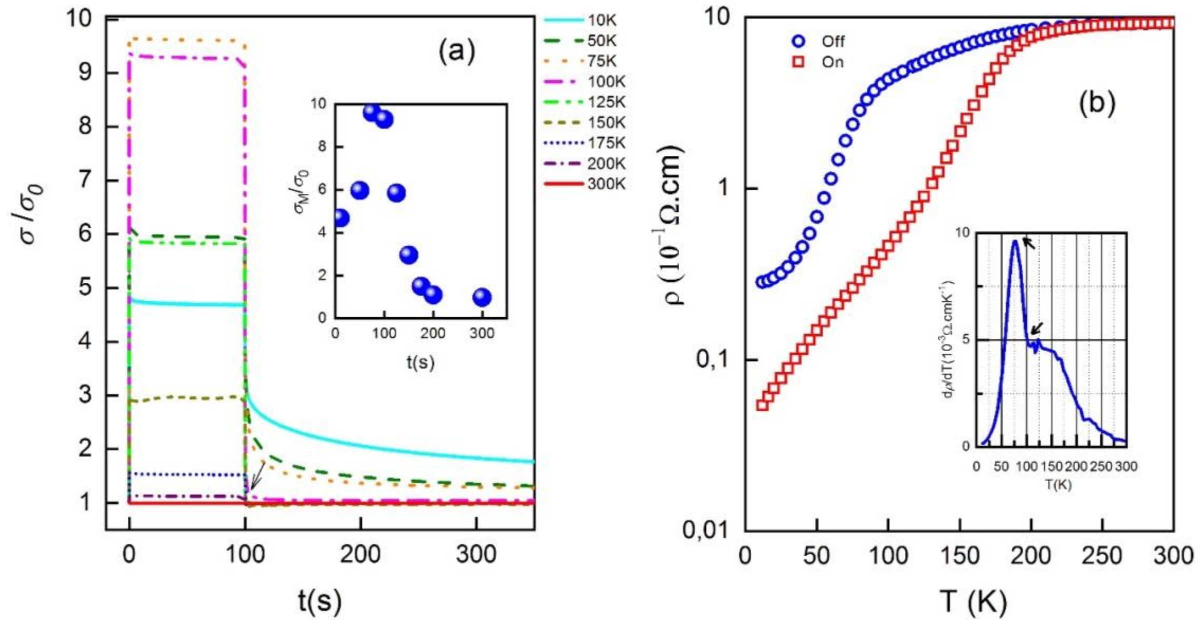

Figure 4.1 FIG. 2. (a) Normalized photoconduction of the $PbTe/Pb_{0.88}Eu_{0.12}Te$ QW structure under infrared irradiation (λ~940 nm) for temperatures ranging from 300 to 10 K. (b) Electrical resistivity as a function of temperature showing the conduction channel change from the barrier to the well, under dark (off) and illuminated (on) conditions. The inset displays the derivative of the resistivity concerning temperature without illumination.

Figure 4.1(b) presents the electrical resistivity ρ as a function of temperature under dark (off) and light (on) conditions. Without illumination (open circles), ρ decreases smoothly until 100 K and drops about one order of magnitude for lower temperatures down to 10 K. The insert in the figure shows the derivative of electrical resistivity with respect to temperature ($d\rho/dT$), where it is possible to observe a rapid increase below 100 K reaching a maximum value around 75 K and further decrease for lower temperatures. These curves suggest that an additional mechanism is effective in this temperature region, so that its contribution leads to the behavior observed in the electrical resistivity. Based on the measurement data, it is reasonable to assume that the transport, in the modulated structure, can be described by a combination of contributions from barriers and

the well, like in a parallel association of resistors, and, since each one responds differently to temperature variations, the association can explain, in a simple but satisfactory way, the profile observed in the resistivity. To verify this assumption, we measured the electrical resistivity as a function of the temperature of a 2 μm thick film similar (same composition and carrier density) to the constituent layers that compose the QW heterostructure: $Pb_{0,88}Eu_{0,12}Te$ (buffer), $Pb_{0,88}Eu_{0,12}Te$:Bi (barrier) and PbTe (well). The measurement data are show in Figure 4.2(b). From this figure, we verify that $Pb_{0,88}Eu_{0,12}Te$ buffer has practically no contribution to the total resistivity, since it is insulating, and the resulting resistivity is basically a combination of the conduction through the two 30 nm thick barriers and 10 nm thick well.

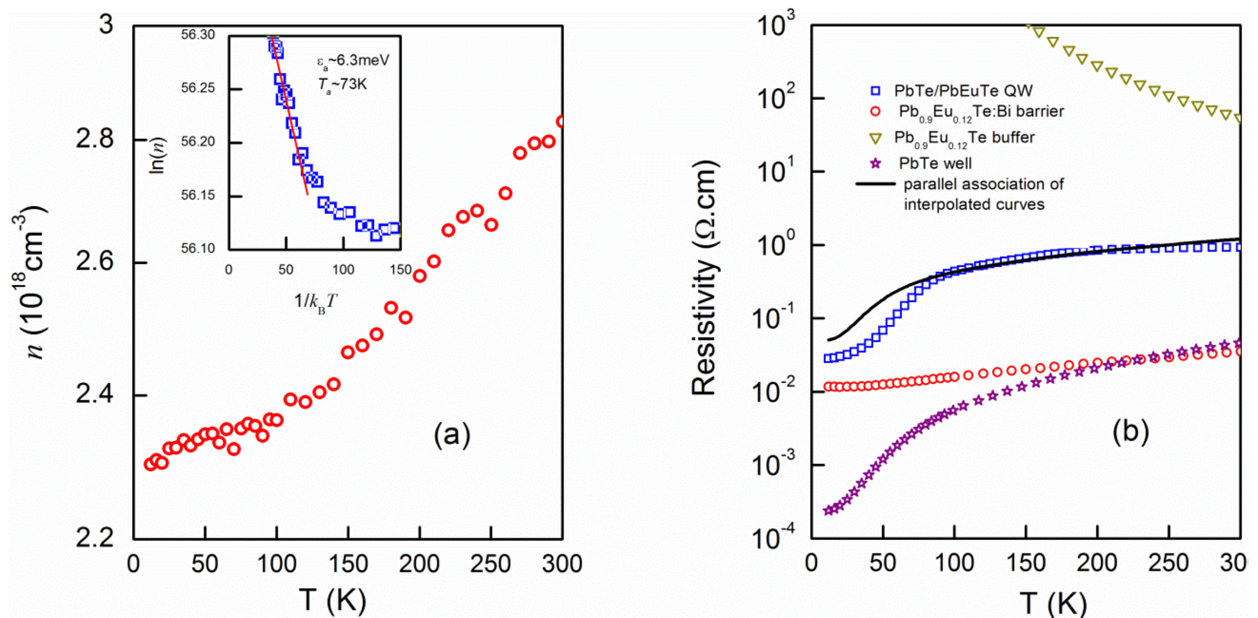

Figure 4.2 (a) Carrier concentration as a function of the temperature of $Pb_{0.88}Eu_{0.12}Te$:Bi single layer, where it is possible to determine activation energy that relates to a donor level located around 6.3 meV, below the conduction band edge. (b) Electrical resistivity as a function of the temperature of 2 μm thick film similar to the constituent layers that compose the QW heterostructure: $Pb_{0.88}Eu_{0.12}Te$ (buffer), $Pb_{0.88}Eu_{0.12}Te$:Bi (barrier) and PbTe (well), the same figure also shows the *n*-PbTe/$Pb_{0.88}Eu_{0.12}Te$ QW resistivity curve. The solid line represents resistivity of the parallel association of each layer considering the respective thickness in the structure.

To understand the conduction through the $Pb_{0,88}Eu_{0,12}Te$ doped with bismuth, we measured the carrier concentration as a function of the temperature of a 2.3 μm thick $Pb_{0,88}Eu_{0,12}Te$:Bi film, presented in

Figure 4.2 (a). We obtained an activation energy that relates to a donor level located around 6.3 ± 0.6 meV below conduction band edge, whose thermal energy, k_BT, correspond to 73 K. This value is very close to the temperature where the derivative of electrical resistivity with respect to temperature, presented in insert of Figure 4.1(b) for the 10 nm sample, is maximum. An analysis shows that at high temperatures (T>75 K, k_BT>6.3 meV), transport occurs through the barriers and well. On the other hand, for T<75 K (k_BT<6.3 meV), electrons are transferred from the donor state in $Pb_{0,88}Eu_{0.12}Te$:Bi barriers to the PbTe layer, in which case the transport is mainly through the well. The charge carrier transference from the barriers to well has already been reported in the literature for similar heterostructures based on PbTe compounds [23, 45].

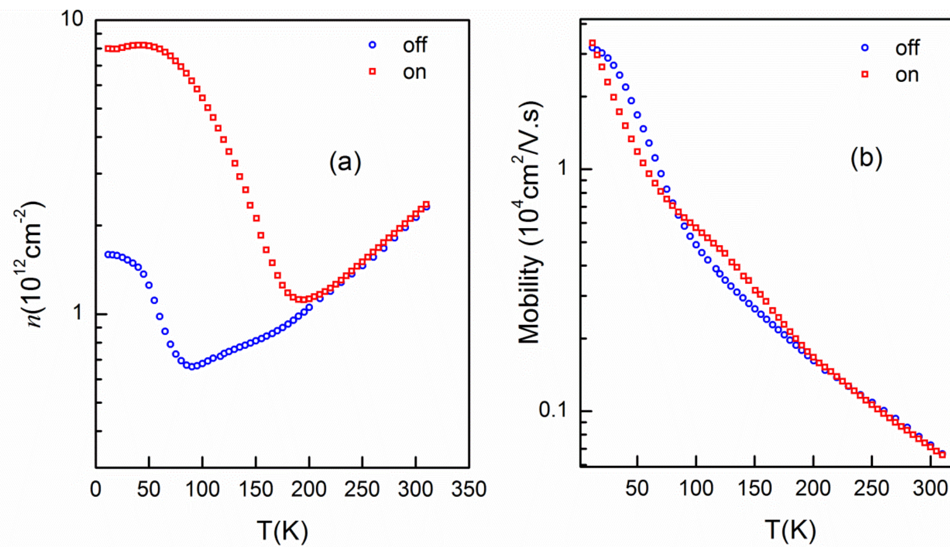

Figure 4.3 Electron density (a) and carrier mobility (b) of the 10nm n-PbTe/ $Pb_{0.88}Eu_{0.12}Te$:Bi QW structure, with 10 nm thick, measured as a function of temperature under the infrared light off and on.

Under illumination, red square symbol in Figure 4.1(b), the drop in resistivity occurs below 200 K for 10 nm QW, exhibiting a huge effect of light on transport properties. Infrared light (λ~940 nm) promotes carriers directly from the valence to conduction bands in the PbTe well and $Pb_{0,88}Eu_{0,12}Te$:Bi barriers. However, recombination rates depend on temperature. At temperatures above 200 K, recombination rates are high enough to reduce considerable the photoconduction effect. The Hall measurements performed on the QW structure, under dark and light conditions, corroborate very well with this result. As shown in Figure 4.3(a), an expressive increase in electron

concentration under illumination (red squares) is observed only below 200 K. For *T*>200 K, due to the high recombination rates, the photogenerated carriers practically do not contribute to the total electron density. In addition, the curve without illumination (blue circles symbol) in Figure 4.3(a) also exhibits an increase in carrier density for *T*<80 K, which is due to the carrier transfer from barriers to well, in accordance to the previous discussion.

Figure 4.3(b) presents the carrier mobility of the $PbTe/Pb_{0,88}Eu_{0.12}Te:Bi$ QW structure as a function of temperature. Without illumination (blue circles shape), mobility increases in the whole temperature range presenting a small saturation close to 10 K. Under illumination (red squares shape), the mobility curve is basically the same as that of dark conditions in the temperature range of 300 K to 200 K. In the region of 200 K to 80 K, it is possible to observe an increase of the mobility in relation to the curve without illumination and, for 10 K < T < 80 K, mobility under illumination becomes smaller than the curve under dark conditions. The decrease in carrier mobility indicates that the drop in the photoconductivity amplitude between 80 K and 10 K observed in Figure 4.1(a), is caused by an additional scattering mechanism, probably electron-electron interaction due to excess of photogenerated carriers. In addition, the scattering mechanism can be further enhanced by the contribution of multiple valleys in the QW [105]. This can be verified by calculating the Fermi level position in the QW at low temperatures, where the conduction in the QW structure occurs basically through the PbTe well. This can be derived taking into account the mass anisotropy and integrating the density of states for all possible subbands (one longitudinal and three oblique valleys) according to:

$$n = \int_0^{\varepsilon_F} d\varepsilon \frac{m_l}{\pi\hbar^2} + 3\int_0^{\varepsilon_F} d\varepsilon \frac{m_o}{\pi\hbar^2} \quad (4.1)$$

We found that:

$$\varepsilon_F = \frac{n\pi\hbar^2}{(m_l+3m_o)} \quad (4.2)$$

where m_l and m_o are the longitudinal and oblique effective masses, respectively [11]. At 10 K, the Fermi energy calculated for the PbTe QW under dark conditions, taking $n \approx 1.55 \times 10^{16}\ m^{-2}$, is $\varepsilon_F \approx 12.3$ meV. This indicates that only one longitudinal level (E_{L1}) is occupied at 10 K, according to Figure 4.4, where the confinement energy levels in the well conduction band, considering the longitudinal and oblique valleys, were obtained from Peres *et al.* [10] once the samples are similar.

The levels derived from the longitudinal valley correspond to 11 meV, 38 meV, 78 meV, 123 meV, 170 meV and, 219 meV, while the confined levels of the oblique valleys correspond to 45 meV and 154 meV, these values were extracted from reference [10].

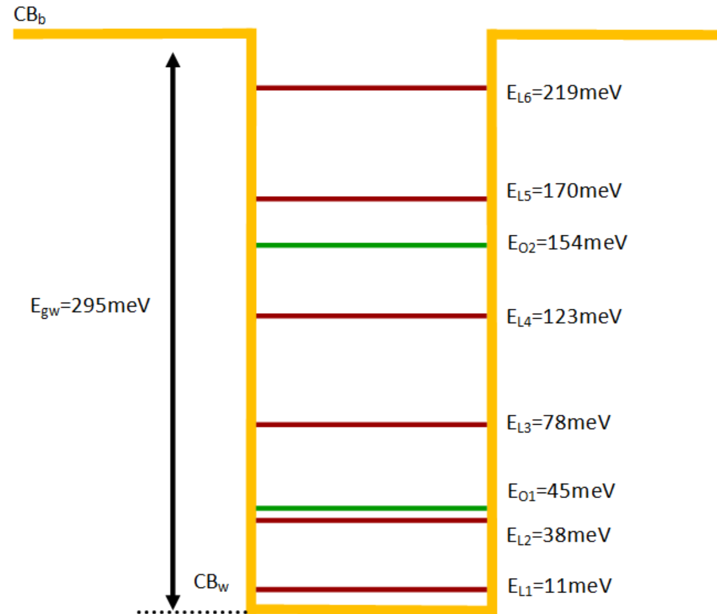

Figure 4.4 Simplified representative illustration of quantized energy levels within the 10 nm thick QW structure, derived from longitudinal (L) and oblique (O) valleys, using the effective mass approximation method from reference [10]. All energy values are in units of meV, where the upper level (CB_b) corresponds to the barrier conduction band energy, while (CB_w) corresponds to the well conduction band energy.

This means that, under dark conditions, a contribution from multiple valleys to scattering mechanism should not be observed. Under illumination, taking $n \approx 7.8 \times 10^{16}\ \mathrm{m}^{-2}$ at 10 K, we obtain $\varepsilon_F \approx 62.2\ \mathrm{meV}\ (\pm 4\ \mathrm{meV})$. In this situation, there are two longitudinal levels (E_{L1} and E_{L2}) and one oblique level (E_{O1}) occupied, as show in Figure 4.4. Thus, the longitudinal and the three oblique valleys contribute to transport under illumination at low temperatures. This effect leads to an enhancement of electron-electron scattering in this temperature range (10 K to 80 K), causing the reduction of carrier mobility and photoconductive amplitude as observed in Figure 4.3(b) and Figure 4.1(a), respectively.

The photoconductive effect in the $PbTe/Pb_{0,88}Eu_{0.12}Te$:Bi QW structure can be analyzed in more details. As the light is turned on, (t = 0 s in Figure 4.1(a)), the sample presented very fast

photoresponse and saturation with an almost noise-free signal. When light is switched off, however, the curve measured at 10 K exhibits strong persistent photoconductivity effect while curve at 150 K returns much faster to its original position, even though it also presents a persistent effect which is not visible in the graphic scale (see arrow in Figure 4.1(a)). The interplay between well and barrier in carrier transport has important consequences for the photoconductivity effect and trap levels within both channels are relevant to determine the persistent effect in the QW structure photoconductivity. Concerning the barrier, it is known that trap levels are present in films of $Pb_{1-x}Eu_xTe$ [36, 106]. Otherwise, information about trap levels in PbTe wells would not be available.

We can obtain information about the trap levels by analyzing the decay curves, when the light is switched off at t = 100 s in Figure 4.1(a), using the expression $\sigma(t) = \sigma_0 exp(-t/\tau)$ (Equation 2.7) [34], which describes the conductivity as a function of time. Figure 4.5 exhibits the natural logarithm of recombination times (τ), obtained from the exponential fitting to the decay curves, as a function of $1/k_BT$. As expected, the recombination time increases as temperature decreases. However, this behavior changes in the region where the transport starts to be dominated by the QW and, therefore, the recombination time reduces abruptly for temperatures below $\approx$75 K. It is possible to obtain the trap level energy, $\Delta\varepsilon$, responsible for the persistent effect on the barriers making a linear fitting to the curve in Figure 4.5, considering the expression [60] $\tau = \tau_0 e^{\Delta\varepsilon/k_BT}$ (Equation 2.8), the obtained value is $\Delta\varepsilon = 54\ meV (\pm 5$ meV). This trap level is originated from disorder which is present in the sample and comes mainly from Eu atoms addition [36]. We can consider the random inhomogeneity model, detailed in Chapter 2, and we obtain the energy associated with the trap level using the expression $E_t = e^2N^{2/3}/\varepsilon n^{1/3}$ (Equation 2.9), where N is the impurity density, n is the carrier concentration and ε is the dielectric constant. The impurity density N can be obtained from magnetoresistance (MR) measurements. It is known that one of the impurities presence effects in semiconductors is the linear magnetoresistance (LMR) effect [29] and that LMR must behave according to the expression $[\rho(B,T) - \rho(0,T)]/\rho(0,T) = N_iB/\pi n^2 e\rho(0,T)$ (Equation 2.89), where $\rho(B,T)$ is the electrical resistivity as a function of the magnetic field (B) and temperature (T). We performed Hall characterization (Figure 4.2 (a)) and MR measurements (inset of Figure 4.5) in a $Pb_{0,88}Eu_{0.12}Te$ film of 2.3 μm thickness in order to obtain the parameters necessary to determine N from the slope of magnetoresistance curve. The used values were $\rho \approx 6.25 \times 10^{-1}\ \Omega cm$, $n \approx 6.0 \times 10^{17}$ cm^{-3}and the slope of the MR curve is

$\approx 0.022\ \mathrm{T}^{-1}$, approximately (see inset in Figure 4.5). These values give $N \approx 2.5 \times 10^{19}\ \mathrm{cm}^{-3}$, which is a huge defect value when compared to N~$5\times10^{17}\ \mathrm{cm}^{-3}$ from Pirralho *et al.* [36]. This is expected since disorder in these films increases with Eu concentration. With these values we obtain $E_t \approx 30.5\ \mathrm{meV}\ (\pm 3\ \mathrm{meV})$ which differs from about 20 meV from the value obtained from the photoconductivity curves (≈54 meV). However, this difference can be a result of Bi doping of the barriers which should also introduce some disorder degree. In this case, the 54 meV value is an effective value, resulting from a disorder caused from Eu and Bi atoms.

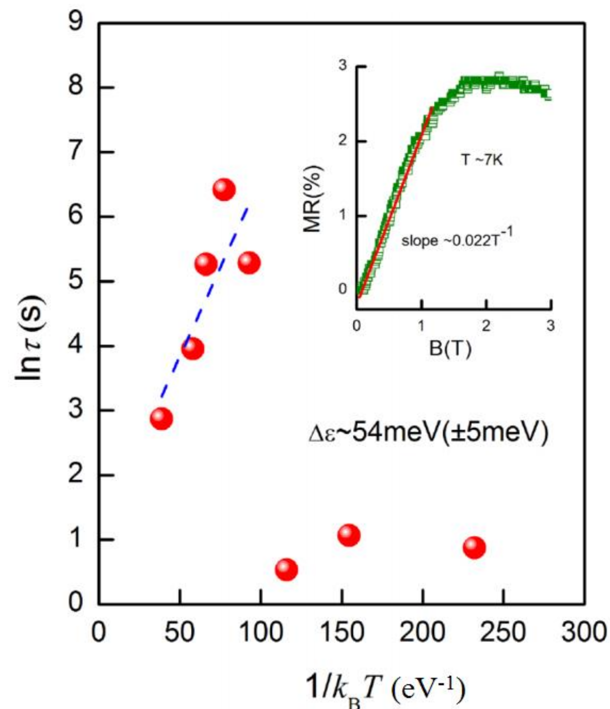

Figure 4.5 Natural logarithm of recombination time of PbTe/$Pb_{0.88}Eu_{0.12}Te$ QW structure, obtained room the exponential fitting to the decay curves in photoconduction, as a function of $1/k_BT$. The blue line corresponds to a linear fit for T>100 K, from which the activation energy relative to a trap level in $Pb_{0.88}Eu_{0.12}Te$ is determined. The inset shows the slope of the magnetoresistance curve for a $Pb_{0.88}Eu_{0.12}Te$ film with 2.3 µm of thickness.

In order to verify the reproducibility of the data presented so far, a similar sample, with 14nm thickness, *n*-type PbTe/$Pb_{0.9}Eu_{0.1}Te$ QW was grown and photoconductivity measurements were performed. The results are shown in Figure 4.6 (a) and (b), where we plot the maximum amplitude σ_m/σ_0 as a function of temperature. The photoconductivity profiles observed in Figure 4.6 (a) are the same as those observed in Figure 4.1 (a). In addition, in Figure 4.6 (b) we observe an increase

of σ_m/σ_0 as temperature decreases from 300 K down to 100 K, and a decreasing of σ_m/σ_0 for temperatures below 100 K. This observation is also in agreement with the profiles observed in Figure 4.1(b) for the QW with 10 nm thickness. It is important to point out that in this sample the maximum photoconductivity amplitude reaches a value about 1000 times higher than the value before illumination. This is probably due to the higher power density of the illumination since the LED was located much close to the sample in this case.

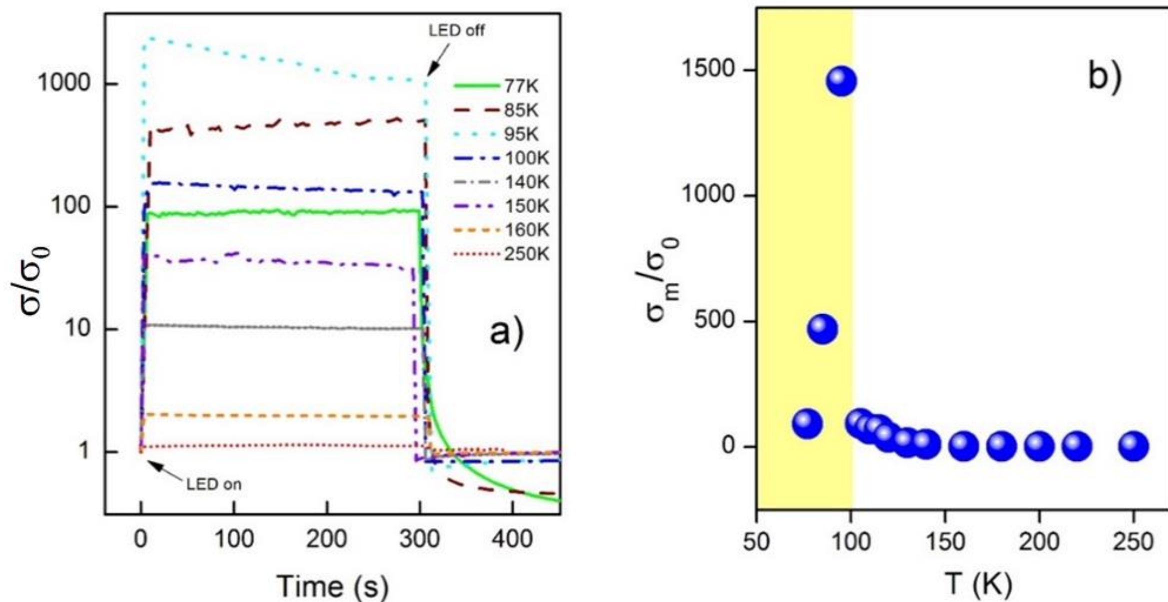

Figure 4.6 (a) Normalized photoconductivity when LED is turned on and off, for temperatures from 300 K to 77 K. (b) The normalized photoconductivity peak under infrared irradiation as a function of temperature between 300 K and 77 K.

This section presented the analysis of photoconductivity measurements and showed that multiple valleys contribution and disorder effect drastically change the transport properties on PbTe QWs leading to anomalous effects. Next section will present magnetotransport measurements in similar QWs that will take into account such effects.

4.2. Magnetotransport

This section presents the magnetoresistance and Hall effect measurements in *p*-type $PbTe/Pb_{0.9}Eu_{0.1}Te$ QWs samples with a thickness of 8, 10, 15, 20 and 30 nm well widths.

We first exhibit preliminary measurements performed on the 9 T magnet for temperatures varying from 1.9 K up to 300 K. For preliminary transport properties, the QWs with a thickness of 10, 20 and 30 nm were investigated. Figure 4.7 shows the behavior of electrical resistance normalized at T=300 K as a function of temperature for samples with 10, 20, and 30 nm QW thickness. The 10 nm well width showed metallic behavior for the whole temperature range measured, indicating that the two-dimensional electron gas (2DEG) is the main transport channel. Samples with 20 nm and 30 nm width wells presented insulator behavior for temperatures higher than ~180 K and ~200 K, respectively. However, between 50 K < T <220 K, specifically, for the 20 nm well width sample and between 40 K < T <180 K, for the 30 nm well-width sample, both present metallic behaviors. Also, the sample with 30 nm well width presented a transition from metallic to insulator behavior around 50 K while the sample with 20 nm well width reveals saturation bellow this temperature. In addition, the resistance profiles presented by those two samples indicate the transport via more than one channel at high temperatures.

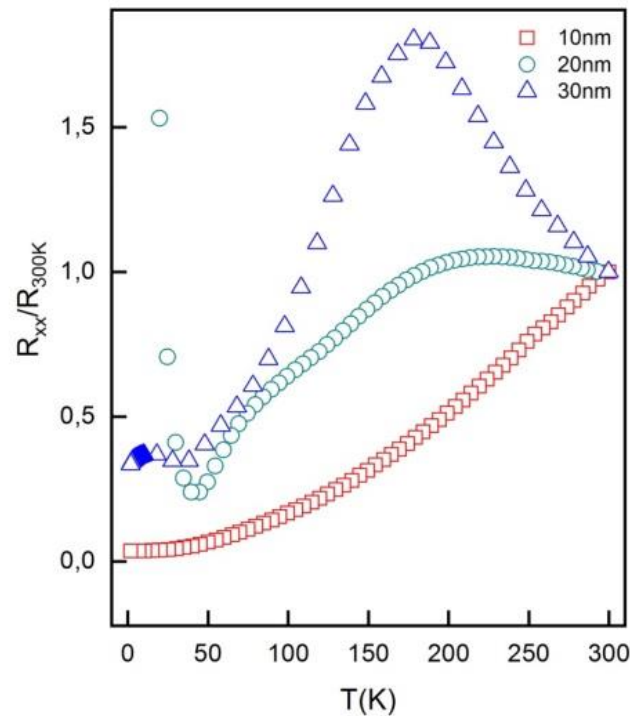

Figure 4. 7 Electrical resistance normalized in a relation to the value at 300 K, as a function of temperature for 10, 20 and 30 nm well width.

Figure 4.8(a) shows the longitudinal resistance (LR) profile for the 20 nm well width sample measured at 1.9 K. Only the classical behavior is observed, therefore no oscillations are present, indicating that quantum confinement is not effective for this sample under these conditions. Figure 4.8(b) presents the LR profile for the 30 nm well-width sample measured at 1.9 K. The profile exhibit classical behavior. For both samples, it is possible that the carrier mobility is not high enough to produce quantum oscillations in this magnetic field range.

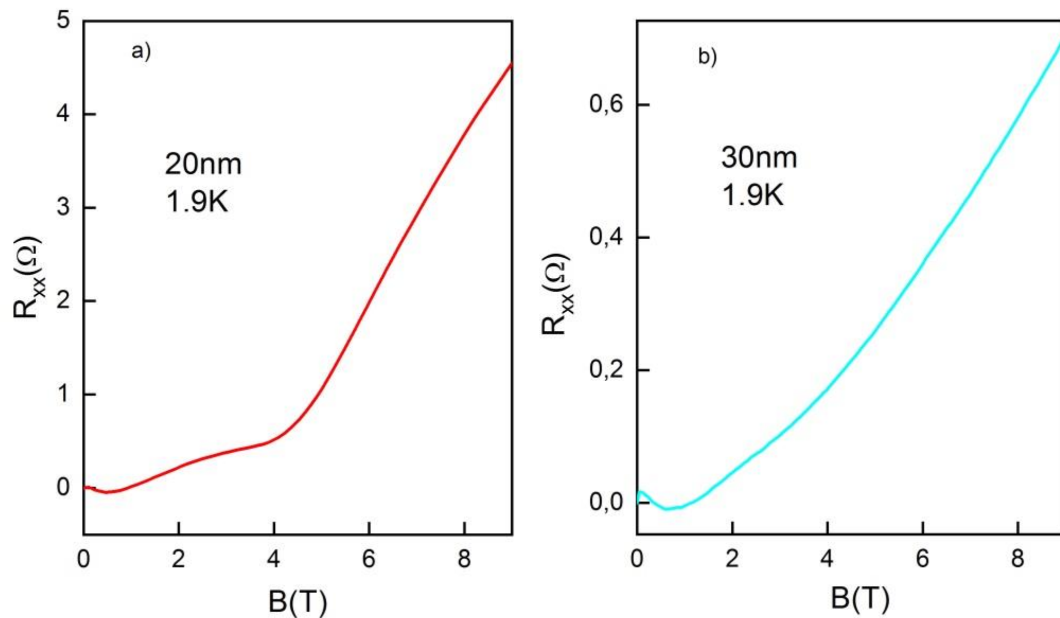

Figure 4.8. (a) *p*-PbTe 20 nm well width sample longitudinal resistance measured at 1.9 K. The profile shows only the classical behavior and no apparent oscillations, indicating that the quantum confinement effect is not effective for this sample under these conditions. (b)) *p*-PbTe 30 nm well width sample longitudinal resistance measured at 1.9 K. oscillations Unlike the previous sample, the measured profile exhibits neither classical behavior nor quantum oscillations.

Figure 4.9(a) exhibit LR for the 10 nm thick QW sample, measured in the 1.9 – 17 K temperature range. Unlike the previous samples, in this case, the oscillations are clear for magnetic field higher than 3.5 T ($B > 3.5$ T). The inset shows the reduced figure for B up to 7 T, showing that the oscillations are already present around 3.5 T. Figure 4.9(b) present the R_{xx} second derivative in relation to B showing more clearing the beating pattern. It is also clear that the oscillations diminish as temperature increase which agrees with the expected behavior, in accordance to Equation 2.52.

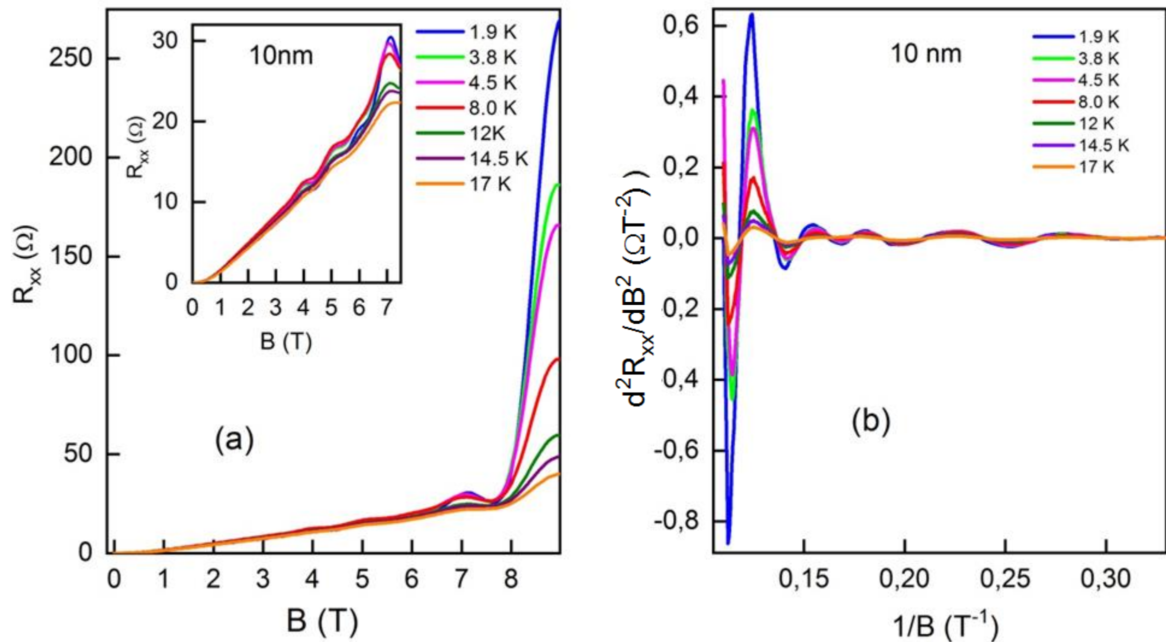

Figure 4.9. (a) LR measurements performed on the *p*-PbTe sample with 10nm well width, in the 1.9 K – 17 K temperature range, whose measure profile clearly shows oscillations for *B*>7T. The inset shows the measurement range reduced to *B* up to 7 T. (b) R_{xx} second derivative in relation to *1/B* which shows more clearly the beat pattern.

As discussed in section 2.4.3, it is possible to obtain the oscillations fundamental frequencies from the filling factors (ν) linear behavior in accordance to Equation 2.58: Figure 4.10(b) exhibit the Landau fan chart diagram, for a 1.9 K temperature, where odd and even filling factors values are associated to the d^2R_{xx}/dB^2 curve maximum and minimum points with the respective *1/B* values, the data are extracted from Figure 4.9(b). From the slope, we obtain the main frequencies F_1 = 18 T (±1 T) and F_2 = 35 T (±1 T). The F_2 value is approximately the double of F_1 (F_2=2 F_1), which means that F_2 is the F_1 second harmonic. These frequencies are proportional to the Fermi surface by Onsager relation, expressed in Equation 2.57, and are related to the 2D carrier concentration according to Equations 2.56. From this we obtain $p_1 = 4.35 \times 10^{15}\ \mathrm{m}^{-2}$ $(\pm 0.48 \times 10^{15}\ \mathrm{m}^{-2})$ and $p_2 = 8.45 \times 10^{15}\ \mathrm{m}^{-2}(\pm 0.48 \times 10^{15}\ \mathrm{m}^{-2})$ for F_1 and F_2, respectively. The sum of these values leads to a total carrier concentration of $p_1 + p_2 = 1.28 \times 10^{16}\ \mathrm{m}^{-2}$, that differ from $7.20 \times 10^{15}\ \mathrm{m}^{-2}$ when compared with the $p_{Hall} = 2.00 \times 10^{16}\ \mathrm{m}^{-2}$ obtained from the Hall effect measurements. This difference may originate from a different conduction mechanism. For further investigation we perform a Fast Fourier Transform (FFT) analyses on Figure 4.9(b) curves, the result are shown in Figure 4.10(a) for 1.9 – 17 K temperatures and 3 - 9 T magnetic field range,

respectively. The more prominent frequencies peaks are 18 T (±1 T) and 35 T (±1 T), same as F_1 and F_2 calculated from the Landau fan chart diagram of Figure 4.10(b). From this analysis, two other frequency peaks are found which values are, F_3 = 30 T and F_4 = 41 T. These frequencies peaks are surging aside from the F_2, one lower (F_3) and one higher (F_4) and may be due to the Fermi surface splitting caused by Rashba effect [10, 68]. Furthermore, from the frequency peak dumping, as show in Figure 4.10(c) for the F_1 peak, it is possible to calculate the carrier cyclotron effective mass from the amplitude hyperbolic sine behavior as a function of the temperature in accord with the Equation 2.52. The calculated mass for F_1 peak is $m_{cyc}^{F_1} = 0.061 m_e$. However, further analysis and investigations at high magnetic fields are necessary to correctly address which effect is occurring, once that the peaks are interfering between with other. This analysis is shown next.

According to Figures 4.8, 4.9 and 4.10, the 10 nm well width sample seems more promising to be investigated at higher magnetic fields and lower temperature, where additional features could be evidenced. In fact, all samples were measured at higher fields and lower temperatures, including the 8 and 15 nm well width ones. However, the SdHO and the QHE are only present in the 10, 15 and 20 nm thicknesses QW. The higher magnetic fields measurements data are showed as follow for the 10, 15 and 20, 8 and 30 nm well widths, respectively.

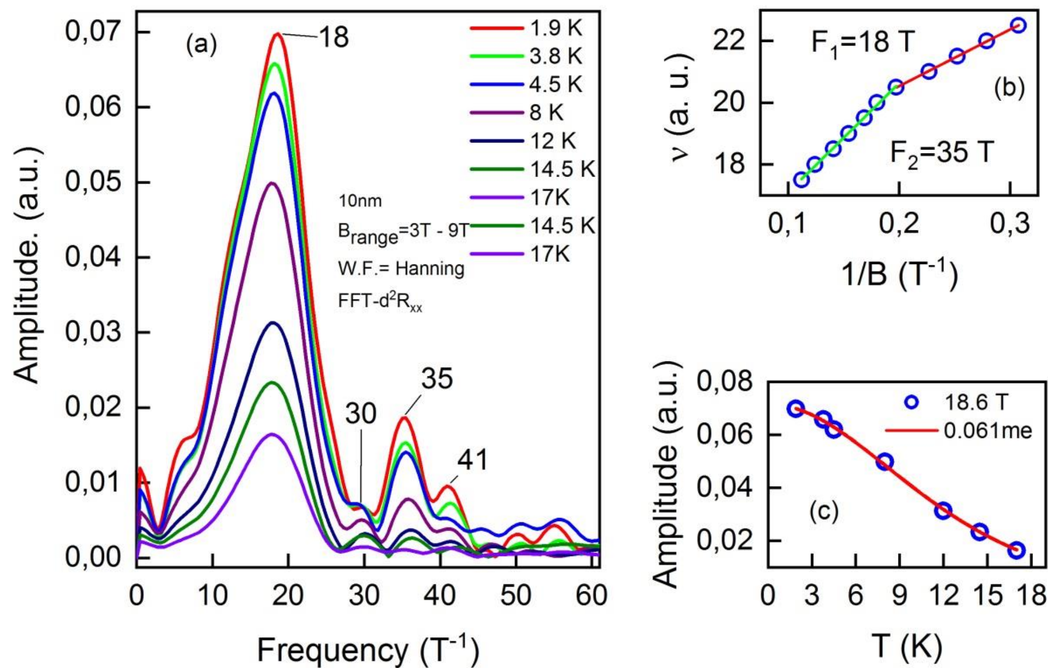

Figure 4. 10. (a) Fast Fourier Transform (FFT) on a 10 nm width well *p*-PbTe sample performed on the $d^2R_{xx}/d(1/B)^2$ curves for the 10nm width QW, show in Figure 4.9(b), for 1.9 – 17 K temperatures, using Hanning windows function and for 3 -9 T magnetic field range. (b) Landau fan diagram for the temperature of T = 1.9 K, where odd and even filling factors values are associated to the $d^2R_{xx}/d(1/B)^2$ curve maximum and minimum points with the respective *1/B* values. The linear fitting provides the fundamental frequencies associated with the SdHO. (c) FFT amplitude for the 18.6 T peak as a function of temperature and the hyperbolic sine fitting, in accord with the Equation 2.48, providing an effective cyclotron mass value of $0.061m_e$.

For the 10nm well width, the electrical longitudinal resistance (LR) R_{xx} (solid curve) and the Hall resistances R_{xy} (dotted blue curve) are shown in Figure 4.11(a). Measurements are performed for magnetic fields up to 33 T and for the temperature of 0.35 K. R_{xy} exhibit very clear plateaus, indicating the Landau level quantization. The SdH oscillations are also presented in R_{xx} curve. In 15 T, a flat plateau in R_{xy} and the near zero resistance in R_{xx} are well defined. These profiles indicate high sample quality and the 2DEG electronic quantum confinement in the QW. The non-zero plateaus in R_{xx} indicate that the conduction is occurring through more than one channel. In section 4.1, this extra channel was associated with the parallel conduction due to the remaining contribution of the PbEuTe layer as already reported in the literature [23, 104]. However, for this samples, the Eu content in the barriers is x=10%, which guarantee an insulator profile once the MIT occurs at x=6% as discussed in Section 2.1.2 from the data presented in Figure 2.3.

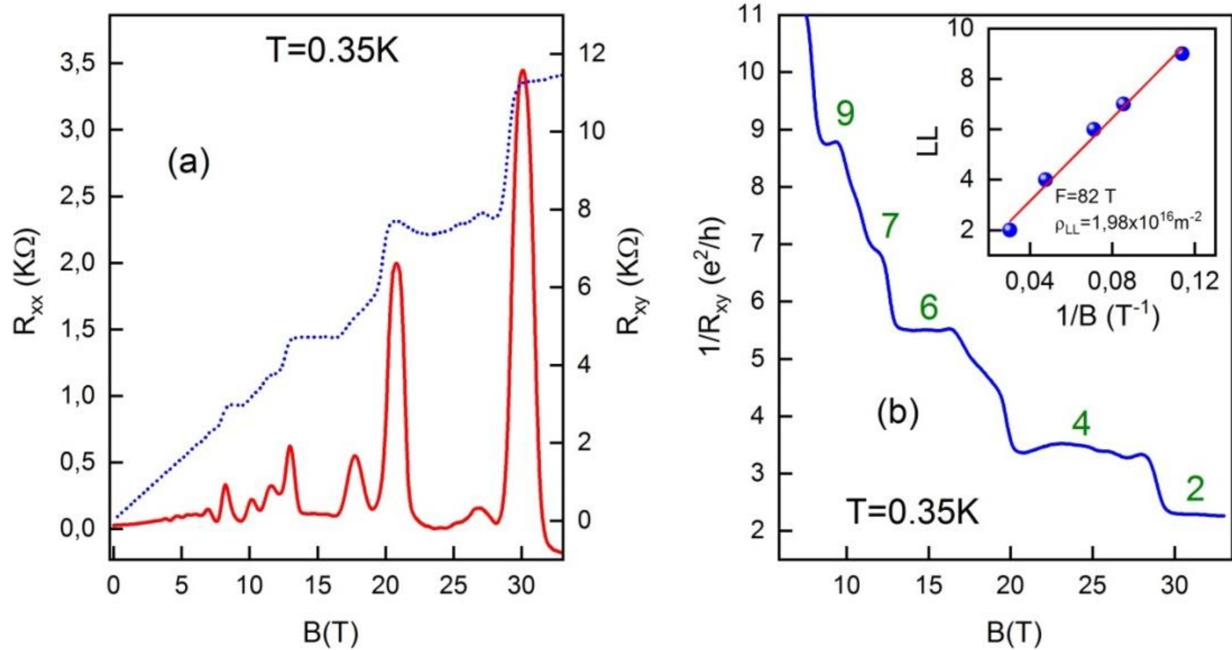

Figure 4.11 (a) R_{xx} and R_{xy} for T=0.35 K. (b) $1/R_{xy}$ in units of e^2/h and the inset is the Landau fan diagram.

The filling factors can be obtained directly by plotting the inverse of the Hall resistance in units of (e^2/h) as a function of B, as shown in Figure 4.11(b), and the obtained values are 2.3; 3.4; 5.6; 6.9 and 8.8. According to the literature [11, 23], these fractional filling factors values are not expected since the R_{xy} curve exhibit flat plateaus. These can be originated from remaining parallel conduction through the barriers of PbEuTe [23] or from the edge states [107-109]. Therefore, for this analysis, we consider the approximated values: 2; 4; 6; 7 and 9 calculated according to Equation 2.40, using the experimental B values corresponding to the observable R_{xy} plateaus. We plot these filling factors as a function of $(1/B)$ where the R_{xx} minima occur (B ~ 8.7 T; 11.7 T; 14 T; 21 T and 33 T). The expected linear dependence is observed as shown in the inset of Figure 4.11(b). From Equation 2.54 ($\upsilon \propto F/B$, where υ is the filling factor), we obtain the fundamental frequency (F) of the SdH oscillations [110, 111]. The obtained value is F = 82 T (±5 T) and from this frequency, it is possible to obtain the 2D carrier concentration, according to Equations 2.56 and 2.57, $p_{2D} = k_F^2/4\pi$ and $k_F^2 = Fe/\pi h$, where k_F is the Fermi wave vector, h is the Planck constant and e the electron charge. The carrier concentration calculated from the Landau fan diagram frequency is $p_{LL} = p_{2D} = 1.98 \times 10^{16}\ \mathrm{m^{-2}}$ $(\pm 0.24 \times 10^{16}\ \mathrm{m^{-2}})$, which is in good agreement with the value

obtained from Hall effect measurements $p_{Hall} = 1.97 \times 10^{16}$ m^{-2}($\pm 0.29 \times 10^{16}$ m^{-2}) at T~0.35 K.

A detailed analysis of the filling factor values can be derived from the equations that calculate the energy levels in the QW, which should include the PbTe Fermi surface multivalley character. The PbTe first Brillouin zone is composed of four-revolution ellipsoids in k-space: one longitudinal (l), parallel to the growth direction, <111>, and three other oblique (o) equivalents, tilted at $\phi = 70.53^{o}$ with the reference axis, as shown in Figure 4.12. This constitutes the multivalley structure of PbTe with is longitudinal and oblique valleys. Due to the strong mass anisotropy $(m_{\parallel}/m_{\perp} \approx 10)$, the valleys splitting causes large confinement energy difference between the longitudinal and the threefold-degenerated ones [75, 112]. The odd filling factor sequence can originate in these multi–valley channels, if oblique and longitudinal valleys participate in the charge transport process [11, 23]. In order to determine the quantum confinement energies, we use the envelope function model, developed for lead-salt QWs, using the Ben Daniel-Duke like boundary conditions, considering the even and odd solutions [113]:

$$\frac{\chi}{m_b(E)} = \frac{q}{m_w(E)} \tan\left(\frac{qL}{2}\right) \tag{4.1}$$

$$\frac{\chi}{m_b(E)} = -\frac{q}{m_{w(E)}} \cot\left(\frac{qL}{2}\right) \tag{4.2}$$

where,

$$\chi = \pm\sqrt{\left(2m_b(E) * (\Delta E - E)\right)/\hbar^2} \tag{4.3}$$

and

$$q = \pm\sqrt{(2m_w(E)E)/\hbar^2} \tag{4.4}$$

where χ and q are the plane wave vectors for the well and barriers, respectively, L=10 nm is well width, ΔE is the energy barrier height, taking into account the 55:45 band offset parameter between the conduction and valence bands [8]. $m_w(E)$ and $m_b(E)$ are the effective masses for the well (w) and the barriers (b), respectively. For the longitudinal valley the effective masses are:

$$m_{l;w}(E) = m_{l;w}^{cyc}(E) = m_{\parallel;w}(E) \tag{4.5}$$

$$m_{l;b}(E) = m_{l;b}^{cyc}(E) = m_{\parallel;b}(E) \tag{4.6}$$

and for the transverse valleys:

$$m_{t;w}(E) = m_{t;w}^{cyc}(E) = \frac{1}{3} m_{\perp;w}(E)\left(1 + \frac{8m_{\parallel,w}(E)}{m_{\perp;w}(E)}\right)^{1/2} \tag{4.7}$$

$$m_{t;b}(E) = m_{t;b}^{cyc}(E) = \frac{9m_{\parallel,b}(E)m_{\perp;b}(E)}{8m_{\parallel,b}(E)+m_{\perp;b}(E)} \tag{4.8}$$

where $m_{l;t;w}^{cyc}(E)$ is the cyclotron mass for longitudinal and transverse valleys, given by the projection of masses ellipsoids on *x-y* plane presented in Figure 4.12 as m_l and m_t, respectively.

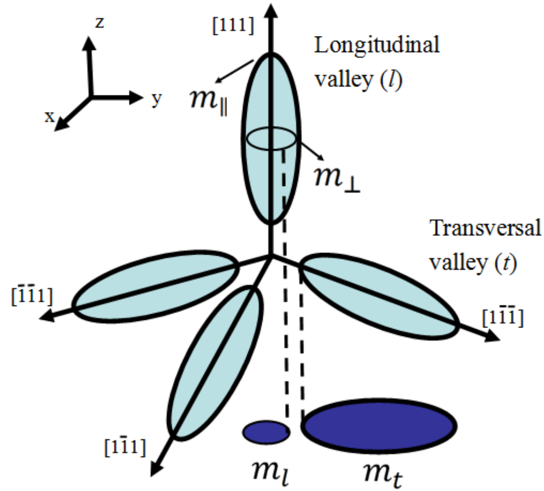

Figure 4. 12 Schematic illustrations of the four <111>-oriented revolution ellipsoids of PbTe Fermi surface, showing the parallel $(m_{\parallel})$ and the oblique $(m_{\perp})$ mass and their projection (m_l and m_t) into the *x-y* plane.

In this work, we chose a more complex approach, following Andrada *et al.* [113] using the energy-dependent effective mass describing the nonparabolicity of the bands, given by:

$$m_{\parallel;\perp}(E) = \frac{\hbar^2}{2P_{\parallel,\perp;w,b}^2}\left(E + E_{g;w,b}\right) \tag{4.9}$$

where

$$P_{\parallel,\perp;w,b} = \frac{\hbar^2 E_{g;w,b}}{2m_{\parallel,\perp;w,b}(0)} \tag{4.10}$$

are the effective momentum matrix elements [11, 113, 114] which reproduce the experimentally determined band edge effective masses $m_{\parallel,\perp;w,b}(0)$ listed in reference [113].

The $m_{\parallel,\perp}(0)$ for PbTe are extracted from Erasmo *et al.* [113]. For $Pb_{0.9}Eu_{0.1}Te$, the $m_{\parallel,\perp}(0)$ are calculated from Equations 4.11 and 4.12 obtained experimentally from Prinz *et al.* [26].

$$m_{\parallel;b}(0) = 0.31 + 3.23x \quad (4.11)$$

$$m_{\perp;b}(0) = 0.022 + 0.453x \quad (4.12)$$

The energy gap value was calculated from the experimental Equations 4.13 and 4.14 obtained from Abramof *et al.* [114] and Yuan *et al.* [101] for the well and barriers, respectively:

$$E_{g;w}(T) = 190.5 + \frac{0.45T^2}{T+23} \text{ (meV)} \quad (4.13)$$

$$E_{g;b}(T) = E_{g;w}(T) + 0.48\left(\frac{T^2}{T+29}\right)(1 - 7.56x) + 4480x \text{ (meV)} \quad (4.14)$$

The energy gap and the masses used to calculate the confinement energies are summarized in Table 4.1 for $Pb_{0.9}Eu_{0.1}Te$ [26] and PbTe [113].

Table 4.1 Energy gap at T=0,35 K and masses for $Pb_{0.9}Eu_{0.1}Te$ and PbTe. The masses are in units of m_e.

	E_g (meV)	$m_{\parallel}(0)$	$m_{\perp}(0)$
PbTe	190.5	0.310	0.022
$Pb_{0.9}Eu_{0.1}Te$	638	0.633	0.067

Figure 4.13(a) shows the calculated confinement energies for the 10nm wide *p*-type QW (ordinate axis negative part) given by the curve cross sections from Equations 4.1 and 4.2. The sub-bands energies, relative to the valence band bottom, are three longitudinal, 18 meV (±1 meV), 59 meV (±3 meV), 105 meV (±5 meV) and 158 meV (±8 meV) and one oblique with the energy of 68 meV (±7 meV). These values are summarized in Table 4.3. For *n*-type QWs Valmir *et. al* [11] and Peres *et. al* [10] found 6 longitudinal and 3 oblique sub-band. The difference is mainly due to the valence band offset and the electrons and holes effective mass values. In order to verify how

many subbands are participating in the conduction mechanism, the Fermi level value is necessary. Therefore, we integrate the two-dimensional density of states for all possible subbands (one longitudinal and three obliques) and obtain the Fermi level (E_F), according to:

$$p = \int_0^{E_F} d\varepsilon \frac{m_l}{\pi\hbar^2} + 3\int_0^{E_F} d\varepsilon \frac{m_o}{\pi\hbar^2} \tag{4.15}$$

follows that

$$E_F = \frac{p\pi\hbar^2}{(m_l+3m_o)} \tag{4.16}$$

At T=0.35 K, the carrier concentration from the Hall effect measurements curve is $p = p_H = 1.97x10^{16}$ m^{-2} which allows to calculate $E_F = 54$ meV $(\pm 3\ meV)$. These values indicates that only the first longitudinal sub-band with 18 meV participates in the conduction, as show in Figure 4.13(b), where the diagram shows the Fermi energy and confinement energies. Therefore, the odd filling factors are not a consequence of the PbTe multivalley character as was the case for *n*-type QW [11].

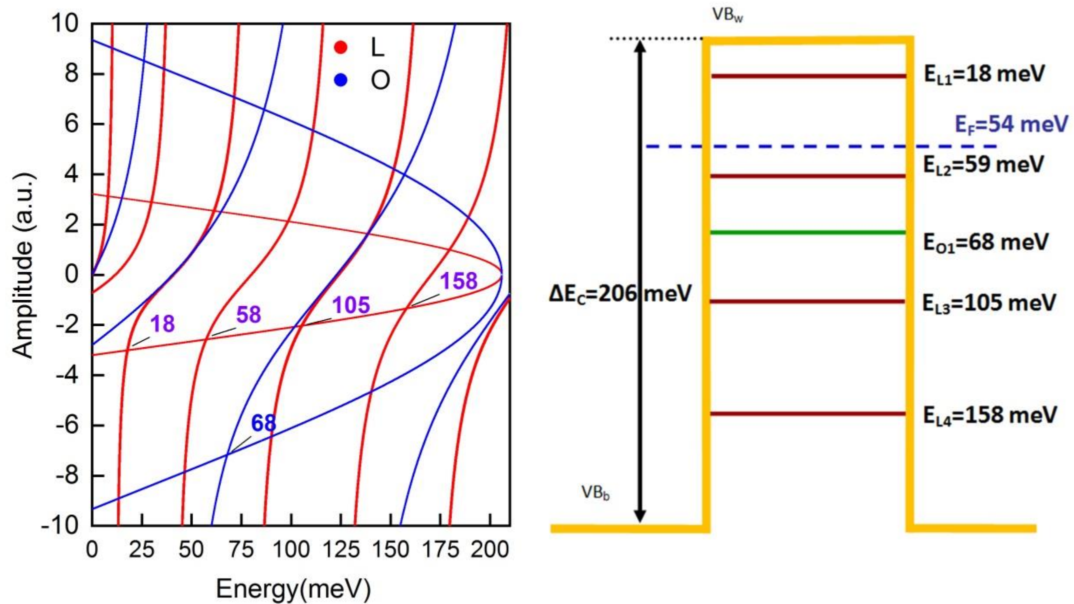

Figure 4.13 (a) Confinements energies calculated from Equations 4.1 and 4.2. (b) Confinement energy diagram with the Fermi level calculated for *p*-type QW.

We can also analyze the sub-bands energy taking into account the Landau level spin splitting and compare with the Fermi energy. As mentioned in Chapter 2, the high *g* factor value leads to a well resolved spin splitting even at low magnetic fields [115, 116]. For higher fields, this may result in a spin splitting in the order, or higher, than Landau level splitting [23]. The sub-bands energy for the case with *B* parallel to the [111] direction can be written as [11, 117]:

$$\varepsilon_{\uparrow}(E_i, n, B) = E_i + \frac{1}{2}(a_n + b_n) + \frac{1}{2}[(a_n - b_n)^2]^{\frac{1}{2}} \quad (4.17)$$

$$\varepsilon_{\downarrow}(E_i, n, B) = E_i + \frac{1}{2}(c_{n-1} + d_{n-1}) + \frac{1}{2}[(c_{n-1} - d_{n-1})^2]^{\frac{1}{2}} \quad (4.18)$$

where E_i is the confinement energy already calculated and shown in Figure 4.13(a), $n = 0, 1, 2, \ldots$ is the orbital number, ↑ and ↓ is for a spin up and down states respectively, and the terms a_n, b_n, c_n and d_n are defined below:

$$a_n = \hbar\omega_t^- \left(n + \frac{1}{2}\right) + \frac{1}{2} g_l^- \mu_B B \quad (4.19)$$

$$b_n = \hbar\omega_t^+ \left(n + \frac{3}{2}\right) - \frac{1}{2} g_l^+ \mu_B B \quad (4.20)$$

$$c_n = \hbar\omega_t^+ \left(n + \frac{3}{2}\right) - \frac{1}{2} g_l^- \mu_B B \quad (4.21)$$

$$d_n = \hbar\omega_t^+ \left(n + \frac{1}{2}\right) + \frac{1}{2} g_l^+ \mu_B B \quad (4.22)$$

The term $\omega_t^{\pm} = eB/m_t^{\pm}$ corresponds to the transversal cyclotron frequency, while $m_t^+ = 0.12m_e$ and $m_t^- = 0.10m_e$ are the transverse masses; $g_l^+ = 2.61$ and $g_l^- = 1.72$ are the longitudinal *g* factors. The mathematical symbols (+) and (-) denote the valence and conduction bands, respectively, and μ_B is the Bohr magneton. Thus, for *p*-type PbTe QW the terms a_n and c_n are zero and the other parameters used are summarized in Table 4.2 and extracted from [86].

Table 4.2 PbTe band parameters from Bauer *et al.* [86] used to calculate the Landau levels spin splitting. Masses are expressed in units of m_e.

E_g (eV)	$2P_{\parallel}^2/m_e$	$P_{\perp}/P_{\parallel}$	m_t^-	m_t^+	g_l^-	g_l^+
0.19	6.02 eV	3.42	0.10	0.12	1.72	2,61

The splitting simulation for this sample is shown in Figure 4.14(a), taking into account the first longitudinal 20 meV sub-band and $n = 0, 1, 2, 3$ and 4. The calculated Fermi level value ($E_F = 54$ meV) plotted together with the R_{xx} and $1/R_{xy}\,(e^2/h)$, in Figure 4.13(b), shown that below the Fermi level, the number of degenerated sub-bands is equal to the integer filling factors 2, 4, 6, 7 and 9. This means that the sub-bands splitting, due to the magnetic field, taking into account the Zeeman and Landau effect, may justify the odd filling factors sequence.

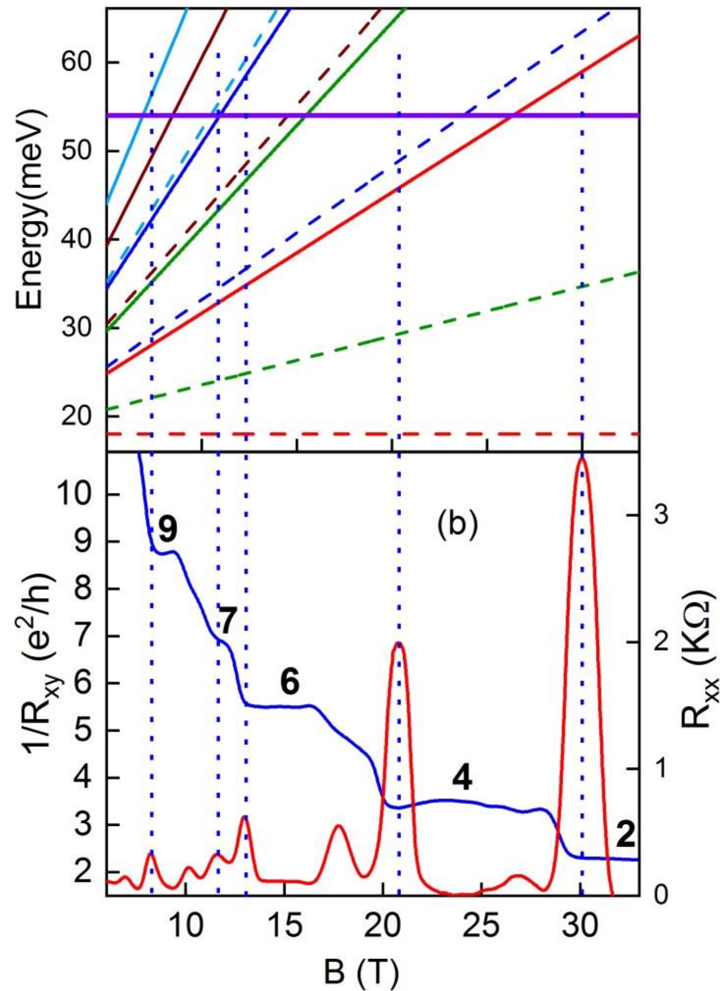

Figure 4.14. Landau spin splitting fan chart diagram where (a) are the calculated Landau spin splitting energy levels for the first longitudinal sub-band (L1=18 meV), which the dotted and solid curves being the spin down and up, respectively; the red, green, dark blue, brown and light blue curves corresponding to the quantum numbers 0, 1, 2, 3 and 4, respectively and the violet line is the Fermi level, with E_F=54 meV, calculated from the Hall effect carrier concentration. (b) The $1/R_{xy}$ in units of e^2/h (blue curve), along with R_{xx} (red curve) data for T=0.35 K. The vertical dotted blue lines that cross R_{xx} peaks and $1/R_{xy}$ plateaus reaching E_F curve, delimit how many sub-bands are participating in the conduction mechanism, corresponding to the calculated LL 2, 4, 6, 7 and 9.

The spin effect should appear in the SdH oscillations as two close frequencies, instead of just one, originating from the 18 meV sub-band that participates in the conduction mechanism. Therefore, to better understand the transport mechanism, fast Fourier transform (FFT) analysis is necessary. To withdraw the linear background, the first derivative of R_{xx} was performed and plotted as a function of the inverse of the magnetic field for temperatures varying from 0.35 K up to 30 K, as shown in Figure 4.15(a). The obtained frequencies are shown in Figure 4.15(b) for the same temperatures range. We notice the appearance of three main frequencies peaks at 19 T (±3 T); 32 T (±3 T) and 45 T (±2 T). The two more intense ones, 32 T and 45 T, result in a total frequency of 77 T, close to the 82 T value obtained from the Landau fan diagram (inset of Figure 4.11(b)), considering the associated errors. Furthermore, the figures present smooth intensity depletion as temperature decreases. Also, from Figure 4.15(c), that shows the FFT for different magnetic field range, it is clear that these two peaks appear together. This indicates that they originate from spin up and down degeneracy [118, 119]. The third one (19 T) is close to the 18 T obtained from Figure 4.10 (a) for B up to 9 T. However, 19 T second harmonic should be 38 T and it is situated around the middle of the other two. It is possible that the 32 T and 45 T peaks are the 19 T second harmonic splitting. Another indication that 19 T frequency peaks originated from the SdH oscillations is its presence when different windows function, applied for the same B interval, are used, as shown in Figure 4.15(d).

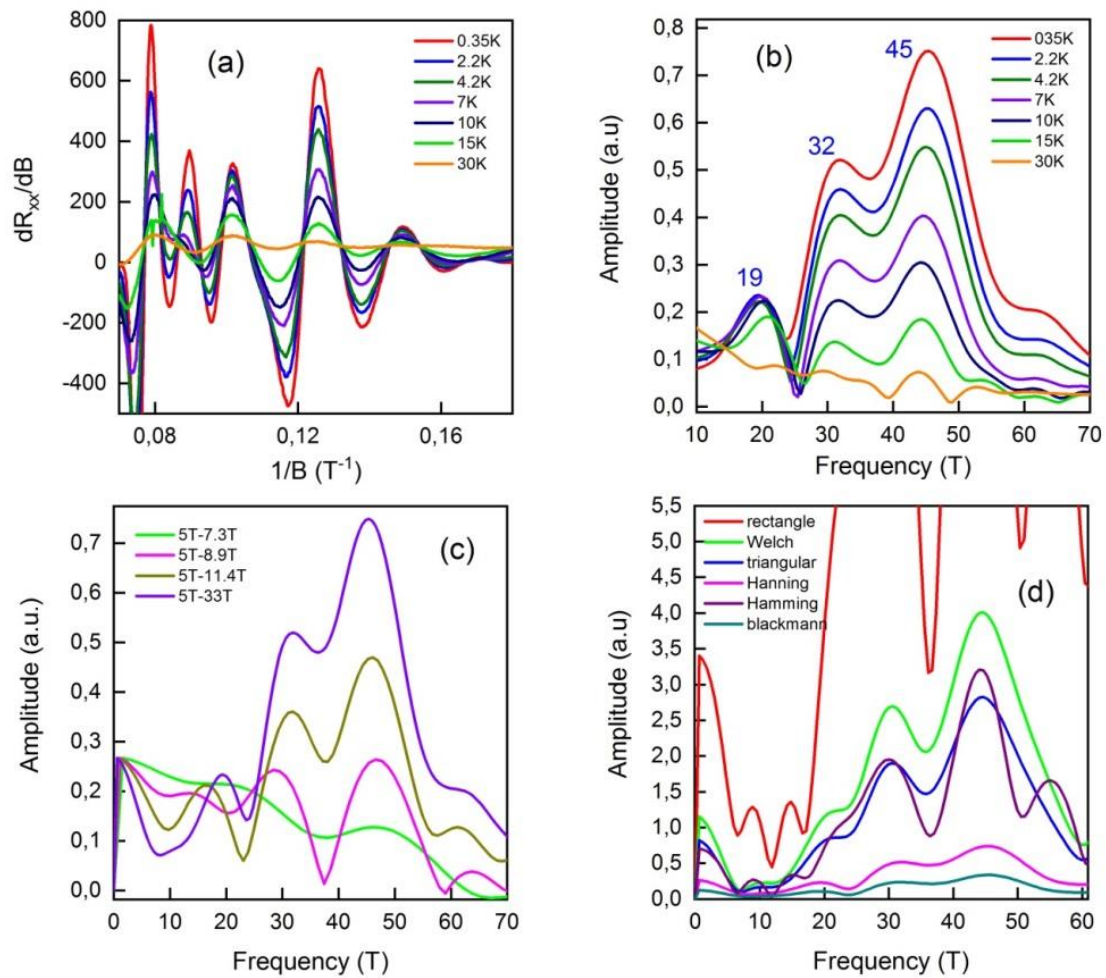

Figure 4.15 (a) first derivative of R_{xx} as a function of the inverse of magnetic field for different temperatures (b) frequencies obtained from FFT analysis for temperatures varying from 0.35 K, which present the higher intensity, up to 30 K, with almost no beat pattern (c) FFT for different magnetic field range and (d) FFT for different windows function in the same field range.

The g factor, related to the Zeeman effect, can be extracted from the oscillations if B is sufficiently high to show the Landau level separation, due to the spin splitting. This calculation can be carried out using Equation 2.65. Figure 4.16(a), shows the plot of dR_{xx}/dB as a function of $1/B$. The splitting becomes clear for higher fields as expected since the energy Zeeman spin-splitting varies with $g\mu_B B/2$, appearing as double peaks in the oscillatory component of R_{xx}. By making the correct association of these peaks in Figure 4.16(a), with the Landau level splitting, shown in Figure 4.16(b), and with the Equation 2.65, we calculate the g factor values of 43, 53, 33 and 31

for the respective n-values of 1, 2, 3 and 4 in accord with Figure 4.16(a). These high g values are in agreement with the discussion above and may be responsible for the odd filling factor sequence.

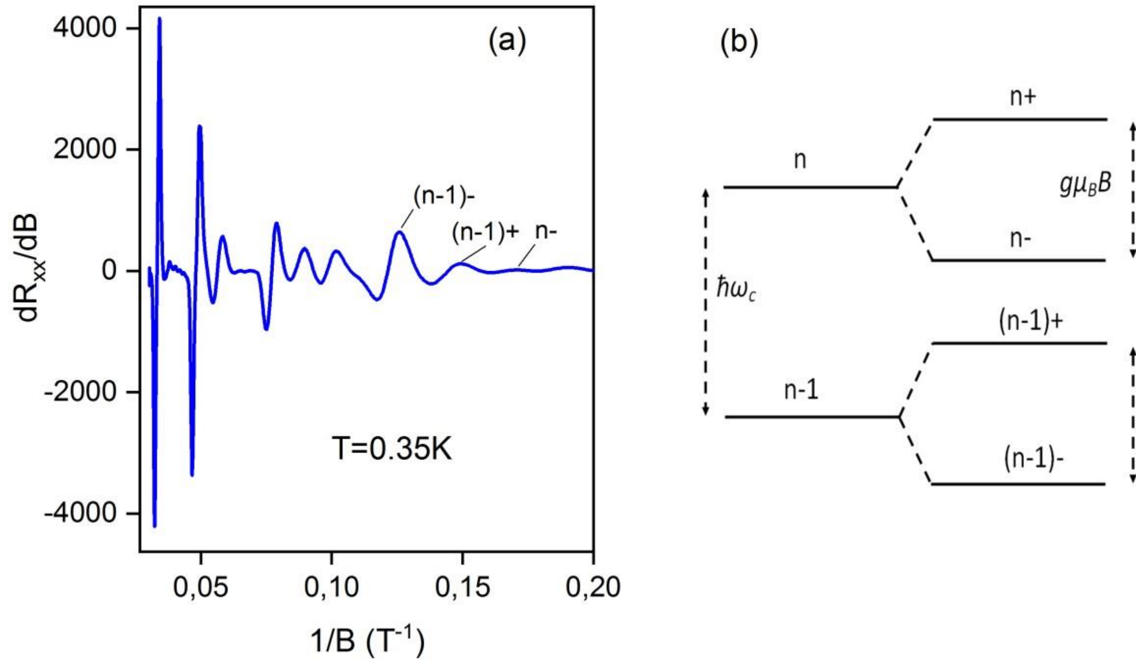

Figure 4.16 (a) First derivative of the normalized R_{xx} as a function of *1/B* at 0.35 K showing the doubling of the peaks due to the Landau level spin splitting and the associated $n_i \pm$ peaks used to calculate the g factor. (b) Landau level n and (n-1) splitting into spin down (-) and spin up (+) states.

Once the fractional filling factors (*ff*) values may be originated from remaining parallel conduction through the barriers of PbEuTe, we illuminated the 10 nm well width sample using a commercial red LED in order to enhance the conduction through the well channel. This enhancement occurred for the photoconductivity results discussed in section 4.1. Figure 4.17(a) shows the 10nm QW thickness R_{xx} (full line) and R_{xy} (dotted line) curves with (ON) and without (OFF) illumination at 3 K temperature. The illuminated and non-illuminated sample presented clear SdHO and the QHE. However, unlike expected, it also presented fractional filling factors values: 3.8; 4.7; 5.9; 8.1 and 9.6. Therefore, for this analysis, we consider the approximated values: 4; 5; 6; 8 and 10, calculated according to Equation 2.40. These are higher values when compared with the 2; 4; 6; 7 and 9 from the non-illuminated sample. The increase in the *ff* is due to the carrier

concentration increase by the illumination. This assumption is in accordance with Figure 4.17(b), where the carrier concentration obtained by Hall effect measurements for illuminated (red triangle curve) and dark (blue circle curve) condition are shown. From this figure, the carrier concentration increases from $p_{OFF} \approx 2.01 \times 10^{16}$ m^{-2} to $p_{ON} \approx 2.32 \times 10^{16}$ m^{-2} for 3 K.

Also, as done for the 10nm well width in the dark condition, the odd *ff* sequence may be justified by the Landau spin splitting fan chart diagram presented in Figure 4.17(c) and comparing with the R_{xx} oscillations peak and the $1/R_{xy}(e^2/h)$ plateaus as shown in Figure 4.17(d). For the Landau spin splitting fan chart diagram, we use the 18 meV first longitudinal sub-band and the 61 meV (±4 meV) Fermi level, calculated taking into account all possible sub-bands (Equation 4.16), using the 3 K temperature carrier concentration value and the quantum numbers of 0, 1, 2, 3 and 4. Comparing Figure 4.17 (c) and (d), for all R_{xx} oscillations peak, the corresponding *ff* values are the same as the number of degenerated sub-bands below the Fermi level.

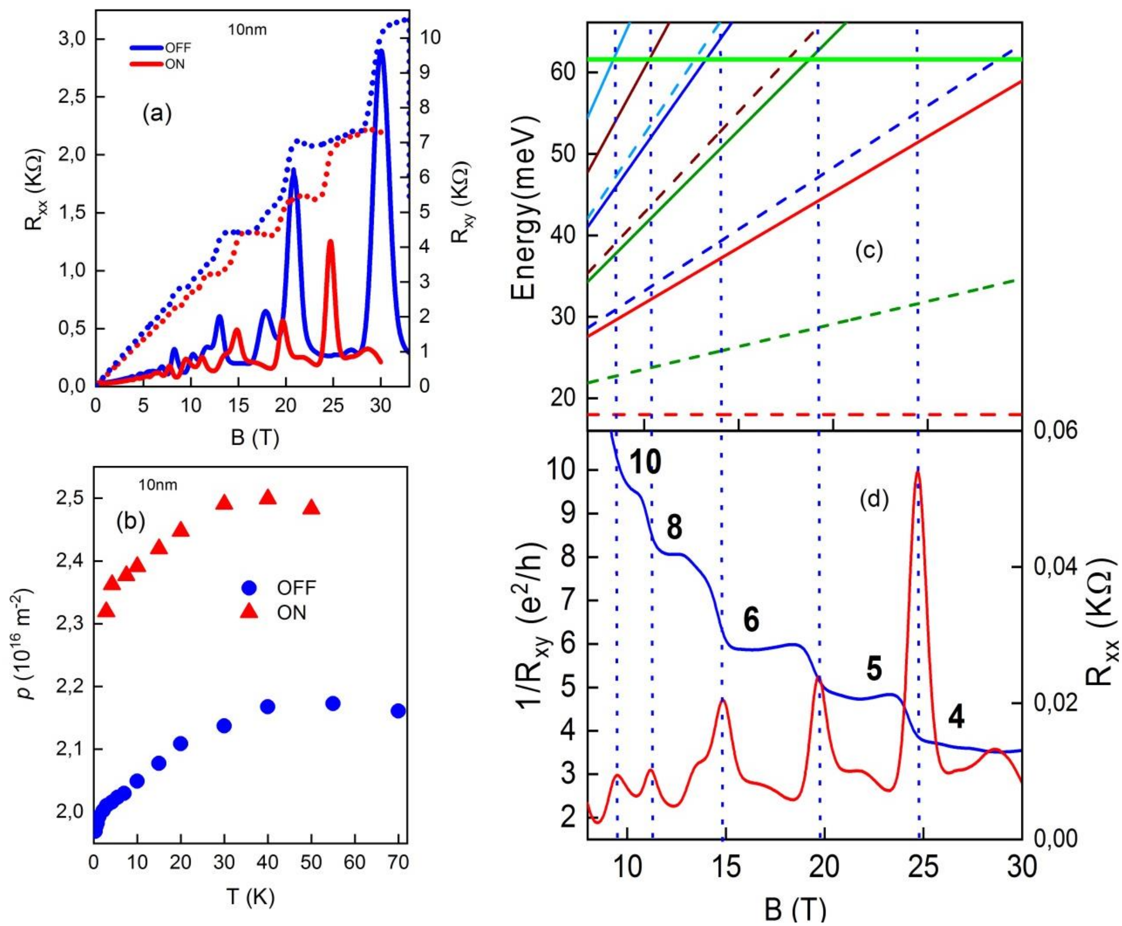

Figure 4.17 (a) shows the R_{xx} and R_{xy} for 10 QW thickness at T = 3 K with (ON) and without (OFF) illumination. (b) Carrier concentrations obtained by Hall effect measurements with illumination (red triangles) and without illumination (blue circles). (c) and (d) are the Landau spin splitting fan chart diagram where (c) are the calculated Landau spin splitting energy levels for illuminated sample which the dotted and solid curves being the spin down and up, respectively; the red, green, dark blue, brown and light blue curves corresponding to the quantum numbers 0, 1, 2, 3 and 4, respectively and the light green line is the Fermi level, of E_F=61 meV and (d) is the $1/R_{xy}$ in units of e^2/h (blue curve), along with R_{xx} (red curve) data for T=3 K. The vertical dotted blue lines that cross R_{xx} peaks and $1/R_{xy}$ plateaus reaching E_F curve, delimit how many sub-bands are participating in the conduction mechanism, corresponding to the calculated LL 4, 5, 6, 8 and 10.

In Figure 4.8, the 20 nm well width sample shows a possible initial oscillation profile, for B up to 9 T, however, a higher magnetic field is necessary. In order to obtain further information about the magnetotransport properties well width dependence, a 15 nm QW thickness is investigated. Thus, the 15 and 20 nm QW thickness measurements data are discussed next, following the same procedure used above for the 10 nm well width sample. Figure 4.18 (a) and (b) show the 15 and 20 nm well width electrical longitudinal R_{xx} (solid curve) and the Hall resistance R_{xy} (dotted curve), respectively. The measurements are performed for a magnetic field up to 33 T and at 2.2 K

temperature. In these figures the R_{xy} plateaus are clearly visible, for both samples, indicating the Landau level quantization. The SdHO are also present in the R_{xx} curves. These profiles indicated the 2DEG electronic confinement and high samples quality. For the 15 nm QW thickness, Figure 4.18(a), for 11, and 17 and 32 T magnetic field values, flat plateaus in R_{xy} and the zero resistance in R_{xx} are well defined. An exception occurs in R_{xx} curve at $B > 27$ T where an interference appears in the signal, turning it into negative values that prevent the expected zero R_{xx} resistance at B=32 T. This negative signal may be associated to contact issues. The QHE and SdHO profiles are also present in Figure 4.18(b), for the 20 nm well width, at 10 and 27 T magnetic field values. However, an R_{xx} anomalous behavior appears for $B > 22$ T preventing the expected zero profile at B=28 T. This anomaly does not seem to be originated from contact issue as it differs from the 15 nm well width behavior for $B > 27$ T, however, it is already known that the edge states can cause anomalies in the SdHO [107].

Figure 4.18 (c) and (d) present the plotting of the inverse of the Hall resistance in units of (e^2/h) as a function of B for 15 and 20 nm QW thickness, respectively, at 2.2 K. From this figure, the filling factors (v) values directly obtained are 1, 2 and 3 for the 15 nm QW thickness and 1.4 and 2 for the 20 nm one. The 20 nm well width sample exhibit one integer value of v, at B=10 T, and one fractionary, at B=27 T. The expected v values, considering the corresponding B, are 1 and 2. Besides, the factionary v value is in the region where the anomaly appears in the R_{xx} curve and may be caused by the edge states. The 15 nm QW, unlike the 10 and 20 nm well widths, exhibit sequential integers v as expected for these samples [11]. From Equation 2.54 ($v \propto F/B$), a linear behavior is expected between v and *1/B*, however, only a few plateaus are visible in Figures 4.18 (c) and (d). We then associated multiple of 1 (one) and 0.5 (half) to the R_{xx} peaks and valleys, respectively, plotting it with the corresponding B values, as shown in the insets of Figures 4.18 (c) and (d). From the linear fittings, the obtained frequency values are 26 T (±2 T) and 13 T (±1 T) for the 15 nm and 20 nm QW thicknesses, respectively. The calculated values obtained from the frequencies are $p_{15nm} = 6.43 \times 10^{15}\ \mathrm{m}^{-2}((\pm 0.48 \times 10^{15}\ \mathrm{m}^{-2})$ and $p_{20nm} = 3.17 \times 10^{15}\ \mathrm{m}^{-2}$ $(\pm 0.36 \times 10^{15}\ \mathrm{m}^{-2})$. The values obtained from the Hall effect measurements are $\rho_{15nm}^{Hall} = 8.49 \times 10^{15}\ \mathrm{m}^{-2}$ $(\pm 0.30 \times 10^{15}\ \mathrm{m}^{-2})$ and $\rho_{20nm}^{Hall} = 7.08 \times 10^{15}\ \mathrm{m}^{-2}$ $(\pm 0.47 \times 10^{15}\ \mathrm{m}^{-2})$.

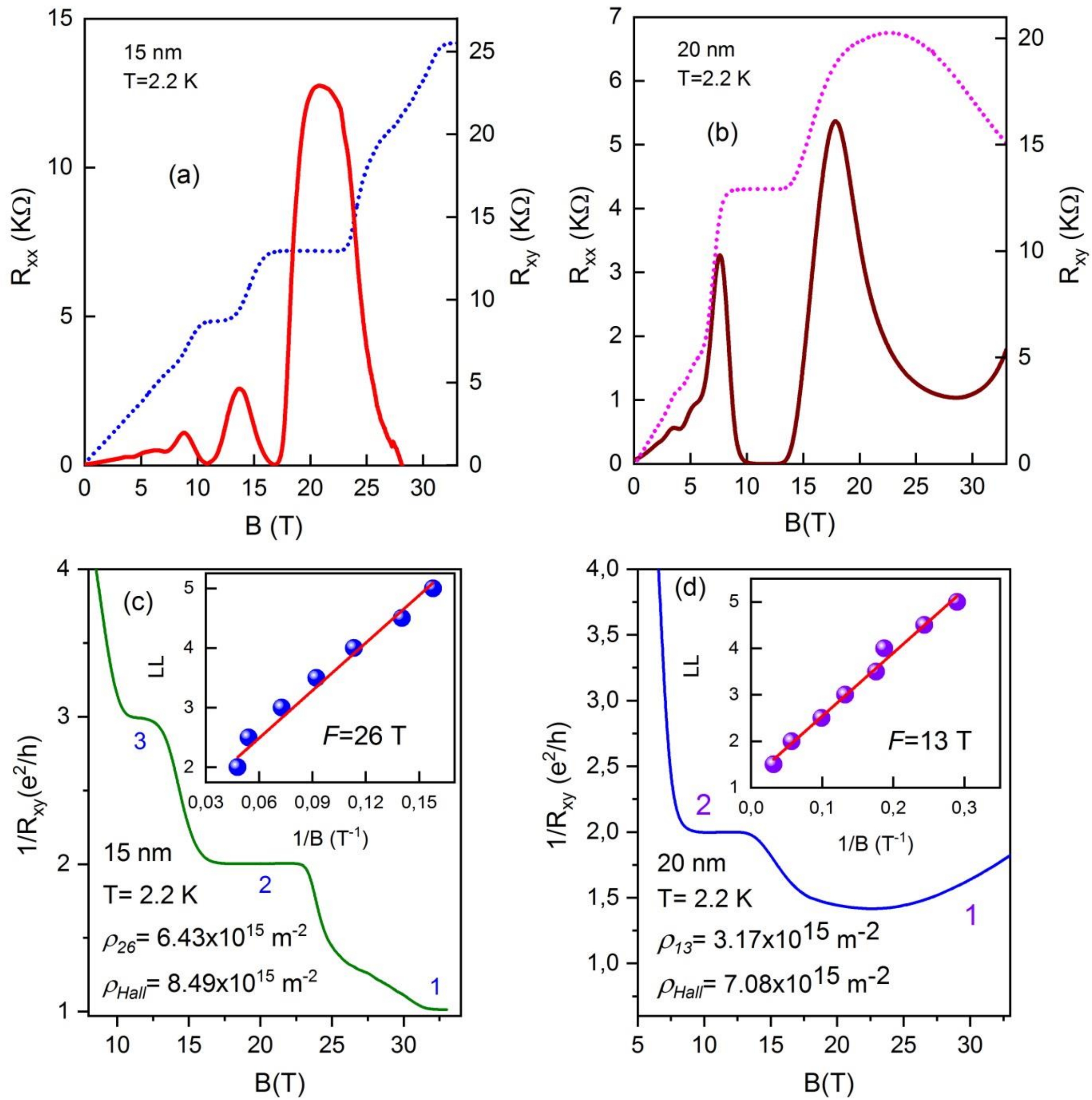

Figure 4.18. (a) and (b) show the R_{xx} and R_{xy} for 15 and 20 nm QW thickness, respectively, at $T = 2.2$ K. (b) and (c) present $1/R_{xy}$ in units of e^2/h and the insets are the Landau levels fan diagram for 15 and 20 nm well width samples, respectively.

The relation between the carrier concentrations calculated from the frequencies and from the Hall effect are $p_{26}/\rho_{15nm}^{Hall} = 0.74$ and $p_{13}/\rho_{20nm}^{Hall} = 0.44$ for the 15 and 20 well width samples, respectively. It is clear that the carrier concentration calculated by the Hall effect is higher than the value obtained from the Landau fan diagram frequencies. This difference is very large to be only caused by the edge states. Also, we can notice that the carrier difference increases with the rise of the QW thickness, being the differences, 0.94, 0.74 and 0.44 for the 10, 15 and 20 nm QW thickness

samples, respectively. It is possible that an extra conduction channel in the interface between the barrier and the well are participating in the conduction, the wider the well thickness, the greater the contribution to the total conduction. This interface channel can be responsible for the carrier difference.

The frequency values can be verified by FFT analysis as a function of temperature, performed on the longitudinal resistance derivative curves, shown in Figure 4.19 (a) and (b) for the 15 and 20 nm well width samples, respectively. The obtained FFT results are presented in Figure 4.19 (c) and (d) for the 15 and 20 nm QW thickness, respectively. For the 15 nm QW thickness, Figure 4.19 (c), a Hanning windows function applied for the 6 – 23 T magnetic field range, provided a value of 23 T (±2 T) and a carrier concentration of $\rho_{23} = 5.56 \times 10^{15}\ \mathrm{m}^{-2}\ (\pm 0.48 \times 10^{15}\ \mathrm{m}^{-2})$. Considering the error, these values are in agreement with the calculated from Figure 4.18 (c) inset. However, the difference when compared to the carrier value obtained from Hall effect remains. Also, 41 (±1) and 50 (±3) T frequencies peaks appears with low amplitude and may be the second harmonic spin splitting. As observed for the 10 nm QW thickness, in this case, the 23 T second harmonic (46 T) should be between the 41 T and 50 T peaks. Figure 4.19 (d) exhibit the FFT for the 20 nm well width and three frequencies peaks are present, 13 (±1), 26 (±1) and 40 (±2) T that leads to carriers concentration values of $\rho_{13} = 3.24 \times 10^{15}\ \mathrm{m}^{-2}\ (\pm 0.24 \times 10^{15}\ \mathrm{m}^{-2})$, $\rho_{26} = 6.29 \times 10^{15}\ \mathrm{m}^{-2}\ (\pm 0.24 \times 10^{15}\ \mathrm{m}^{-2})$ and $\rho_{40} = 9.67 \times 10^{15}\ \mathrm{m}^{-2}\ (\pm 0.48 \times 10^{15}\ \mathrm{m}^{-2}$. Considering these tree frequencies, the total carrier concentration will be: $\rho_{13+26+40} = 1.90 \times 10^{16}\ \mathrm{m}^{-2}\ (\pm 0.15 \times 10^{16}\ \mathrm{m}^{-2})$, a value which is much higher than Hall values, $\rho_{20nm}^{Hall} = 7.08 \times 10^{15}\ \mathrm{m}^{-2}\ (\pm 0.47 \times 10^{15}\ \mathrm{m}^{-2})$. Moreover, in accordance to Figure 4.18 (d) the frequency of 13 T should appear. Therefore, further information is necessary and can be obtained from the multi-valleys channels that may participate in the charge transport process.

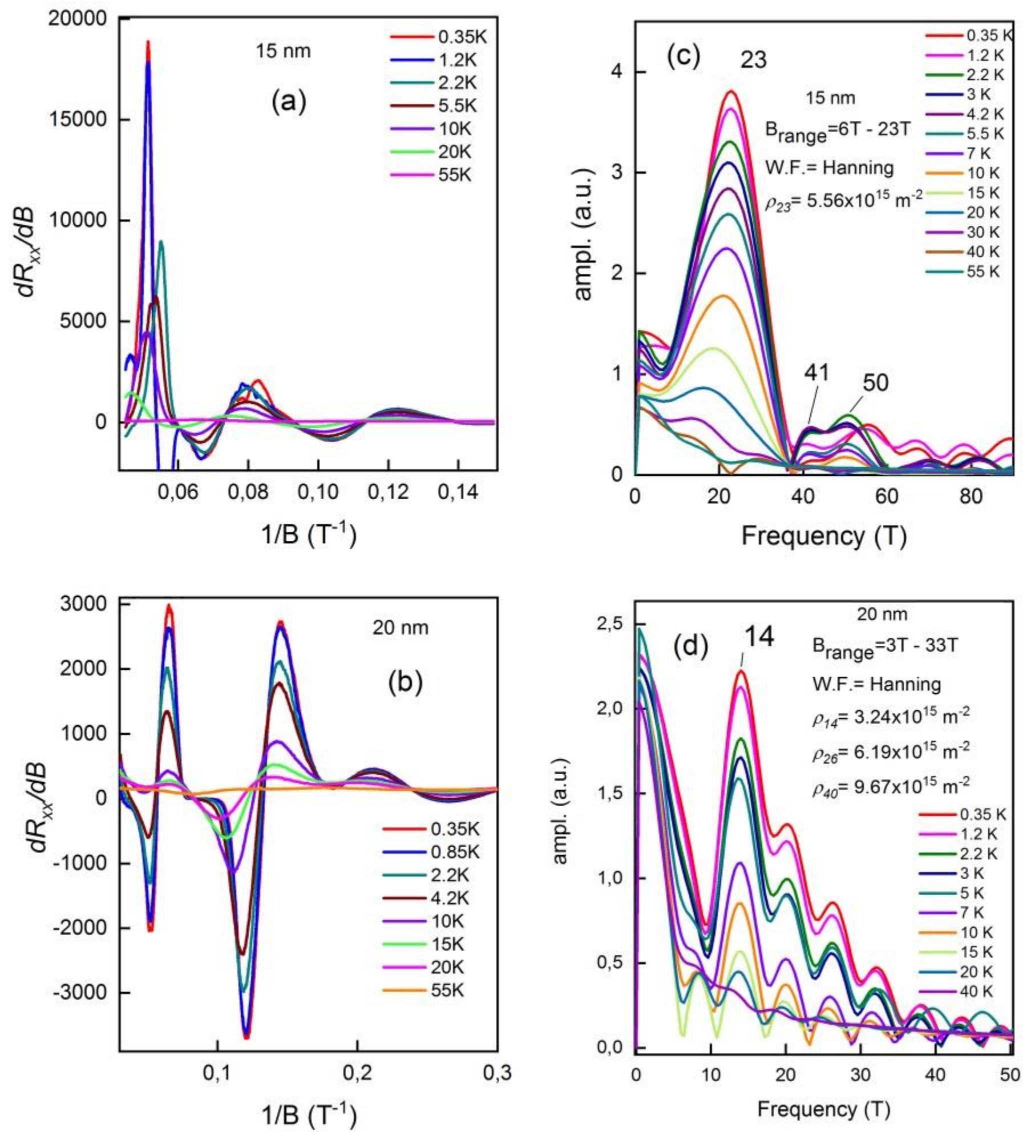

Figure 4.19 15 and 20 nm QW thickness (a) and (b) first derivative of R_{xx} as a function of the inverse of the magnetic field for different temperatures. (c) and (d) frequencies obtained from FFT analysis for temperatures varying from 0.35 K, which present the higher intensity, up to 55 K, with almost no beat pattern.

Following the same procedure from 10 nm well width sample, we solve the Equations 4.1 and 4.2 for the 15 nm QW thicknesses. The results are shown in Figure 4.20 (a) and from the intersections of the curves, the confinement energies (E_a) are obtained. Figure 4.20 (c) exhibits, schematically, the E_a values together with the Fermi level of 23 (±2) meV for the 15 well width samples. The Fermi level is calculated in accord with Equation 4.16, using $\rho_{15nm}^{Hall} = 8.49 \times 10^{15}\ \mathrm{m}^{-2}$ $(\pm 0.30 \times 10^{15}\ \mathrm{m}^{-2})$ employing the mass values presented in Table 4.1. The calculated

confinement energies are summarized in Table 4.3 with their respective errors. In accordance to Figure 4.20 (c), the 15 nm well width sample should present only one frequency related to the E_{L1} = 7 meV (±1 meV) sub-band. This result is in agreement with Figure 4.19 (c) and Figure 4.18 (c), where the main frequency peak of ~23 T should arise from the first longitudinal sub-band (L_1 = 7 meV) that participate in the conduction mechanism. It also supports our previous assumption that the two other peaks (41 and 50 T), from Figure 4.19 (c), arise from the spin splitting.

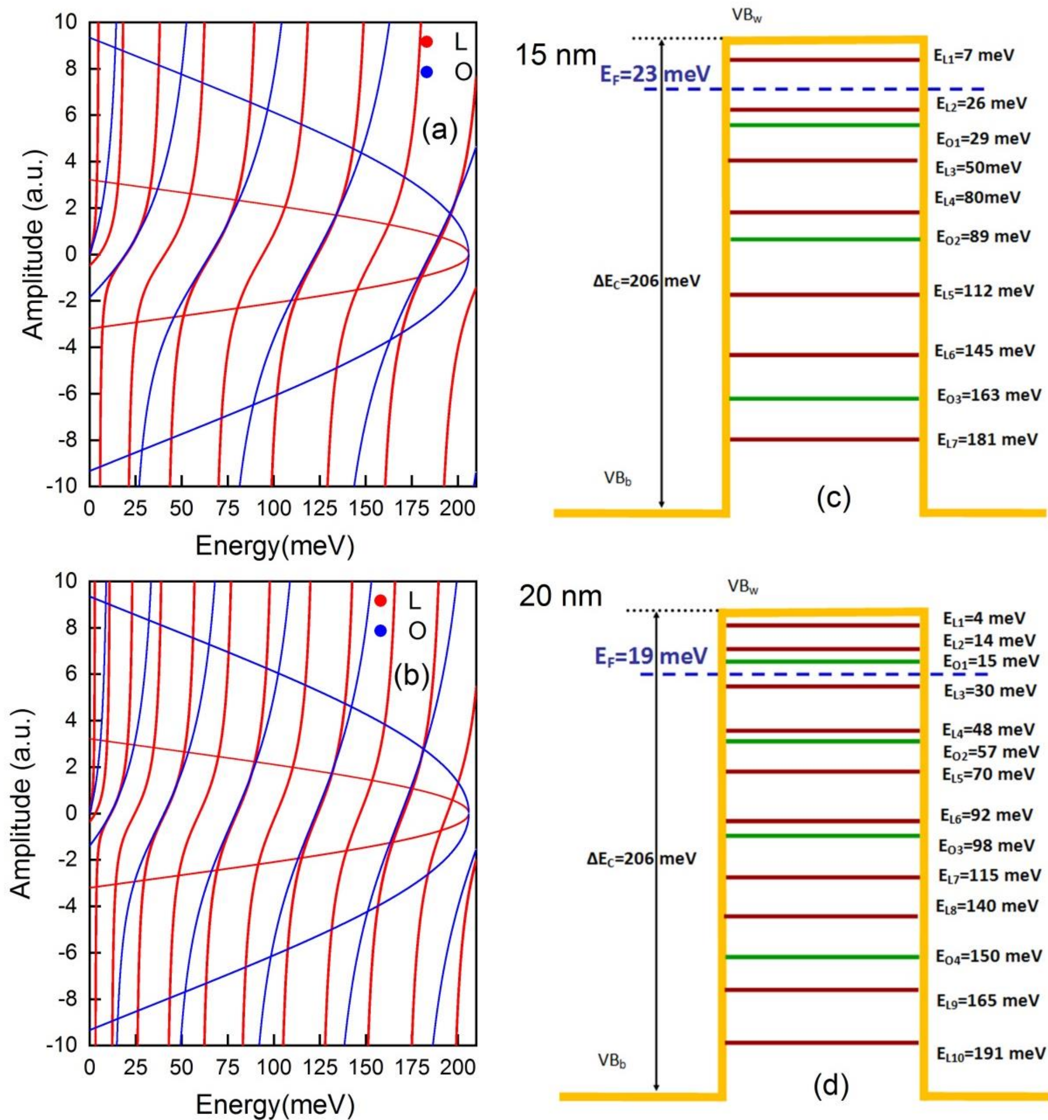

Figure 4.20 (a) and (b) Confinements energies calculated from Equations 4.1 and 4.2, given by the cross sections curves; (c) and (d) are the confinement energy diagram with the 23 (±2), 19 (±2) meV Fermi level calculated for the 15 and 20nm *p*-type QW, respectively.

Table 4.3 Confinement energies calculated using the envelope function model, developed for lead-salt QWs, using the Ben Daniel-Duke like boundary conditions, considering the even and odd solutions and their respective calculated errors for the 10, 15 and 20 nm QW thickness samples.

	Confinement energy (meV)													
Degenerated level	L_1	L_2	L_3	L_4	L_5	L_6	L_7	L_8	L_9	L_{10}	O_1	O_2	O_3	O_4
10 nm well width	18	59	105	158	x	x	x	x	x	x	68	x	x	x
Error (±)	4	10	16	23	x	x	x	x	x	x	12	x	x	x
15 nm well width	7	26	50	80	112	145	181	x	x	x	29	89	163	x
Error (±)	1	3	5	8	11	13	15	x	x	x	3	9	11	x
20 nm well width	4	14	30	48	70	92	115	140	165	191	15	57	98	150
Error (±)	1	1	3	4	5	7	7	10	10	102	2	4	7	8

Solving the Equations 4.1 and 4.2 for the 20 nm well width sample, we found the confinement energies (E_a). The results are shown in Figure 4.20 (b) where the E_a is obtained from the intersections of the curves. Figure 4.20 (d) schematically exhibit the E_a values together with the Fermi level of 19 (±2) meV, calculated in accord with Equation 4.16 using $\rho_{20nm}^{Hall} = 7.08 \times 10^{15}\ \mathrm{m}^{-2}$ ($\pm 0.47 \times 10^{15}\ \mathrm{m}^{-2}$) and the mass values presented in Table 4.1. The calculated confinement energies are summarized in Table 4.3 with their respective errors. According to Figure 4.20 (d), the 20 nm well width sample should have three sub-bands participating in the charge conduction, two longitudinal (L_1= 4 meV and L_2= 14 meV) and an oblique one (O_1= 15 meV). This result agrees with the three peak frequencies from the FFT analysis presented in Figure 4.19 (d). However, it disagrees with the only main frequency presented in the inset of Figure 4.18 (d). Also, if we take the carrier concentration of $\rho_{13} = 3.24 \times 10^{15}\ \mathrm{m}^{-2}$ calculated from the 13 T frequency (see inset in Figure 4.18 (d)) we obtain 8.4 meV for the Fermi energy. Using this value to find how many sub-bands lay above the Fermi level in the confinement energy diagram, shown in Figure 4.20 (d), we can notice that just the first longitudinal sub-band participates in the conduction. This also agrees with our previous assumption that an extra layer is formed by the PbEuTe, from the

barrier, diffusion through the PbTe layer. Furthermore, the 26 T and 40 T frequencies will be the 13 T second and third harmonic, respectively. Further information about the calculated frequencies, and how many sub-bands are participating in the conduction mechanism, can be obtained from the Landau spin splitting fan chart diagram, shown next.

Following the same procedure from 10 nm QW thickness sample, using the Equations 4.17 and 4.18 and the PbTe band parameters from Table 4.2 we obtain Figure 4.21. In this figure the Landau spin splitting fan chart diagram, for the 15 and 20 nm well width sample, are shown together with the $1/R_{xy}$ in units of e^2/h along with R_{xx}. Figure 4.21 (a) shows the spin splitting simulation for the 15 nm QW thickness sample, where the first longitudinal sub-band (L_1) spin up (full line) and spin down (dotted line), using the two first quantum numbers n= 0 (red curve) and n= 1 (blue curve) are shown together with the 23 meV Fermi level. Comparing Figure 4.21 (a) with Figure 4.21 (b), where the $1/R_{xy}$ in units of e^2/h, along with R_{xx} for the 15 nm well width is shown, it is clear that for all R_{xx} oscillations peak, the corresponding *ff* values are the same as the number of degenerated sub-bands below the Fermi level. Satisfactorily agreeing with the 15 nm well width analysis from above, where just the first longitudinal sub-band (L_1= 7 meV) is participating in the conduction mechanism. For the 20 nm QW thickness sample, Figure 4.21 (c) shown the spin splitting simulation using the first longitudinal sub-band (L_1= 4meV) spin up (full line) and down (dotted line), for the first quantum number n= 0 (red curve) together with the 19 meV Fermi level; and Figure 4.21 (d) present the $1/R_{xy}$ in units of e^2/h, along with R_{xx}. From these figures, it is clear that the corresponding *ff* values, for all R_{xx} oscillations peak, are the same as the number of degenerated sub-bands below the Fermi level. This leads us to assume that the other frequencies, 26 and 40 T, are in fact the 13 T frequency second and thirty harmonics, respectively. Also, the carrier concentration difference, between Hall measurements and the frequency calculations, can originate from an extra conduction channel formed by the PbEuTe diffusion through the PbTe. Thus the conduction through this extra channel may be enhanced with illumination, as occurred for the 10 nm well width sample.

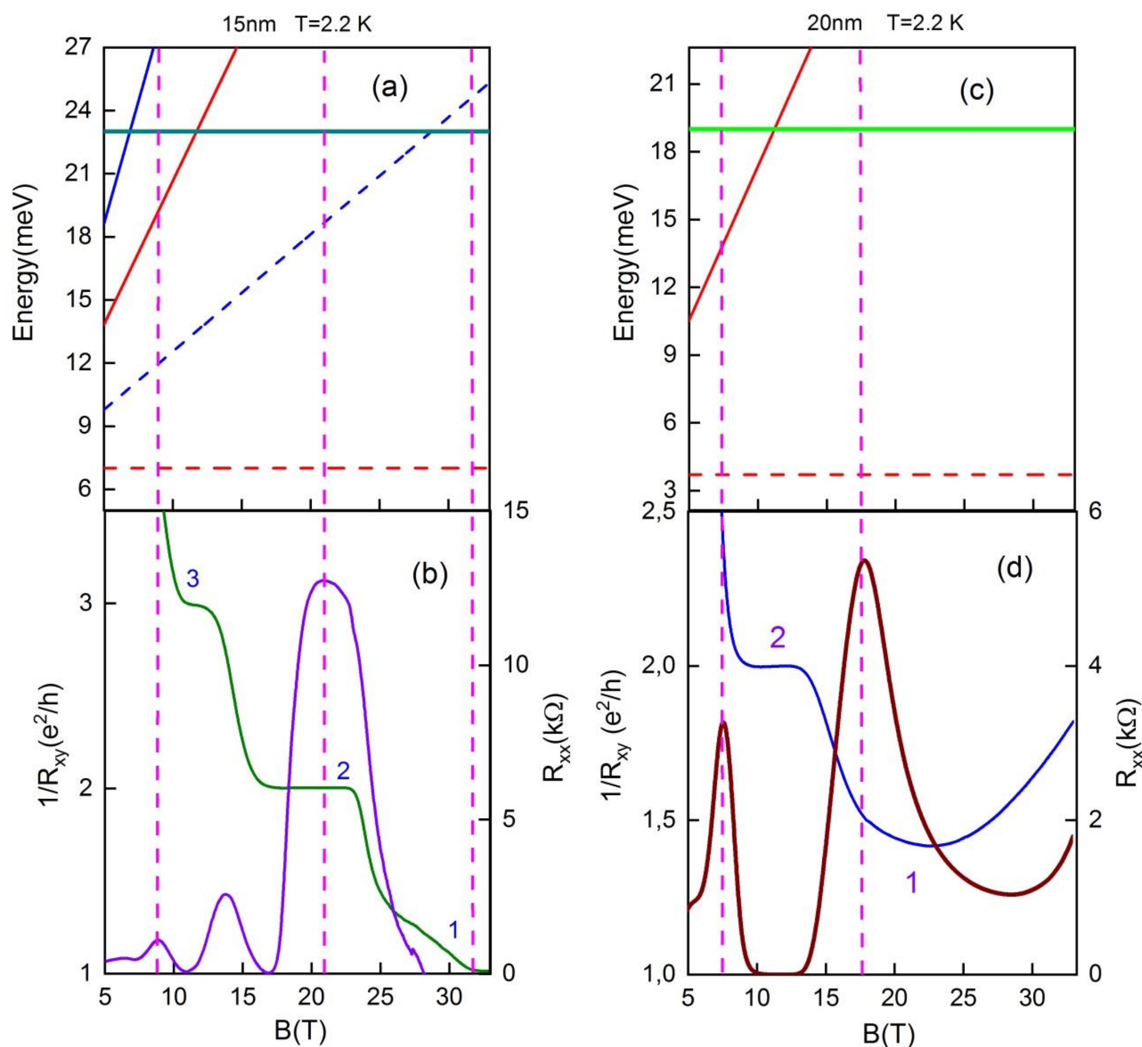

Figure 4. 21 Landau spin splitting fan chart diagram where (a) and (c) are the calculated Landau spin splitting energy levels for the first longitudinal sub-band, L_1=7 and 4 meV for the 15 and 20 nm well width samples, respectively. With the dotted and solid curves being the spin down and up, respectively; the red and blue curves corresponding to the quantum numbers 0 and 1, respectively and the green (dark and light) line being the Fermi level, with 23 and 19 meV, calculated from the Hall effect carrier concentration for the 15 and 20nm QW thickness, respectively. (b) and (d) shown the $1/R_{xy}$ in units of e^2/h (green and blue curves), along with R_{xx} (violet and brown curves) data for 15 and 20 nm well width samples, respectively, at T=2.2 K. The vertical dotted lines that cross R_{xx} peaks and $1/R_{xy}$ plateaus reaching E_F curve, delimit how many sub-bands are participating in the conduction mechanism, corresponding to the calculated LL.

Figure 4.22 shows the magnetotransport results for the illuminated 20 nm QW thickness sample. Figure 4.22 (b) shows the R_{xx} measurements results, with (ON - red full curve) and without (OFF - blue dotted curve) illumination. In this figure, it is clear that the SdHO peak, under illumination,

suffers a shift for lower B values when compared with the non-illuminated sample, as indicated by the green arrows in the Figure 4.22 (b) inset, where an R_{xx} zoon-in is shown. Also, the illuminated R_{xx} curve amplitude, exhibit higher resistance for B>10 T and rapidly increasing for B>25 T, when compared with the non-illuminated sample curve. The resistance gain reaches a value of 4550% higher than the 20 nm QW thickness without illumination at 33 T. Similar behavior is observed for the illuminated and non-illuminated R_{xy} measurement results as shown in Figure 4.22 (a), where the R_{xy} with (ON - red full curve) and without (OFF - blue dotted curve) illumination are presented. In this figure, it is clear that the transversal resistance curves, for illuminated and non-illuminated sample, present almost the same amplitude for B<25 T and rapidly increase for B>25 T reaching, at 33 T, a value 820% higher than the curve without illumination. These effects can originate from the change in the carriers concentration when light is applied, as discussed in section 2.2.

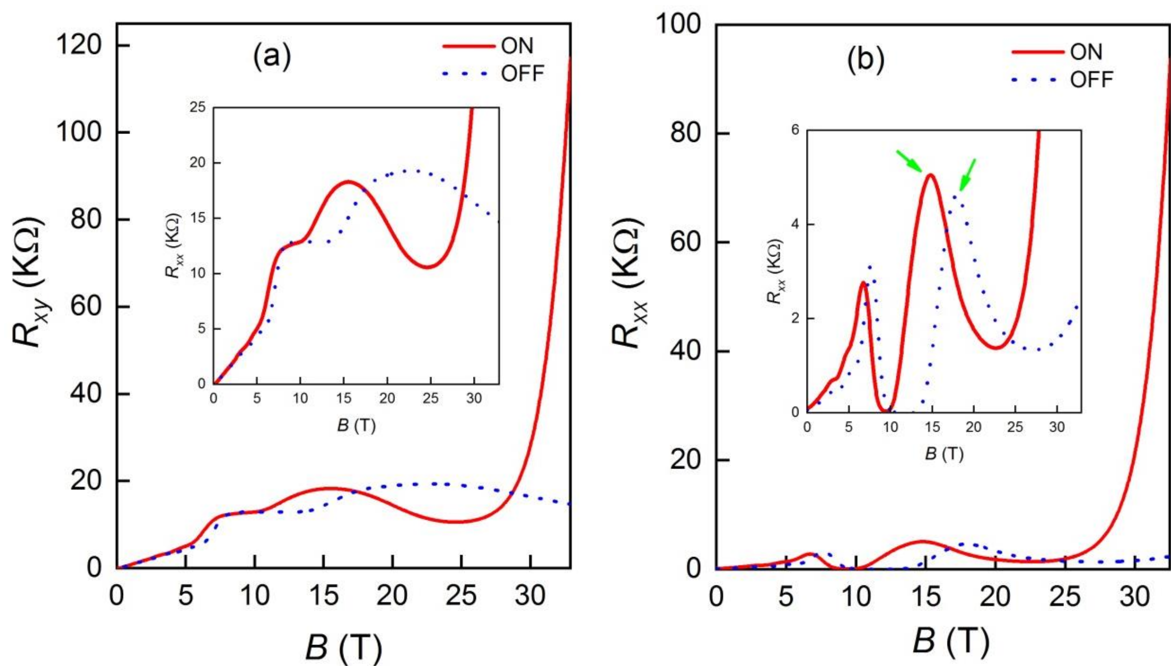

Figure 4. 22 Show the 20 nm QW thickness, under dark (blue dotted curve) and light (red full curve) conditions for (a) R_{xy} and (b) R_{xx} resistances at T = 2.2 K.

From the classic Hall effect, as discussed in section 2.3.1, it is possible to obtain the carrier concentration. Figure 4.23 (c) shows the calculated values for the illuminated (red open circles) and non-illuminated (blue open square) 20 nm well width sample. We notice a slight carriers concentration reduction when illuminated, it is unexpected once the light should enhance the carriers in the VB. However, it can be explained if the red light used to illumination is promoting carriers from the PbEuTe barrier to the extra layer, originated from the PbEuTe diffusion through the PbTe layer. This agrees with our previous assumption and also explain the fast increase in the resistance, exhibited in Figure 4.22 (a) and (b) for B>25 T, once that the conduction through the extra channel is enhanced. Although there is a carrier concentration reduction, the filling factors do not change, as shown in Figure 4.23 (b), where the *ff* can be directly obtained from the R_{xy} (e^2/h) as a function of 1/B plot. Also, the anomalous behavior seems to have increased for B>10 T, appearing a peak in Figure 4.23 (b) at B~25 T, when illuminated. These effects can be due to the conduction enhancement in the extra conduction channel.

From Figure 4.22 (b) (R_{xx}) maximum and minimum, shown in Figure 4.23 (a), we obtained the main frequency of 13 T (±1 T). This is the same value as that obtained from the sample under dark conditions (Figure 4.19 (d)). From the FFT analysis, shown in Figure 4.23 (d), we also obtained a 14 T (±1 T) main frequency which is in agreement with the discussion above. Also, two other frequencies, 24 T (±2 T) and 32 T (±3 T) appear, being different when compared with the 26 and 40 T found for the no-illuminated 20 nm well width sample. It is possible that the different B range used to perform the FFT analysis, for the illuminated (4 – 24 T) and no-illuminated (3 – 33 T) samples, is the cause of this difference.

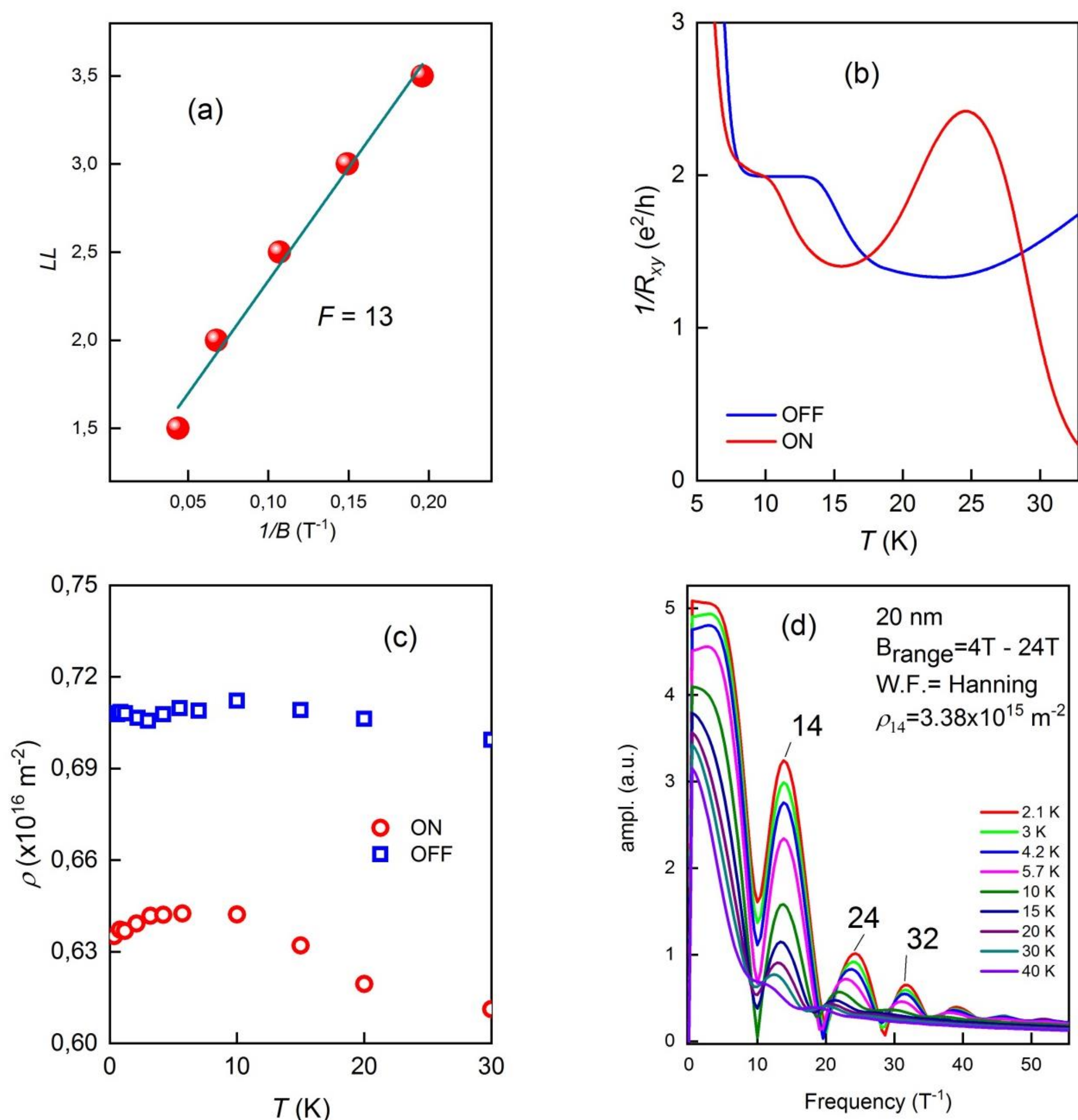

Figure 4. 23 Show the 20 nm QW thickness results for (a) maximums and minimums from illuminate SdHo R_{xx} (Figure 4.22 (b)) as a function of B and the linear fit that give a frequency value of 13 T. (b) Present the $1/R_{xy}$ in units of e^2/h, for illuminated (ON – red curve) and non-illuminated (OFF - blue curve) condition, where the filling factors are directed obtained. (c) Carriers concentrations as a function of temperature, for illuminated (ON – red circles) and non-illuminated (OFF - blue squares) condition. (d) FFT analysis of the SdHO at the illuminated condition for different temperatures.

Lastly, the 8 and 30 nm QW thickness measurements are shown in Figure 4.23. Clearly, no SdH oscillations are present in the R_{xx} resistance as a function of B, as shown in Figure 4.23 (a) and (b). Also, we can notice that these samples present high initial resistance values, compared with the others 10, 15 and 20 nm QW thicknesses. It may be possible that the indium contacts do not reach

the well, only diffusing through the barrier. This assumption is in agreement with the 8 nm R_{xx}(T) plotted in the inset of Figure 4.23 (a) which exhibited insulator worth mention that for all samples measured, several attempts to make contact were made. Most of those presented insulator profiles; however, the ones that show SdHO have a metallic behavior profile. This may also be associated with PbEuTe diffusion through the PbTe well. In this diffused PbEuTe layer, the Eu content is not enough to guarantee an insulator behavior. This allows parallel conduction between the PbTe well and this diffused PbEuTe layer similar to occur for the *n*-type PbEuTe QW discussed in section 4.1.

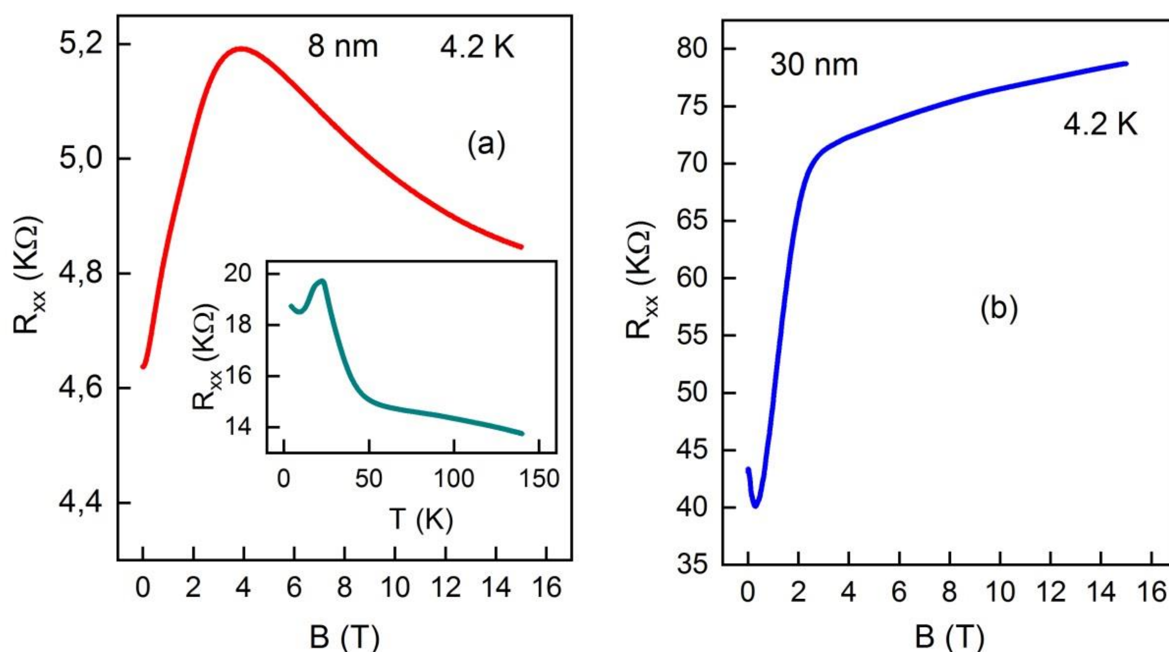

Figure 4. 24(a) and (b) Show longitudinal R_{xx} resistance for the 8 and 30 nm QW thickness, respectively, at T =4.2 K. The inset present the 8 nm well width sample R_{xx} as a function of temperature.

In short, magnetotransport measurements performed in *n* and *p*-type PbTe/PbEuTe QWs were presented in this chapter. The *n*-type samples presented positive photoconduction and fast photoresponse and also showed ~~a~~ parallel transport contribution between the PbTe well and the PbEuTe:Bi barriers that depend on the temperature region. Furthermore, magnetotransport properties of *p*-type 10, 15 and 20 nm well width samples were investigated, exhibiting SdHO and QHE at low temperature and high magnetic fields. We found that only the first longitudinal sub-

band, calculated using the envelope function model developed for lead-salt QWs, participate in the conduction mechanism. This was in agreement with the FFT oscillations analysis and with the calculated frequencies from the maximum and minimum oscillations. The filling factors sequence was justified by the Landau level spin splitting simulation, taking into account the calculated Fermi Level and the first longitudinal sub-band. Also, the 8 and 30nm QW thickness showed high resistance value and no SdHO or QHE. This can be associated with the PbEuTe barriers diffusion through the PbTe well, forming a PbEuTe layer with Eu content lower than the barrier.

5. Conclusions

From the results presented for *n*-type QWs, we found that the photoresponse to infrared light has contributions from different channels, barriers, and well. We verified that the contribution of each channel depends on the temperature region. For high temperatures, the transport via barriers is more effective since the thermal energy is comparable to the bismuth donor level located below the $Pb_{0.88}Eu_{0.12}Te$ conduction band edge. On the other hand, at low temperatures, the transport mechanism is dominated by the conduction through the PbTe well. The photoconductivity amplitude temperature dependence corroborates qualitatively well with the electron concentration and mobility, measured by Hall effect, under darkness and illumination conditions. We also found the persistent photoconductivity effect presence across the measured temperatures range and we were able to calculate the trap energy depth in the barriers from the experimental data and compare with the random potential model. The values are similar, although they differ due to the Bi atoms inclusion in the barriers, which was not considered in the model. Besides, we have shown that the photoconductivity amplitude decreasing at temperatures below $\approx$75 K is due to the electron-electron scattering, enhanced by conduction via multiple valleys, which leads to a reduction in carrier mobility.

For the *p*-type QWs, we compare three different well widths and found that 20 nm and 30 nm thick samples exhibit metallic or insulator behavior for different temperature ranges. However, the 10nm thick sample presented metallic behavior in all temperatures measured, showing clearly QHE and SdH oscillations, starting at 4 T. The QHE exhibit odd non-integers filling factor sequence (2.3; 3.4; 5.6; 6.9 and 8.8). However, for the analysis, we consider the approximated integers: 2; 4; 6; 7 and 9 calculated by the experimental B values corresponding to the observable R_{xy} plateaus. This odd sequence cannot be originated from the multi-valley transport mechanism, since only the first longitudinal valley participates, according to the Fermi level compared to the quantum confinement energy levels. However, this odd sequence may be associated with the Landau spin splitting fan chart diagram, presented in figure 4.14. In addition, the spin effect was observed as two main different peak frequencies, extracted from the FFT analysis, as 32 T and 45 T values that added become close to the principal frequency of 82 T, obtained from the Landau fan chart

diagram. These frequencies should be the second harmonic spin splitting of the main 18 T peak obtained from the FFT from at *B* up to 9 T. The high *g* factor, extracted from the oscillatory R_{xx} component is in agreement with the presented data, confirming that the odd filling factor sequence is due to the Landau level spin splitting. However, the fractional *ff* values may be related to the edge states, once that parallel conduction in the interface, between the barrier and well, was not enhanced or destroyed by illumination. However, further investigations are necessary to clarify this effect.

Furthermore, the 15 nm well width samples presented QHE with even integers filling factor values of 1, 2 and 3, unlike the 10 nm one. This sequence is also justified by the first longitudinal Landau level spin splitting fan chart diagram and the calculated Fermi level. The SdHO FFT analysis provided main frequencies peaks of 23, 41 and 50 T. The lower amplitude frequencies may be the main peak and the others are the second harmonic spin splitting. Also, the SdHO exhibit anomalous behavior at high *B* values that may be associated with the edge states. However, the carrier concentrations calculated from Hall measurements and the ones calculated from the main frequencies peak do not match, presenting a large difference. It is possible that the PbEuTe from the barrier is diffused through the PbTe well, which originated a PbEuTe layer with lower Eu content. This diffused layer can allow the transport via two channel, PbTe well and the PbEuTe diffused layer, similar to what occurred to the *n*-type PbTe/PbEuTe:Bi QW. This multi-channel conduction assumption can be responsible for the carrier concentration difference and also explain the observed anomalies in SdHO. Also, unlike the 10 nm well width sample, the 15 nm well width sample second harmonic spin splitting peaks, presented low amplitudes compared to the main peak.

The 20 nm well width samples also presented QHE with even integers filling factor values of 1 and 2, like the 15 nm one. This sequence is also justified by the first longitudinal Landau level spin splitting fan chart diagram and the calculated Fermi level. The SdHO FFT analysis provided main frequencies peaks of 14, 26 and 40 T. The lower amplitude frequency is the main peak and the others are the second and third harmonic, respectively. As found for the 15 nm QW thickness, the carrier concentrations calculated from Hall measurements, and the ones calculated from the main frequencies peak do not match. This result agrees with PbEuTe diffusion through the PbTe previous assumption. Also, the 20 nm QW thickness under illumination measurements corroborated with the discussion above. It shows a longitudinal resistance increase for higher *B* values and a decrease

in the carrier concentration. This can be due to the PeEuTe diffused layer carrier population, once the red light which is used to illuminate, has energy higher than the VB QW, making possible to have the carriers concentration enhancement in the diffused PbEuTe layer.

Finally, the 8 and 30nm QW thickness present high resistance and do not show SdHO, neither QHE. This also agrees with the assumption that an extra PbEuTe layer is formed from the PbEuTe barrier diffusion through the PbTe well.

We propose, for future research to calculate the possibles traps levels in the band gap, by performing photoconductivity measurements over the *p*-type QW samples investigated in this work, in order to further investigate these fractional filling factor sequence and the anomalous resistance profile behavior. Also, a new *p*-type sample series, varying the PbEuTe barrier thickness, can be grown to investigate the PbEuTe diffusion layer, by x-ray analysis.

6. Bibliography

[1] Y. L. Pei, Y. Liu, "Electrical and thermal transport properties of Pb-based chalcogenides: PbTe, PbSe, and PbS," *Journal of Alloys and Compounds,* vol. 514, p. 40– 44, 2012.

[2] G. Springholz, T. Schwarz, M. Aigle, H. Pascher and W. Heiss, "4.8 µm vertical emitting PbTe quantum-well lasers based on high-finesse EuTe/PbEuTe microcavities," *Applied Physics Letter,* vol. 76, p. 1807, 2000.

[3] A. Majumda, H. Z. Xu, S. Khosravani, F. Zhao, L. Jayasinghe, and Z. Shi, "High power light emission of IV–VI lead salt multiple-quantum-well structure grown by molecular-beam epitaxy on [111] BaF2 substrate," *Applied Physics Letter,* vol. 82, p. 493, 2003.

[4] S. Mukherjee, Z. Shi, "State of the art IV VI Semiconductor Light Emitting Devices in Mid - Infrared Opto Electronic Applications," *IETE Technical Review,* vol. 26, p. 236, 2009.

[5] B. Grbi, R. Leturcq, T. Ihn, K. Ensslin, D. Reuter, and Andreas D. Wieck, "Strong spin–orbit interactions and weak antilocalization in carbon doped p-type GaAs heterostructures," *Phys. Rev. B,* vol. 77, pp. 1-8, 2008.

[6] S. A. Studenikin, P. T. Coleridge, G. Yu, P. Poole, "Electron spin-orbit splitting in InGaAs/InP quantum well studied by means of the weak antilocalization and spin-zero effects in tilted magnetic fields.," *J.Semicond. Sci. Technol.,* vol. 20, p. 1103– 1110, 2005.

[7] I. Zutic, J. Fabian, S. Das Sarma,, "Spintronics: Fundamentals and applications," *Rev. Mod. Phys.,* vol. 76, pp. 323-410, 2004.

[8] S. Yuan, G. Springholz, and G. Bauer, "Electronic and optical properties of PbTe/Pb 1 EuTe multiple-quantum-well structures," *Phys. Rev. B,* vol. 49, p. 5476, 1994.

[9] J. Oswald, B. Tranta, M. Pippan, G. Bauer , "PbTe doping superlattices: properties of p-n-p and p-i-n-i-p structures," *J. optical Quantum Electronics,* vol. 22, p. S243, 1990.

[10] M. L. Peres, H. S. Monteiro, V. A. Chitta, S. de Castro, U. A. Mengui, P. H. O. Rappl, N. F. Oliveira, Jr.,E. Abramof, and D. K. Maude, "Experimental investigation of spin-orbit coupling in n-type PbTe quantum wells," *Journal of Applied Physics,* vol. 115, p. 093704, 2014.

[11] V. A. Chitta,W. Desrat, D. K. Maude, B. A. Piot,N. F. Oliveira, Jr.,P. H. O. Rappl,A. Y. Ueta and E. Abramof, "Multivalley transport and the integer quantum Hall effect in a PbTe quantum well," *Physical review B,* vol. 72, p. 195326, 2005.

[12] J. O. Dimmoock and G. B. Wright, "Band Edge Structure of PbS, PbSe, and PbTe," *Phys. Rev.,* vol. 135, 1964.

[13] M. Hulin , "Electron band structure of Tellurium," *J. Pkys. Chem. Solids ,* vol. 27, pp. 441-449, 1966.

[14] Y. Gelbstein, G. Gotesman, Y. Lishzinker, Z. Dashevsky and M.P. Dariel, "Mechanical properties of PbTe-based thermoelectric semiconductors," *Scripta Materialia,* vol. 58, p. 251–254, 2008.

[15] Z. H. Dughaish, "Lead telluride as a thermoelectric material for thermoelectric power generation," *Physica B,* vol. 322, p. 205–223, 2002.

[16] A. D. LaLonde, Y. Pei, H. Wang, and G. J. Snyder, "Lead telluride alloy thermoelectrics," *Materials today,* vol. 14, p. 526, 2011.

[17] Y. Kanai, R. Nii, and N. Watanabe , "Electrical Properties of Lead Telluride," *J. Appl. Phys.,* vol. 32, p. 2146, 1961.

[18] S. D. Mahanti, K. Hoang, S. Ahmad, "Deep defect states in narrow band-gap semiconductors," *Physica B,* Vols. 401-402, p. 291–295, 2007.

[19] R. Dalven, "A review of the semiconductor properties of PbTe, PbSe, PbS and PbO," *Infrared physics,* vol. 9, pp. 141-184, 1969.

[20] I. I. ZasavitskiĬ, E. V. Bushuev, E. A. Andrada e Silva, and E. Abramof, "Energy Spectrum of Quantum Wells in PbTe/PbEuTe-Based Structures from Photoluminescence Data," *JETP Letters,* vol. 75, pp. 559-562, 2002.

[21] L. W. Molenkamp, R. Eppenga, and G. W. 't Hooft, "Determination of valence-band efective-mass anisotropy in GaAs quantum wells by optical spectroscopy," *Phys. Rev. B ,* vol. 38, p. 4314, 1988.

[22] G. Springholz, "Chapter 13 - Molecular beam epitaxy of IV–VI semiconductors: multilayers, quantum dots and device applications," in *Molecular beam epitaxy of IV–VI semiconductors*, Elsevier, 2013, pp. 263-310.

[23] G. Springholz, G. Ihninger, G. Bauer, M. M. Olver, J. Z. Pastalan, S. Romaine, and B. B. Goldberg, "Modulation doping and observation of the integral quantum Hall effect in PbTe/Pb1-xEuxTe multiquantum wells," *Appl. Phys. Lett. ,* vol. 63, p. 2908, 1993.

[24] H. Schaber and R.E. Doezema, "Frar infrared spin-flip resonance in PbTe," *Solid State Communications,* vol. 31, pp. 197-199, 1979.

[25] J. Singleton, E. Kress-Rogers. A. V. Lewis, R. J. Nicholas, E. J. Fantner, G. Bauer and A. Oteros, "Magneto-optical studies of strained PbTe," *J. Phys. C: Solid State Phys.,* vol. 19, pp. 77-92, 1986.

[26] A. Prinz, G. Brunthaler, Y. Ueta, G. Springholz, and G. Bauer, "Electron localization in n-Pb12xEuxTe," *Phys. Rev. B,* vol. 59, p. 12 983, 1999.

[27] U. A. Mengui, E. Abramof, P. H. O. Rappl, B. Díaz, H. Closs, J. R. Senna, and A. Y. Ueta, "Electrical properties of PbTe doped with BaF2," *Journal Of Applied Physics ,* vol. 105, p. 043709, 2009.

[28] S. Castro, "Medidas de transporte elétrico em semicondutores de gap estreito," *Tese submetida ao Programa de Pós-Graduação em Engenharia de Materiais,* 2015.

[29] J. M. Schneider, M. L. Peres, S. Wiedmann, U. Zeitler, V. A. Chitta, E. Abramof, P. H. O. Rappl, S. de Castro, D. A. W. Soares, U. A. Mengui, and N. F. Oliveira Jr., "Systematic study of doping dependence on linear magnetoresistance in p-PbTe," *Appl. Phys. Lett.,* vol. 105, p. 162108, 2014.

[30] A. Dyrdal, V. K. Dugaev,J.Barnas, "Spin Hall effect in IV-VI semiconductors," *EPL,* vol. 85, p. 67004, 2009.

[31] S. Murakami, N. Nagaosa, S. C. Zhang, "Spin Hall Insulator," *Phys. Rev. Lett.,* vol. 93, p. 156804, 2004.

[32] S. A. Wolf, D. D. Awschalom, R. A. Buhrman, J. M. Daughton, S. von Molnár, M. L. Roukes, A. Y. Chtchelkanova, D. M. Treger, "Spintronics: A Spin-Based Electronics Vision for the Future," *Science,* vol. 294, p. 1488, 2001.

[33] S. Jin, C. Cai, G. Bi, B. Zhang, H. Wu, and Y. Zhang, "Two-dimensional electron gas at the metastable twisted interfaces of CdTe/PbTe (111) single heterojunctions," *Phys. Rev. B,* vol. 87, p. 235315, 2013.

[34] B. Zhang, C. Cai, S. Jin, Z. Ye, H. Wu, and Z. Qi, "Resonant nature of intrinsic defect energy levels in PbTe revealed by infrared photoreflectance spectroscopy," *Appl. Phys. Lett.,* vol. 105, p. 022109, 2014.

[35] M. L. Peres, V. A. Chitta, Nei F. Oliveira Jr., D. K. Maude, P. H. O. Rappl, A. Y. Ueta, E. , "Antilocalization of hole carriers in Pb1−xEuxTe alloys in the metallic regime," *Phys. Rev. B,* vol. 79, p. 085309, 2009.

[36] M. J. P. Pirralho, M. L. Peres, D. A. W. Soares, P. C. O. Braga, F. S. Pena, C. I. Fornari, P. H. O. Rappl, and E. Abramof, "Transition from negative to positive photoconductivity in p-type Pb1−xEuxTe films," *Phys. Rev. B,* vol. 95, p. 075202 , 2017.

[37] J. A. H. Coaquira, V. A. Chitta, N. F. Oliveira Jr, .P. H. O. Rappl, A. Y. Ueta, E. Abramof, G. Bauer, "Electrical Characterization of p-Type Pb1−xEu x Te," *Journal of Superconductivity,* vol. 16, p. 115, 2003.

[38] M. J. P. Pirralho, "Propriedades de fotocondutividade e transporte elétrico em filmes de Pb1-xEuxTe e Bi2Te3," in *Tede de Doutorado, UNIFEI, Itajubá-M.G.*, 2017.

[39] A. lshida, S. Matsuura, and H. Fujiyasu, "Properties of PbTe/EuTe short period superlatices and their application to LASER diodes," *Superlattices and Microstructures,* vol. 2, pp. 575-, 1986.

[40] D. L. Partin, "Lead Salt Quantum Effect Structures," *IEEE J. of Quantum Electronics ,* vol. 24, p. 1716, 1988.

[41] D. L. Partin, "Single quantum well lead-europium-selenide-telluride diode lasers," *Appl. Phys. Lett.,* vol. 45, p. 487, 1984.

[42] D. L. Partin, R. F. Majkowski, and D. E. Swets , "Quantum well diode lasers of lead-europium-selenlcle-telluride," *J. Vac. Sci. Technol. B,* vol. 3, p. 576, 1985.

[43] Z. Shi, M. Tacke, A. Lambrecht, and H. Bottner, "Midinfrared lead salt multi-quantum-well diode lasers with 282 K operation," *Appl. Phys. Lett.,* vol. 66, p. 2537, 1995.

[44] F. D. Rosi, "Thermoeletricity and thermoeletric power generation," *Solid-State Electronics ,* vol. 11, pp. 833-868, 1968.

[45] T. C. Harman, D. L. Spears, M. J. Manfra, "High thermoelectric figures of merit in PbTe quantum wells," *Journal of Electronic Materials,* vol. 25, p. 1121–1127, 1996.

[46] G. J. Snyder, and A. H. Snyder, "Figure of merit ZT of a thermoelectric device defined from materials properties," *Energy Environ. Sci.,* vol. 10, p. 2280, 2017.

[47] L. Yang, Z.-G. Chen, M. S. Dargusch, and J. Zou, "High Performance Thermoelectric Materials: Progress and Their Applications," *Adv. Energy Mater. ,* vol. 8, p. 1701797, 2018.

[48] D. A. Broido, T. L. Reinecke, "Theory of thermoelectric power factor in quantum well and quantum wire superlattices," *Phys. Rev. B,* vol. 64, p. 045324, 2001.

[49] S. Hikami, A. I. Larkin, and Y.Nagaoka , "Spin-Orbit Interaction and Magnetoresistance in the Two Dimensional Random System," *Prog. Theor. Phys. ,* vol. 63, p. 707, 1980.

[50] S. Jin, H. Wu, and T. Xu, "Large Rashba splitting in highly asymmetric CdTe/PbTe/PbSrTe quantum well structures," *Appl. Phys. Lett. B,* vol. 95, p. 132105, 2009.

[51] Pai-Chun Wei, Surojit Chattopadhyay, Min-De Yang, Shih-Chang Tong, Ji-Lin Shen, Chien-Yao Lu, Han-Chang Shih, Li-Chyong Chen, and Kuei-Hsien Chen, "Room-temperature negative photoconductivity in degenerate InN thin films with a supergap excitation," *Physical Review B,* vol. 81, pp. 045306-1, 2010.

[52] Yiming Yang, Xingyue Peng, Hong-Seok Kim, Taeho Kim, Sanghun Jeon,Hang Kyu KangWonjun Choi, Jindong Song, Yong-Joo Doh, and Dong Yu, "Hot Carrier Trapping Induced Negative Photoconductance in InAs Nanowires toward Novel Nonvolatile Memory," *Nano Lett.,* vol. 15, p. 5875, 2015.

[53] R. Jaramillo, Meng-Ju Sher, Benjamin K. Ofori-Okai, V. Steinmann, Chuanxi Yang, Katy Hartman,Keith A. Nelson, Aaron M. Lindenberg, Roy G. Gordon, "Transient terahertz photoconductivity measurements of minority-carrier lifetime in tin sulfide thin films: Advanced metrology V," *J. Appl. Phys.,* vol. 119, p. 035101, 2016.

[54] M. M. Furchi, D. K. Polyushkin, A. Pospischil, T. Mueller, "Mechanisms of photoconductivity in atomically thin MoS2," *Nano Lett.,* vol. 14, pp. 6165-6170, 2014.

[55] M. A. B. Tavares, M. J. da Silva, M. L. Peres, S. de Castro, D. A. W. Soares, A. K. Okazaki, C. I. Fornari, P. H. O. Rappl, and E. Abramof, "Investigation of negative photoconductivity in p-type Pb1-xSnxTe film," *Appl. Phys. Lett.,* vol. 110, p. 042102, 2017.

[56] R. L. Field III, Y. J i n, H. Cheng, T. Dannecker, R. M. Jock, Y. Q. Wang, C. Kurdak, and R. S. Goldman, "Influence of N incorporation on persistent photoconductivity in GaAsN alloys," *Phys. Rev. B,* vol. 87, p. 155303, 2013.

[57] J. Z. Li, J. Y. Lin, and H. X. Jiang, "Persistent photoconductivity in a twodimensional electron gas system formed by an GaAs/GaN heterostructures," *Journal of Applied Physics ,* vol. 82, p. 1227, 1997.

[58] S. de Castro, D. A. W. Soares, M. L. Peres, P. H. O. Rappl, and E. Abramof, "Room temperature persistent photoconductivity in p-PbTe and p-PbTeBaF2," *Appl. Phys. Lett.,* vol. 105, p. 022109, 2014.

[59] H. J. Queisser and D. E. Theodorou, "Decay kinetics of persistent photoconductivity in semiconductors," *Phys. Rev. B,* vol. 33, p. 4027, 1986.

[60] B. A. Akimov, V. A. Bogoyavlenskii, L. I. Ryabova, V. N. Vasil’kov, "Specific features of photoconductivity in thin n-PbTe:Ga epilayers," *Semiconductors,* vol. 35, p. 502–505, 2001.

[61] A. Ya. Shik, "Photoconductivity of randomly-inhomogeneous semiconductors," *A. F. Ioffe Physico-technical Institute (Zh. Eksp. Teor. Fi),* vol. 68, pp. 1859-186, 1975.

[62] A. Y. Shik , "Photoconductivity of randomly-inhomogeneous semiconductors," *Sov. Phys. JETP,* vol. 68, pp. 1859-1867, 1974.

[63] V. F. Mitin, "Heavily doped and fully compensated Ge single-crystalline films on GaAs," *Appli. Phys. Lett.,* vol. 92, p. 202111, 2008.

[64] K. von Klitzing, "The quantized Hall effect," *Reviews of Modern Physics,* vol. 58, p. 519, 1986.

[65] D. Tong, "University of Cambridge," January 2016. [Online]. Available: http://www.damtp.cam.ac.uk/user/tong/qhe/qhe.pdf. [Accessed 03 january 2019].

[66] J. H. Davies, The Physics of Low-Dimensional Semiconductors an Introduction, New York: Cambridge University Press, 1998.

[67] R. Gans, "Elektronentheorie der Metalle," *Physik,* vol. 20, p. 293, 1906.

[68] A. K. Okazaki, S. Wiedmann, S. Pezzini, M. L. Peres, P. H. O. Rappl, and E. Abramof, "Shubnikov–de Haas oscillations in topological crystalline insulator SnTe(111) epitaxial films," *Phys. Rev. B,* vol. 98, p. 195136, 2018.

[69] I. M. Lifshitz and L. M. Kosevich, "On the theory of the Shubnikov de Hass effect," *Soviet Physics JETP,* vol. 6, p. 67, 1958.

[70] Z. Ren, A. A. Taskin, S. Sasaki, K. Segawa, and Y.i Ando, "Large bulk resistivity and surface quantum oscillations in the topological insulator," *Physical Review B,* vol. 82, p. 241306, 2010.

[71] A.A. Taskin, S. Sasaki, K. Segawa, and Y. Ando, "Manifestation of Topological Protection in Transport Properties of Epitaxial Bi2Se3 films," *Physical Review Letters,* vol. 109, p. 066803, 2012.

[72] B. Hamdou, J. Gooth, A. Dorn, E. Pippel and K. Nielsch , "Surface state dominated transport in topological insulator Bi2Te3 nanowires," *Applied Physics Letters ,* vol. 103, p. 193107, 2013.

[73] J. Xiong, Y. Luo, Y. Khoo, S. Jia, R. J. Cava, and N. P. Ong, "High-field Shubnikov–de Haas oscillations in the topological insulator Bi2Te2Se," *Physics Review B,* vol. 86, p. 045314, 2012.

[74] D. Shoenberg, Magnetic Oscillations in Metals, New York: Cambridge University Press, 1984.

[75] J. R. Burke, B. Houston, and H. T. Savage, "Anisotropy of the Fermi Surface of p-Type PbTe," *PHYSICAL RE VIEW B,* vol. 2, 1970.

[76] J. Heremans , "Solid state magnetic field sensors and applications," *J. Phys. D: Appr. Phys.,* vol. 26, pp. 1149-1168, 1993.

[77] X. Liu, Z. L.Song, R.Wang, and Z.Y.Quan, "High Field Linear Magnetoresistance Sensors with Perpendicular Anisotropy L10-FePt Reference Layer," *Advances in Condensed Matter Physics,* vol. Article ID 8528617, 2016.

[78] P. Kapitza, "The Change of Electrical Conductivity in Strong Magnetic Fields.," *Roy. Soc. Proc.,* vol. 119, pp. 358-, 1929.

[79] I. M. Lifshitz, and V. G. Perschanskii , "Galvanomagnetic Characteristics of Metals with opem Fermi Surfaces," *J. Exptl. Theoret. Phys,* vol. 38, pp. 188-193, 1959.

[80] A. A. Abrikosov, "Galvanomagnetic phenomena in metals in the quantum limit," *Soviet Physics JETP,* vol. 29, p. 746, 1969.

[81] R. Xu, A. Husmann, T. F. Rosenbaum, M.-L. Saboungi, J. E. Enderby & P. B. Littlewood, "Largemagnetoresistance in non-magnetic silver chalcogenides," *letters to nature,* vol. 390, p. 57, 1997.

[82] A. Husmann, J. B. Betts, G. S. Boebinger, A. Migliori, T. F. Rosenbaum & M. -L. Saboungi, "Megagauss sensors," *Nature,* vol. 417, p. 421, 2002.

[83] A. A. Abrikosov, "Quantum magnetoresistance," *Physical Review B,* vol. 58, p. 2788, 1998.

[84] A. A. Abrikosov, "Gapless State of Bismuth-Type Semimetals," *Journal of Low Temperature Physics,* vol. 8, p. 315, 1972.

[85] F. S. Pena, M. L. Peres, M. J. P. Pirralho, D. A. W. Soares, C. I. Fornari, P. H. O. Rappl, and E. Abramof, "Fast photoresponse and high parallel transport in n-type PbTe/PbEuTe quantum wells," *Appl. Phys. Lett.,* vol. 111, p. 192105, 2017.

[86] G. Bauer and G. Springholz, "Molecular beam epitaxy- aspects and applications," *Vacuum,* vol. 43, pp. 357-356, 1992.

[87] C. I. Fornari, "Propriedades de filmes finos do isolante topológico telureto de bismuto crescidos por epitaxia de feixe molecular," *Tede de Doutorado, INPE, São José dos Campos,* 2017.

[88] A. K. Okazaki, "Estudo de Filmes Finos de PbTe:CaF2, Crescidos por Epitaxia de Feixe Molecular," *Dissertação de Mestrado, INPE, São José dos Campos,* 2015.

[89] "Korth Kristalle GmbH," Korth Kristalle GmbH, [Online]. Available: https://www.korth.de/. [Accessed 04 03 2019].

[90] Ú. A. Mengui, "Crescimento por MBE e caracterização de filmes SnTe e heteroestruturasde SnTe/Sn1-xEuxTe sobre BaF2," *Tese de Doutorado, INPE, São Jose dos Campos,* 2006.

[91] Rappl, P. H. O., "Las: Laboratório Associado de Sensores e Materiais," INPE, [Online]. Available: http://www.las.inpe.br/~cesar/Infrared/mbe.htm. [Accessed 24 12 2018].

[92] "Molecular Materials Research Center," Beckman Institute: California Institute of Technology, [Online]. Available: http://mmrc.caltech.edu/Vacuum/. [Accessed 24 01 2019].

[93] G. Springholz, *Molecular Beam Epitaxy and in situ Reflection High-Energy Electron Diffraction of IV-VI Semiconductor Heterostructures. PhD dissertation, Institut für Halbleiterphysik, Johannes-Kepler-Universität Linz, A-4045 Linz-Auhof, Österreich,* September 1993, ISBN 3 85320 648 4.

[94] M. Dabrowska-Szata, "Analysis of RHEED pattern from semiconductor surfaces," *Materials Chemistry and Physics,* vol. 81, pp. 257-259, 2003.

[95] L. Reimer, I. Fromm, and I.Naundorf, "Electron spectroscopc difraction," *Ultramicroscopy ,* vol. 32, pp. 80 - 91 , 1990.

[96] K. Omoto, K. Tsuda, and M. Tanaka, "Simulations of Kikuchi patterns due to thermal diffuse scattering on MgO crystals," *Journal of Electron Microscopy,* vol. 51, pp. 67 - 78, 2002.

[97] J. A. Eades , "Laue Zones: A clarification of nomenclature," *Ultramicroscopy,* vol. 32, p. 183, 1990.

[98] C. I. Fornari, Paulo H. O. Rappl, Sérgio L. Morelhão, and Eduardo Abramof, "Structural properties of Bi2Te3 topological insulator thin films grown by molecular beam epitaxy on (111) BaF2 substrates," *Journal of Applied Physics,* vol. 119, p. 165303, 2016.

[99] M. A. Herman, H. Sitter, Molecular Beam Epitaxy, Fundamentals and Current Status, Vol. 7, Berlin: Springer Science & Business Media, 1990.

[100] M. Borgström, " Epitaxial Growth, Processing and Characterization of Semiconductor Nanostructures," *Division of Solid State Physics, Department of Physics, Lund University, Box 118, SE-221 00 Lund, Sweden,,* 2003.

[101] S. Yuan, H. Krenn, G. Springholz, Y. Ueta, and G. Bauer, "Magnetoreflectivity of Pb12xEuxTe epilayers and PbTe/Pb12xEuxTe multiple quantum wells," *Phys. Rev. B,* vol. 55, p. 4607, 1997.

[102] "Radboud University, High Field Magnet Laboratory (HFML)," [Online]. Available: https://www.ru.nl/hfml/research/levitation/diamagnetic-levitation/bitter-solenoid/. [Accessed 05 03 2019].

[103] " ANTONIO POLIMENI'S HOMEPAGE," [Online]. Available: https://antoniopolimeni-physics.weebly.com/research.html. [Accessed 05 03 2019].

[104] F. S. Pena, M. L. Peres, M. J. P. Pirralho, D. A. W. Soares, C. I. Fornari, P. H. O. Rappl, and E. Abramof;, "Fast photoresponse and high parallel transport in n-type PbTe/PbEuTe quantum wells," *Appl. Phys. Lett.,* vol. 111, p. 192105, 2017.

[105] M. M. Glazov and E. L. Ivchenko, "Electron-electron scattering effect on spin relaxation in multi-valley nanostructures," *EPL,* vol. 87, p. 57005, 2009.

[106] M. L. Peres, R. M. Rubinger, L. H. Ribeiro, C. P. L. Rubinger, G. M. Ribeiro, V. A. Chitta, P. H. O. Rappl, and E. Abramo4, "Conduction mechanisms in p-type Pb1−xEuxTe alloys in the insulator regime," *Journal of Applied Physics,* vol. 111, p. 123708, 2012.

[107] R. J. Haug and K. von Klitzing, "Influence of Edge Currents on Shubnikov-de Haas Oscillations in Two-Dimensional Systems," *Europhysics Letters,* vol. 10, pp. 489-192, 1989.

[108] M. König, S. Wiedmann, C.h Brüne, A. Roth, H. Buhmann, L. W. Molenkamp, X.-L. Qi, S.-C. Zhang, "Quantum spin Hall insultor state in HgTe quantum wells," *Science,* vol. 318, p. 766, 2007.

[109] B. Ostahie, M. Nita, and A. Aldea, "Edge states mechanism for the anomalous quantum Hall effect in diatomic square lattice," *Physical Review B,* vol. 98, p. 125403, 2018.

[110] S. Barua, K. P. Rajeev and A. K. Gupta, "Evidence for topological surface states in metallic single crystals of Bi2Te3," *J. Phys.: Condens. Matter,* vol. 27, p. 015601 , 2015.

[111] A. R. Wright and R. H. McKenzie, "Quantum oscillations and Berry’s phase in topological insulator surface states with broken particle-hole symmetry," *Physical Review B,* vol. 87, p. 085411, 2013.

[112] S. E. Kohn, P. Y. Yu, Y. Petroff, Y. R. Shen, Y. Tsang, and M. L. Cohen, "Electronic Band Structure and Optical Properties of PbTe, PbSe, and PbS," *PHYSICAL REVIEW B,* vol. 8, 1973.

[113] E. A. de Andrada e Silva, "Optical transition energies for lead-salt semiconductor quantum wells," *PHYSICAL REVIEW B,* vol. 60, p. 8859, 1999.

[114] E. Abramof, E. A. de Andrada e Silva, S. O. Ferreira, P. Motisuke, P. H. O. Rappl, and A. Y. Ueta, "Optical spectra of PbTe/Pb1-xEuxTe quantum wells," *Phys. Rev. B,* vol. 63, p. 085304, 2001.

[115] H. Schaber and R.E. Doezema, "Far infrared spin ressonance in PbTe," *Solid State Communications,* vol. 31, pp. 197-199, 1979.

[116] T. Ichiguchi, S. Nishikawa and K. Murase, "Lattice and electronic properties and g value of PbSnTe," *Solid State Communications,,* vol. 34, p. 309—314, 1980.

[117] H. Burkhard, G. Bauer, W. Zawadzki, "Band-population effects and intraband magneto-optical propertiesof a many-valley semiconductor: PbTe," *Phys. Rev. B,* vol. 19, p. 5149, 1979.

[118] M. M. Hasegawa and E. A. de Andrada e Silva, "Spin-orbit-split subbands in IV-VI asymmetric quantum wells," *Physical Review B,* vol. 68, p. 205309, 2003.

[119] I. G. Savel’ev, A. M. Kreshchuk, S. V. Novikov, A. Y. Shik, G. Remenyi,, "Spin splitting of the Landau levels and exchange interaction of a non-ideal two-dimensional electron gas in InxGa1−xAs/InP heterostructures," *J. Phys.: Condens. Matter,* vol. 8, p. 9025–9036, 1996.

[120] M. J. W., Epitaxial Growth, part A, New York: Academic Press, INC, 1975.

[121] M. Rahman, and N.l Hasan, "Compound Semiconductor Epitaxial Growth Techniques," *Int. J. Thin. Fil. Sci. Tec.,* vol. 5, pp. 45-49, 2016.

[122] W. Knap, V. I. Fal'ko, E. Frayssinet, P. Lorenzini, N. Grandjean, D.Maude, G. Karczewski, B. L. Brandt, J. Łusakowski, I. Grzegory, M. Leszczy´nski, P. Prystawko, C. Skierbiszewski, S.Porowski, X. Hu, G. Simin, M. Asif Khan and M. S. Shur, "Spin and interaction effects in Shubnikov–de Haas oscillations and the quantum Hall effect in GaN/AlGaN heterostructures," *J. Phys.: Condens. Matter,* vol. 16, p. 3421–3432, 2004.

[123] I. Strzalkowski, S. Joshi, and C. R. Crowell, "Dielectric constant and its temperature dependence for GaAs, CdTe, and ZnSe," *Appl. Phys. Lett.,* vol. 28, p. 350, 2008.

[124] W. Shockley, and W. T. Read Jr., "Statistics of the Recombinations of Holes and Electrons," *Physical Review,* vol. 87, p. 835, 1952.

[125] A.Y. Shik, Electronic Properties of Inhomogeneous Semiconductors, Luxembourg: Gordom and Breach Publishers, 1995.

[126] H. H. Timothy, H. Lin, J. Liu, W. Duan, A. Bansil, and L. Fu, "Topological crystalline insulators in the SnTe material class," *Nat. Commun.,* vol. 3, p. 982, 2012.

[127] S. Maekawa, and H. Fukuyama, "Magnetoresistance in Two-Dimensional Disordered Systems: Effects of Zeeman Splitting and Spin-Orbit Scattering," *J. Phys. Soc. Jpn.,* vol. 50, pp. 2516-2524, 1981.

[128] F. C. Frank , J. H. Van Der Merwe , and N. F. Mott, "One-dimensional dislocations. II. Misfitting monolayers and oriented overgrowth," *Proc. R. Soc. London Ser. A,* vol. 198, p. 205, 1949.

[129] G. Nimtz, "Recombination in narrow-gap semiconductors," *Physics Reports,* vol. 63, pp. 265-300, 1980.

[130] D. John, The Physics of Low Dimensional Semiconductors, Glasgow: Cambridge University Press, 1998.

[131] G. Bauer and H. Clemens , "Physics and applications of IV-VI compound quantum well and superlattice structures," *Semicond. Sci. Technol. ,* vol. 5, pp. S122-5130, 1990.

[132] E. A. d. A. e. Silva, "Optical transition energies for lead-salt semiconductor quantum wells," *PHYSICAL REVIEW B,* vol. 60, p. 8859, 1999.

[133] S.A.J. Wiegers, P.C.M. Christianen, H. Engelkamp, A. den Ouden, J.A.A.J. Perenboom, U. Zeitler, J.C. Maan, "The High Field Magnet Laboratory at Radboud University Nijmegen," *J. Low Temp. Phys. ,* vol. 159, p. 389–393, 2010.

[134] S. Keshav, M. Vera, L. Bernd, and P.l C. W. Chu, "Shubnikov–de Haas oscillations from topological surface states of metallic BiSeTe," *Phys. Rev. B,* vol. 90, p. 241111(R) , 2014.

[135] E. Hall, "On a New Action of the Magnet on Electric Currents," *American Journal of Mathematics,* vol. 2, p. 287–92, 1879.

[136] J. Nickel, "Magnetoresistance Overview," *Hewlett-Packard Company,* 1995.

[137] M. Li, Z. Wang, L. Yang, X. P.A. Gao, and Z. Zhang, "From linear magnetoresistance to parabolic magnetoresistance in Cu and Cr-doped topological insulator Bi2Se3 films," *Journal of Physics and Chemistry of Solids,* pp. 1-6, 2017.